

Measurement of the CKM Matrix
Element $|V_{ub}|$ with $B \rightarrow \rho e \nu$ Decays
at *BABAR*

D I S S E R T A T I O N

zur Erlangung des akademischen Grades

Doctor rerum naturalium
(Dr. rer. nat.)

vorgelegt

der Fakultät Mathematik und Naturwissenschaften
der Technischen Universität Dresden

von

Diplom Physiker Leif Hendrik Wilden,
geboren am 18. Februar 1974 in Hamburg

Abstract

The branching fraction for $B \rightarrow \rho e \nu$ and the CKM matrix element $|V_{ub}|$ is measured with semileptonic exclusive B meson decays using approximately 55 million $\Upsilon(4S) \rightarrow B\bar{B}$ decays collected during the years 2000 and 2001 with the *BABAR* detector. The result is

$$\begin{aligned}\mathcal{B}(B^0 \rightarrow \rho^- e^+ \nu) &= (3.39 \pm 0.44 \pm 0.52 \pm 0.60) \times 10^{-4}, \text{ and} \\ |V_{ub}| &= (3.69 \pm 0.23 \pm 0.27_{-0.59}^{+0.40}) \times 10^{-3}.\end{aligned}$$

The quoted errors are statistical, systematic, and theoretical respectively. These are combined results obtained using five different form-factor models. Individual results are also quoted.

Zusammenfassung

Das Verzweigungsverhältnis $B \rightarrow \rho e \nu$ und das CKM Matrix Element $|V_{ub}|$ werden mittels semileptonischer exklusiver B Mesonen Zerfälle gemessen. Die Daten wurden in den Jahren 2000 und 2001 mit dem *BABAR* Dektector aufgezeichnet und entsprechen ungefähr 55 Millionen $\Upsilon(4S) \rightarrow B\bar{B}$ Zerfällen. Das Ergebnis ist

$$\begin{aligned}\mathcal{B}(B^0 \rightarrow \rho^- e^+ \nu) &= (3.39 \pm 0.44 \pm 0.52 \pm 0.60) \times 10^{-4} \text{ und} \\ |V_{ub}| &= (3.69 \pm 0.23 \pm 0.27_{-0.59}^{+0.40}) \times 10^{-3}.\end{aligned}$$

Die angegebenen Fehler sind statistisch, systematisch und theoretisch. Dieses Ergebnis ist eine Kombination von Ergebnissen fünf verschiedener Form-Faktor Modelle. Die Ergebnisse werden auch für jedes Modell einzeln angegeben.

Contents

1	Introduction	4
1.1	Overview	4
1.2	Outline of the Thesis	4
2	Theoretical Aspects	5
2.1	The Standard Model	5
2.1.1	Symmetry Breaking and the Higgs Mechanism	7
2.1.2	Electroweak Interaction and the CKM Matrix	8
2.1.3	The Strong Interaction	9
2.2	Semileptonic B Meson Decays	10
2.2.1	Signal Decay Kinematics	11
2.2.2	Form-Factor Models	15
3	The <i>BABAR</i> Experiment	19
3.1	Introduction	19
3.2	The <i>BABAR</i> Detector	20
3.2.1	Silicon Vertex Tracker	20
3.2.2	Drift Chamber	22
3.2.3	Cherenkov Detector	22
3.2.4	Electromagnetic Calorimeter	23
3.2.5	Instrumented Flux Return	26
4	Analysis Strategy	27
4.1	Dataset	27
4.2	Monte Carlo Simulation	27
4.2.1	Corrections to the Monte Carlo Simulation	32
4.3	Event Selection	33
4.3.1	Multihadron Selection	34
4.3.2	Electron Selection	34

4.3.3	Hadron Selection	38
4.3.4	Missing Momentum	39
4.3.5	Consistency Cuts	42
4.3.6	Continuum Rejection	44
4.3.7	Cut Optimization	49
4.3.8	Selection Results	49
4.4	Fit Method	52
4.4.1	Fit Variables	53
4.4.2	Contributions to the Fit	53
4.4.3	The Extended Binned Maximum-Likelihood Fit	56
4.4.4	Checks of the Fit Method	60
4.5	Reweighting Technique	61
4.6	Reconstruction of q^2	61
5	Results	65
5.1	Branching-Fraction Fit Result	65
5.2	Fit Projections	68
5.3	Fit Quality	69
5.4	Systematic Errors	78
5.4.1	Detector Simulation	78
5.4.2	Background Modeling	80
5.4.3	Other Systematic Errors	82
5.5	Extraction of $ V_{ub} $	86
5.6	Comparison with Other Measurements	86
6	Conclusions and Outlook	89
	Acknowledgements	99

Chapter 1

Introduction

1.1 Overview

In this thesis the measurement of the CKM matrix element $|V_{ub}|$ with semileptonic exclusive B meson decays using *BABAR* Run I and Run II data, corresponding to approximately 55 million $B\bar{B}$ meson pair decays, is described. Five decay modes $B \rightarrow H_u e \nu$ are studied, where $H_u = \rho^0, \rho^\pm, \pi^0, \pi^\pm$, or ω . The analysis is optimized for $B \rightarrow \rho e \nu$ decays with electrons at high momenta above the $b \rightarrow c$ kinematic endpoint. The two pion channels are included into the analysis because of the crossfeeds into the signal channels. A two dimensional fit of ΔE (the reconstructed B meson energy minus the expected energy) versus the ρ (ω) mass spectrum M_{had} is performed in two different electron-energy regions. The measured rate is then extrapolated to the entire electron energy-spectrum according to selected form-factor models and the total branching fraction \mathcal{B} is extracted. Form-factor models relate \mathcal{B} to $|V_{ub}|^2$. Results for each form-factor model and a combined result for \mathcal{B} and $|V_{ub}|$ are quoted.

1.2 Outline of the Thesis

The outline of this thesis is as follows: Chapter 2 gives an overview of the Standard Model with emphasis on theoretical aspects associated to the measurement of exclusive $B \rightarrow \rho l \nu$ branching fractions and the determination of the CKM matrix element $|V_{ub}|$. In chapter 3 the e^+e^- collider PEP-II and the *BABAR* experiment are introduced. Chapter 4 explains the analysis strategy, the datasets used, and the Monte Carlo simulations used to model the data. The fit method which is used to extract the branching fraction is explained in detail at the end of this chapter. The results and a comparison to results from other experiments are presented in chapter 5. The last chapter closes with a conclusion and an outlook on future measurements.

Chapter 2

Theoretical Aspects

This chapter gives a short overview of the Standard Model with emphasis on the weak interaction. The reader is then introduced to semileptonic B meson decays, and in particular to various form-factor models which have been proposed to describe $B \rightarrow X_u \ell \nu$ decays.

2.1 The Standard Model

The Standard Model represents our current knowledge about fundamental particles and their interactions. It is a gauge field theory with the gauge group $SU(3) \times SU(2)_L \times U(1)$. All baryonic matter in the universe is composed out of fermions with spin 1/2 and interactions among these are mediated by gauge bosons with an integer spin. There are six *flavors* of quarks and six kinds of leptons arranged in three *generations*. All quarks and leptons together with their quantum numbers are listed in Table 2.1. For each particle there is a corresponding anti-particle. All fermions of the Standard Model have been observed experimentally. The mass in each generation of quarks and leptons increases. The reason for this mass pattern remains unknown. In Table 2.1 L and R denote left or right handed fields. The charge Q is not an independent quantum number. It is given by the relation $Q = T_3 + Y$, where T_3 is the Eigenvalue of the third component of the weak isospin T , and Y is the weak hypercharge. The left handed fields of quarks and leptons are doublets Q_i and L_i with respect to the weak interaction. All other fields are isospin singlets. Quantum Chromo Dynamics (QCD), the theory which describes the strong interactions, introduces another degree of freedom: the color charge C , which can either be *red*, *green*, or *blue* (see section 2.1.3).

Interactions are mediated by gauge bosons. The gauge boson fields generate the invariance of the Lagrangian under local gauge transformations:

$$\begin{array}{ll} \text{electromagnetic} & \gamma (q = 0) \\ \text{weak} & W^+ (q = 1), W^- (q = -1), Z (q = 0) \\ \text{strong} & g_1 \dots g_8 (q = 0) \end{array} \quad (2.1)$$

The gravitational interaction which is not listed here lacks such a consistent quantum field theory. However due to its weakness it can be neglected in the description of fundamental particle interactions for all practical purposes. The W bosons allow transitions

			interaction →		electromag.		strong
			gauge group →		U(1)		SU(3)
			T	T ₃	Y	Q	C
quantum number →							
quarks:							
$Q_1 = \begin{pmatrix} u \\ d' \end{pmatrix}_L$	$Q_2 = \begin{pmatrix} c \\ s' \end{pmatrix}_L$	$Q_3 = \begin{pmatrix} t \\ b' \end{pmatrix}_L$	1/2	+1/2 -1/2	+1/6	+2/3 -1/3	r,g,b
u_R	c_R	t_R	0	0	+2/3	+2/3	r,g,b
d_R	s_R	b_R	0	0	-1/3	-1/3	r,g,b
leptons:							
$L_1 = \begin{pmatrix} \nu_e \\ e \end{pmatrix}_L$	$L_2 = \begin{pmatrix} \nu_\mu \\ \mu \end{pmatrix}_L$	$L_3 = \begin{pmatrix} \nu_\tau \\ \tau \end{pmatrix}_L$	1/2	+1/2 -1/2	-1/2	0 -1	
e_R	μ_R	τ_R	0	0	-1	-1	

Table 2.1: Quantum numbers of quarks and leptons. L and R denote left- and right-handed fields, Y the weak hypercharge, Q the electric charge, C the color charge and T the weak isospin.

between quarks of different generations. These interactions are described by the CKM matrix (see sections 2.1.1 and 2.1.2). The three neutrinos (ν) have no mass according to the Standard Model and transitions among the three generations are not allowed. However such transitions have recently been observed by the Super Kamiokande [1] and the SNO (Sudbury Neutrino Observatory) [2] experiments. The Standard Model can be extended to accommodate for neutrino masses, though at this point the experimental data does not allow to distinguish between different possible extensions of the model. The physical fields W^\pm , Z and γ of the electroweak interaction are given by linear combinations of the fundamental representations of the $SU(2)_L \times U(1)$ symmetry:

$$\begin{aligned}
 W^\pm &= \frac{1}{\sqrt{2}}(W_1 \mp iW_2) , \\
 Z &= \cos \theta_W W_3 - \sin \theta_W B , \\
 \gamma &= \sin \theta_W W_3 + \cos \theta_W B ,
 \end{aligned}
 \tag{2.2}$$

where W_1 , W_2 , and W_3 are the generators of the $SU(2)$ group, and B is the generator of the $U(1)$ group. θ_W is the weak mixing angle or Weinberg angle [3].

A priori invariance of the Standard Model Lagrangian under $SU(2)_L$ transformations can only be achieved if there are no mass terms for quarks and leptons. Since this is obviously not true, the Standard Model requires a different mechanism for generating the fermion masses. This is accomplished by the presence of the *Higgs* field, acting as a background field coupling to the fermions and gauge bosons. The Higgs field and the CKM matrix are closely related. This will be described in more detail in section 2.1.1. The Higgs particle has not been observed experimentally. Its discovery is one of the major goals of the Large Hadron Collider (LHC) experiment, which is currently being built at CERN (Conseil Européen pour la Recherche Nucléaire). Also new linear e^+e^- colliders operating at energies of up to 1 TeV, for example the TESLA project (Tera Electron Volt Energy Superconducting Linear Accelerator), have been proposed to precisely measure the properties of the Higgs boson.

Another way of probing the Standard Model is to test the Standard Model predictions for CP asymmetries in certain weak processes. The letter C denotes charge conjugation and the letter P the parity operation. CP violation has first been observed experimentally in the K meson system. It is the primary goal of the *BABAR* experiment to discover and measure CP asymmetries also in the B meson system. Mainly due to the large b quark mass, theoretical predictions for the B meson system are in general more reliable than for the K meson system.

2.1.1 Symmetry Breaking and the Higgs Mechanism

The Standard Model generates fermion mass terms in the Lagrangian by introducing a single scalar Higgs doublet $\Phi = (\Phi_1, \Phi_2)$ [4]

$$\mathcal{L}_{Higgs} = (\partial^\alpha \Phi)^\dagger (\partial_\alpha \Phi) - V(\Phi), \quad \text{with } V(\Phi) = -\mu^2 \Phi^\dagger \Phi + \lambda^2 (\Phi^\dagger \Phi)^2. \quad (2.3)$$

The potential is constructed in such a way that it has the shape of a Mexican hat, giving a non zero vacuum expectation value v in its ground state. The Yukawa coupling of the quarks in the i^{th} generation can be written as (note $\tilde{\Phi} = i\sigma_2 \Phi^*$)

$$\mathcal{L}_Y = A_{ij}^u \bar{Q}_{Li}^I \tilde{\Phi} u_{Rj}^I + A_{ij}^d \bar{Q}_{Li}^I \Phi d_{Rj}^I + \text{h.c.} . \quad (2.4)$$

The superscript I denotes quark fields in the interaction eigenbasis, to be distinguished from the mass eigenbasis. The interaction of the quarks with the $SU(2)_L$ gauge bosons is given by

$$\mathcal{L}_W = -\frac{1}{2} g \bar{Q}_{Li}^I \gamma^\mu \tau^a Q_{Li}^I W_\mu^a, \quad (2.5)$$

where τ^a operates in $SU(2)_L$ space. g is the weak coupling constant. The charged current interaction in Eq. 2.5 is given by

$$\mathcal{L}_W = -\frac{1}{\sqrt{2}} g \bar{u}_{Li}^I \gamma^\mu d_{Li}^I W_\mu^+ + \text{h.c.} . \quad (2.6)$$

After spontaneous symmetry breaking the Higgs doublet is replaced by

$$\Phi \rightarrow \Phi(x) = \frac{1}{\sqrt{2}} \begin{pmatrix} 0 \\ v + h(x) \end{pmatrix}. \quad (2.7)$$

v is the vacuum expectation value of the Higgs field, and h its excitations. The mass terms that arise from Eq. 2.4 are

$$\mathcal{L}_M = \frac{v}{\sqrt{2}} [A_{ij}^u \bar{u}_{Li}^I u_{Rj}^I + A_{ij}^d \bar{d}_{Li}^I d_{Rj}^I + \text{h.c.}], \quad (2.8)$$

i.e. the mass matrices are

$$M^u = -A^u \frac{v}{\sqrt{2}} \quad \text{and} \quad M^d = -A^d \frac{v}{\sqrt{2}}. \quad (2.9)$$

One can now transform to the mass eigenbasis by choosing four complex unitary matrices such that $V_{dL} M_d V_{dR}^\dagger = M_d^{\text{diag}}$ and $V_{uL} M_u V_{uR}^\dagger = M_u^{\text{diag}}$, where M_q^{diag} are diagonal and real. The charged current interactions from Eq. 2.5 expressed in this mass eigenbasis are then given by

$$\mathcal{L}_W = -\frac{1}{\sqrt{2}} g \bar{u}_{Li} \gamma^\mu \bar{V}_{ij} d_{Lj} W_\mu^+ + \text{h.c.} . \quad (2.10)$$

The matrix $\bar{V} = V_{uL} V_{dL}^\dagger$ in this equation is called Cabibbo-Kobayashi-Maskawa matrix [5]. All terms corresponding to lepton couplings have been left out in the previous discussion.

2.1.2 Electroweak Interaction and the CKM Matrix

The coupling of the quarks to the W bosons is given by Eq. 2.10. It was shown in the previous section that the CKM matrix relates the interaction eigenstates to their mass eigenstates:

$$d_i^I = \begin{pmatrix} d' \\ s' \\ b' \end{pmatrix} = \begin{pmatrix} V_{ud} & V_{us} & V_{ub} \\ V_{cd} & V_{cs} & V_{cb} \\ V_{td} & V_{ts} & V_{tb} \end{pmatrix} \cdot \begin{pmatrix} d \\ s \\ b \end{pmatrix} \quad (2.11)$$

For example in a quark decay $q \rightarrow W^- Q$ the coupling is gV_{Qq} , for the decay $Q \rightarrow W^+ q$ the coupling is gV_{Qq}^* .

The CKM matrix is a unitary 3×3 matrix by construction, i.e. it has 9 free real parameters. After eliminating the unobservable phases from the quark fields, 3 real angles and one complex phase remain. Measurements show that the diagonal elements are close to 1, the off-diagonal elements are an order of magnitude smaller, and transitions between the first and third generation are even smaller. A representation of the CKM matrix which makes use of this fact and is often used when CP violation is discussed is the Wolfenstein approximation [6]:

$$V_{CKM} \approx \begin{pmatrix} 1 - \frac{\lambda^2}{2} & \lambda & A\lambda^3(\rho - i\eta) \\ -\lambda & 1 - \frac{\lambda^2}{2} & A\lambda^2 \\ A\lambda^3(1 - \rho - i\eta) & -A\lambda^2 & 1 \end{pmatrix} \quad (2.12)$$

Experimentally we measure that $\lambda \approx 0.22$ and $A \approx 0.82$. CP violation occurs if $\eta \neq 0$. Unitarity ($V_{CKM}V_{CKM}^\dagger = 1$) requires that $V_{ud}V_{ub}^* + V_{cd}V_{cb}^* + V_{td}V_{tb}^* = 0$. This equation, after dividing by $V_{cd}V_{cb}^*$, can be represented as a triangle in the complex plane, which is usually referred to as the *unitarity triangle*, see Fig. 2.1. The triangle's apex is given by the point (ρ, η) . The three angles are given by

$$\alpha = \arg \left[-\frac{V_{td}V_{tb}^*}{V_{ud}V_{ub}^*} \right], \quad \beta = \arg \left[-\frac{V_{cd}V_{cb}^*}{V_{td}V_{tb}^*} \right], \quad \gamma = \arg \left[-\frac{V_{ud}V_{ub}^*}{V_{cd}V_{cb}^*} \right] = \pi - \alpha - \beta \quad (2.13)$$

The angles are a measure of CP violation in the B meson system. The length of the triangle's left side is proportional to the matrix element V_{ub} . The measurement of $|V_{ub}|$ in processes that do not violate the CP symmetry can be compared to measurements of $\sin(2\beta)$. The Standard Model is consistent only if both independent measurements give a consistent result, meaning that the triangle closes at its apex.

All matrix elements can be measured by non CP violating processes. $|V_{ud}|$ has been determined from nuclear beta decays, semileptonic kaon and hyperon decays give $|V_{us}|$, neutrino and antineutrino production of charm or valence d quarks give $|V_{cd}|$, semileptonic D meson decays measure $|V_{cs}|$ and semileptonic B meson decays $|V_{cb}|$. $|V_{ub}|$ can be measured by inclusive semileptonic B meson decays or as done in this thesis by exclusive reconstruction. Using the unitarity constraints, one can summarize the results from different experiments as follows [7, 8]:

$$|V_{CKM,ij}| = \begin{pmatrix} 0.9742 \dots 0.9757 & 0.219 \dots 0.226 & 0.002 \dots 0.005 \\ 0.219 \dots 0.225 & 0.9734 \dots 0.9749 & 0.037 \dots 0.044 \\ 0.004 \dots 0.014 & 0.035 \dots 0.043 & 0.9990 \dots 0.9993 \end{pmatrix} \quad (2.14)$$

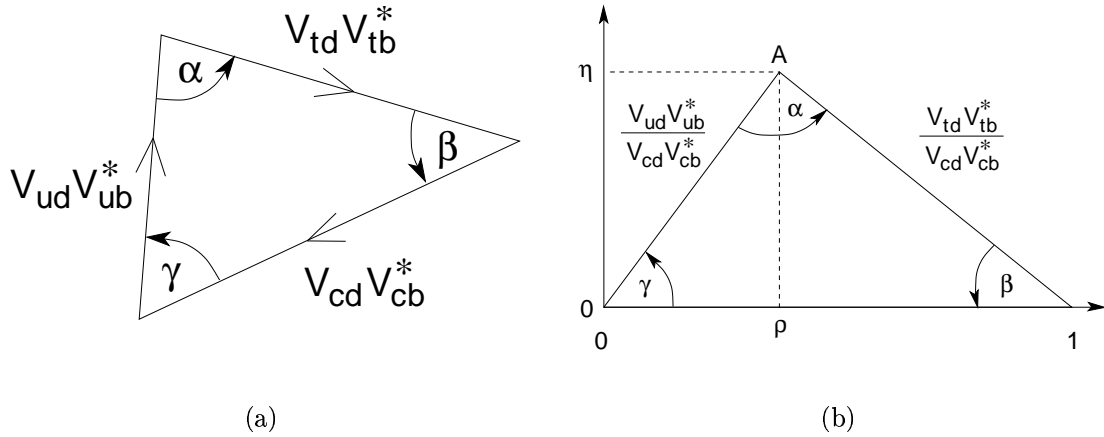


Figure 2.1: The unitarity triangle. **(a)** Three vectors in the complex plane form a triangle. **(b)** The unitarity triangle after division by $V_{cd}V_{cb}^*$.

2.1.3 The Strong Interaction

The strong interaction is described by Quantum Chromo Dynamics (QCD). Only quarks participate in the strong interaction. According to QCD each quark carries one of three *color charges*, either red, green or blue. The names are chosen in analogy to the color theorem in optical theory: only if the color states of two or more quarks would add up to *white* the formation of a bound state is possible. The corresponding gauge group is $SU(3)$, requiring eight gluons mediating the strong force. Each gluon carries one color and one anti-color charge. Due to the non abelian nature of the $SU(3)$ group gluons can couple to themselves. This results in a large number of graphs to be calculated in perturbation theory even for simple processes. Furthermore the strong coupling constant is very large at energy scales found in a bound meson state making perturbation theory very difficult or even impossible. Nevertheless it is often possible to make predictions either by directly solving the QCD equations (Lattice QCD) or by making use of other physical constraints like QCD sum rules, Light Cone Sum Rules (LCSR), Heavy Quark Symmetry (HQS), or by a combination of several techniques. The form-factor models introduced below make use of such techniques.

2.2 Semileptonic B Meson Decays

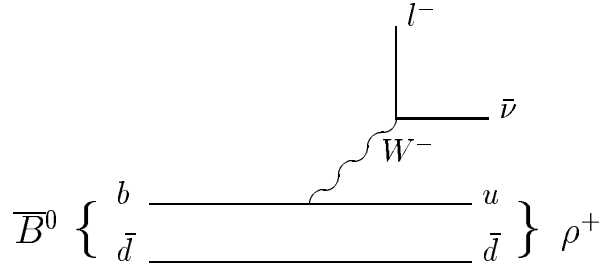


Figure 2.2: Feynman spectator diagram of the semileptonic decay $\bar{B}^0 \rightarrow \rho^+ \ell^- \bar{\nu}$.

The study of semileptonic B meson decays allows to measure the CKM matrix elements $|V_{cb}|$ and $|V_{ub}|$. The rates of $b \rightarrow c$ and $b \rightarrow u$ transitions are proportional to the squares of these matrix elements. Theoretically, the rate for $b \rightarrow u\ell\nu$ transitions is well known. Originally $|V_{ub}|$ has therefore been determined from the inclusive lepton momentum spectrum – blind to the particular decay mode. However the $b \rightarrow u\ell\nu$ rate is small compared to the $b \rightarrow c\ell\nu$ rate. With $|V_{ub}|/|V_{cb}| \approx 0.1$ and a phase space factor from a simple free quark model one finds $\Gamma(b \rightarrow u\ell\nu)/\Gamma(b \rightarrow c\ell\nu) \approx 2.0\%$ [9]. For this reason inclusive analyses are sensitive only in the endpoint region of the lepton-energy spectrum, which cannot be accessed by $b \rightarrow c\ell\nu$ decays for kinematical reasons. One needs to extrapolate to the entire lepton energy spectrum thereby introducing large theoretical uncertainties.

An alternative route to measure $|V_{ub}|$ is the exclusive reconstruction of particular $b \rightarrow u\ell\nu$ final states. Experimentally this provides some extra kinematical constraints for background suppression and theoretically the uncertainties are partly of a different nature. It is desirable to obtain a consistent measurement of $|V_{ub}|$ with both the inclusive and exclusive approach. The first exclusive measurement of the modes $B \rightarrow \rho(\omega, \pi)\ell\nu$ was presented by the CLEO collaboration [10, 11]. As an example Fig. 2.2 shows the spectator diagram associated to the decay $\bar{B}^0 \rightarrow \rho^+ \ell^- \bar{\nu}$. The extraction of $|V_{ub}|$ is complicated by the fact that the quarks are not free, but buried inside mesons. The probability that the final state quarks will form a given meson is described by form-factor models. The following sections describe five different form-factor models which have been studied in this analysis. Most form-factor models predict an overall normalization at a given value of q^2 , where $q = p_\ell + p_\nu$. p_ℓ and p_ν are the four momenta of the electron and the neutrino. Usually the normalization is predicted at $q^2 = q_{max}^2$, where the daughter meson is at rest in the parent meson rest frame, and then extrapolated to the entire q^2 range. In contrast to $b \rightarrow c\ell\nu$ decays the accessible q^2 range is larger and the extrapolation is much more difficult. Fig. 2.3 (a) shows the $d\Gamma/dq^2$ distribution for different models. The analysis presented here is most sensitive at high lepton energies above 2.3 GeV. For illustration Fig. 2.3 (b) shows the same distribution requiring that $E_\ell > 2.3$ GeV. All models are very similar in this region and the measured q^2 distribution does not allow to distinguish between the models. The main source of model dependency for the measured $B \rightarrow \rho\ell\nu$ branching fraction will be the fraction of events at high lepton energies. Table 2.2 shows the predicted fraction of events in the relevant lepton-energy regions for various form-factor models and Table 2.3 shows the predicted

overall normalization $\tilde{\Gamma}_{thy}$ for each model. $\tilde{\Gamma}_{thy}$ together with the life time of the B meson τ_{B^0} relates the branching fraction to $|V_{ub}|$:

$$|V_{ub}| = \sqrt{\frac{\mathcal{B}(B^0 \rightarrow \rho^- e^+ \nu)}{\tilde{\Gamma}_{thy} \tau_{B^0}}}. \quad (2.15)$$

This relation introduces another model dependence for determining $|V_{ub}|$.

model	$\Gamma(2 < E_\ell < 2.3 \text{ GeV})/\Gamma$	$\Gamma(E_\ell > 2.3 \text{ GeV})/\Gamma$	$\Gamma(E_\ell > 2 \text{ GeV})/\Gamma$
ISGW2	0.33	0.36	0.69
UKQCD	0.30	0.28	0.58
LCSR	0.28	0.24	0.53
Beyer/Melikhov	0.30	0.27	0.57
Ligeti/Wise	0.34	0.32	0.65

Table 2.2: Lepton-energy distribution for different form-factor models. The fraction of events found at high lepton energies is the primary source of model dependency in this analysis.

model	reference	$\tilde{\Gamma}_{thy}$ (ps^{-1})	estimated error on $\tilde{\Gamma}_{thy}$
ISGW2	[13]	14.2	$\pm 50\%$
UKQCD	[14]	16.5	$+21\%$ -14%
LCSR	[16]	16.9	$\pm 32\%$
Beyer/Melikhov	[19]	16.0	$\pm 15\%$
Ligeti/Wise	[20]	19.4	$\pm 29\%$

Table 2.3: Predicted values of $\tilde{\Gamma}_{thy}$ for different form-factor models. $\tilde{\Gamma}_{thy}$ relates the measured branching ratio to the matrix element $|V_{ub}|$ and therefore is a source of model dependence for determining $|V_{ub}|$. The error estimates are taken from the cited references.

2.2.1 Signal Decay Kinematics

The matrix element of the semileptonic decay $M_{Q\bar{q}} \rightarrow X_{q'\bar{q}} l^- \bar{\nu}$ of a pseudoscalar meson $M_{Q\bar{q}}$ to the hadron $X_{q'\bar{q}}$ can be written as the product of the leptonic and the more complicated hadronic currents [9]

$$M(M_{Q\bar{q}} \rightarrow X_{q'\bar{q}} l^- \bar{\nu}) = -i \frac{G_F}{\sqrt{2}} V_{q'Q} L^\mu H_\mu, \quad (2.16)$$

where $G_F/\sqrt{2} = g^2/(8M_W^2)$, M_W is the W boson mass, $L^\mu = \bar{u}_l \gamma^\mu (1 - \gamma_5) v_\nu$ is the leptonic current, and $H_\mu = \langle X_{q'\bar{q}} | \bar{q}' \gamma^\mu (1 - \gamma_5) Q | M_{Q\bar{q}} \rangle$ is the hadronic current. Strong interaction effects are isolated inside the hadronic current. There will be a dependence on theoretical models used to calculate the hadronic current.

The hadronic current must be constructed from the available four-vectors (momentum and spin-polarization vectors). The so formed Lorentz-invariant quantities have coefficients (form-factors) that are functions of the virtual W invariant mass

$$q^2 = m_W^2 = (p_l + p_{\bar{\nu}})^2 = (P - p_X)^2 = M^2 + m_X^2 - 2ME_X, \quad (2.17)$$

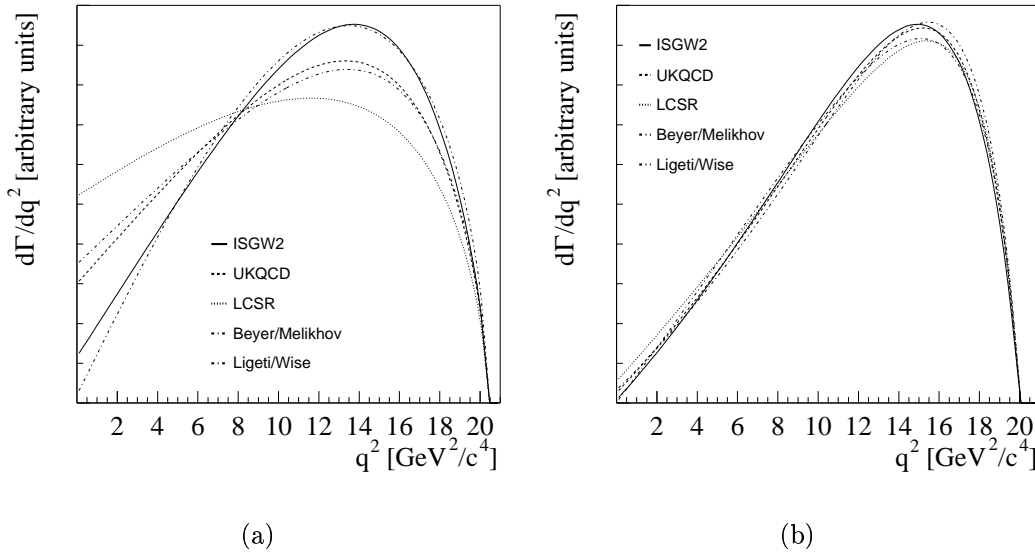


Figure 2.3: $d\Gamma/dq^2$ distribution for different form-factor models. All distributions are normalized to the same area. (a) for the entire lepton-energy range, (b) for $E_\ell > 2.3$ GeV. All models are very similar at high lepton energies.

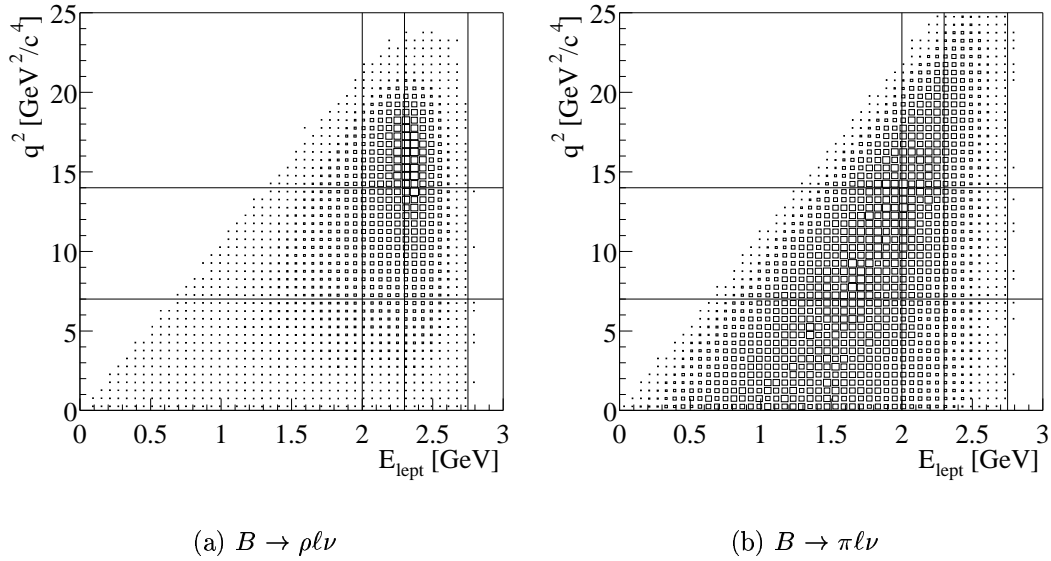


Figure 2.4: A Dalitz plot of q^2 vs. $E_{\text{lept}}^{\text{cm}}$ for the decays (a) $B \rightarrow \rho \ell \nu$ and (b) $B \rightarrow \pi \ell \nu$.

where P is the four-vector energy-momentum of the meson M , M its mass, and E_X the energy of the final meson X in the rest frame of M . Fig. 2.4 shows the Dalitz plot of the two decays $B^+ \rightarrow \rho^0 \ell^+ \nu$ and $B^+ \rightarrow \pi^0 \ell^+ \nu$ for the ISGW2 model. The spectrum for the decay to the scalar pion is much softer than the decay to a vector meson. A detailed discussion of the q^2 and lepton-energy spectrum for these decays can be found in [9].

The expressions of the hadronic current are given below for the cases of a final pseudoscalar meson and a vector meson [9].

(1) Case $P_{Q\bar{q}} \rightarrow P'_{q'\bar{q}} l \nu$ (for example $B^+ \rightarrow \pi^0 \ell^+ \nu$):

The hadronic current is described by two form-factors, $f^0(q^2)$ and $f^+(q^2)$

$$\begin{aligned} \langle P'(p') | V^\mu | P(p) \rangle &= f^+(q^2) \left[(p + p')^\mu - \frac{M^2 - m_{P'}^2}{q^2} q^\mu \right] \\ &+ f^0(q^2) \frac{M^2 - m_{P'}^2}{q^2} q^\mu. \end{aligned} \quad (2.18)$$

This expression can be simplified for leptons with small masses such as electrons and muons. In the limit of $m_l \ll M$, $q^\mu L_\mu = 0$, where L_μ is the leptonic current. The term proportional to q^μ can be neglected. The amplitude is then

$$\langle P'(p') | V^\mu | P(p) \rangle = f^+(q^2) (p + p')^\mu. \quad (2.19)$$

Using Eq. 2.19 one can calculate the differential decay rate:

$$\frac{d\Gamma}{dq^2} = \frac{G_F^2 |V_{q'Q}|^2 p_{P'}^3}{24\pi^3} |f^+(q^2)|^2, \quad (2.20)$$

where $p_{P'}$ is the momentum of the P' in the center of mass frame of the initial P meson

$$|\vec{p}_{P'}| = \sqrt{\left(\frac{M^2 + m_{P'}^2 - q^2}{2M} \right)^2 - m_{P'}^2}. \quad (2.21)$$

(2) Case $P_{Q\bar{q}} \rightarrow V_{q'\bar{q}} l \nu$ (for example $B^+ \rightarrow \rho^0 \ell^+ \nu$, $B^+ \rightarrow \omega \ell^+ \nu$):

The hadronic current is written in terms of four independent form-factors $A_1(q^2)$, $A_2(q^2)$, $V(q^2)$ and $A_0(q^2)$

$$\begin{aligned} \langle V(p', \varepsilon) | V^\mu - A^\mu | P(p) \rangle &= \frac{2iV(q^2)}{M + m_V} \epsilon^{\mu\nu\alpha\beta} \varepsilon_\nu^* p'_\alpha p_\beta \\ &- (M + m_V) A_1(q^2) \varepsilon^{*\mu} + \frac{A_2(q^2)}{M + m_V} (\varepsilon^* \cdot q) (p + p')^\mu \\ &+ 2A_3(q^2) m_V \frac{\varepsilon^* \cdot q}{q^2} q^\mu - 2A_0(q^2) m_V \frac{\varepsilon^* \cdot q}{q^2} q^\mu, \end{aligned} \quad (2.22)$$

where ε is the vector-meson polarization vector, m_P , m_V , p_P , and p_V are the pseudoscalar and vector-meson masses and four-momenta, $q \equiv p_P - p_V$, $A_0(0) = A_3(0)$ and

$$A_3 = \frac{M + m_V}{2m_V} A_1 - \frac{M - m_V}{2m_V} A_2. \quad (2.23)$$

A simplification can be made for leptons of small masses: the terms in q_μ vanish. Effectively there are only three form-factors $A_1(q^2)$, $A_2(q^2)$, $V(q^2)$ for electrons and muons. Instead of using these form-factors, the full differential decay rate is usually

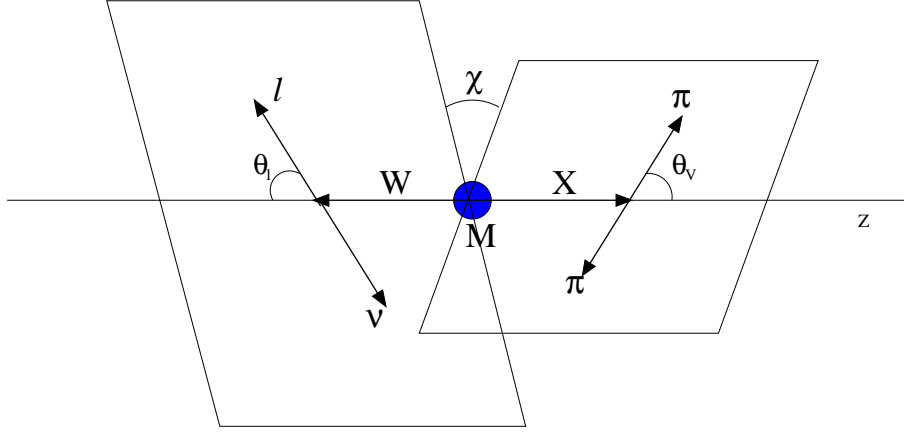


Figure 2.5: θ_ℓ is the polar angle of the lepton in the W rest frame with respect to the W flight direction in the B meson rest frame, and θ_V is the polar angle of one of the pseudoscalar daughters in the rest frame of the vector meson with respect to the vector-meson flight direction in the B meson rest frame. χ is the angle between the decay planes of the W and the vector meson.

expressed in terms of the amplitudes for the vector meson with helicity $+1$, -1 , or 0 , denoted by $H_+(q^2)$, $H_-(q^2)$, and $H_0(q^2)$

$$\begin{aligned}
 H_\pm(q^2) &= (M + m_V)A_1(q^2) \mp \frac{2M|\vec{p}_V|}{M + m_V}V(q^2), \\
 H_0(q^2) &= \frac{1}{2m_V\sqrt{q^2}}[(M^2 - m_V^2 - q^2)(M + m_V)A_1(q^2) \\
 &\quad - 4\frac{M^2|\vec{p}_V|^2}{M + m_V}A_2(q^2)], \tag{2.24}
 \end{aligned}$$

where \vec{p}_V is the momentum of the vector meson and is given by Eq. 2.21 replacing $m_{P'}$ by m_V . The full differential decay rate is then [9]

$$\begin{aligned}
 \frac{d\Gamma(P \rightarrow V l \nu, V \rightarrow P_1 P_2)}{dq^2 d \cos \theta_V d \cos \theta_\ell d \chi} &= \frac{3}{8(4\pi)^4} G_F^2 |V_{q'Q}|^2 \frac{|\vec{p}_V| q^2}{M^2} B(V \rightarrow P_1 P_2) \\
 &\times \left\{ (1 - \eta \cos \theta_\ell)^2 \sin^2 \theta_V |H_+(q^2)|^2 \right. \\
 &+ (1 + \eta \cos \theta_\ell)^2 \sin^2 \theta_V |H_-(q^2)|^2 \\
 &+ 4 \sin^2 \theta_\ell \cos^2 \theta_V |H_0(q^2)|^2 \\
 &- 4\eta \sin \theta_\ell (1 - \eta \cos \theta_\ell) \sin \theta_V \cos \theta_V \cos \chi H_+(q^2) H_0(q^2) \\
 &- 4\eta \sin \theta_\ell (1 + \eta \cos \theta_\ell) \sin \theta_V \cos \theta_V \cos \chi H_-(q^2) H_0(q^2) \\
 &\left. - 2 \sin^2 \theta_\ell \sin^2 \theta_V \cos 2\chi H_+(q^2) H_-(q^2) \right\}, \tag{2.25}
 \end{aligned}$$

where $q^2 = (p_P - p_V)^2$, θ_ℓ is the polar angle of the lepton in the W rest frame with respect to the W flight direction in the B meson rest frame, and θ_V is the polar angle of one of the pseudoscalar daughters in the rest frame of the vector meson with respect to the vector-meson flight direction in the B meson rest frame. χ is the angle between the decay planes of the W and the vector meson, see Fig. 2.5. The factor η is equal to $+1$ (-1) when the quark Q has charge $-1/3$ ($+2/3$).

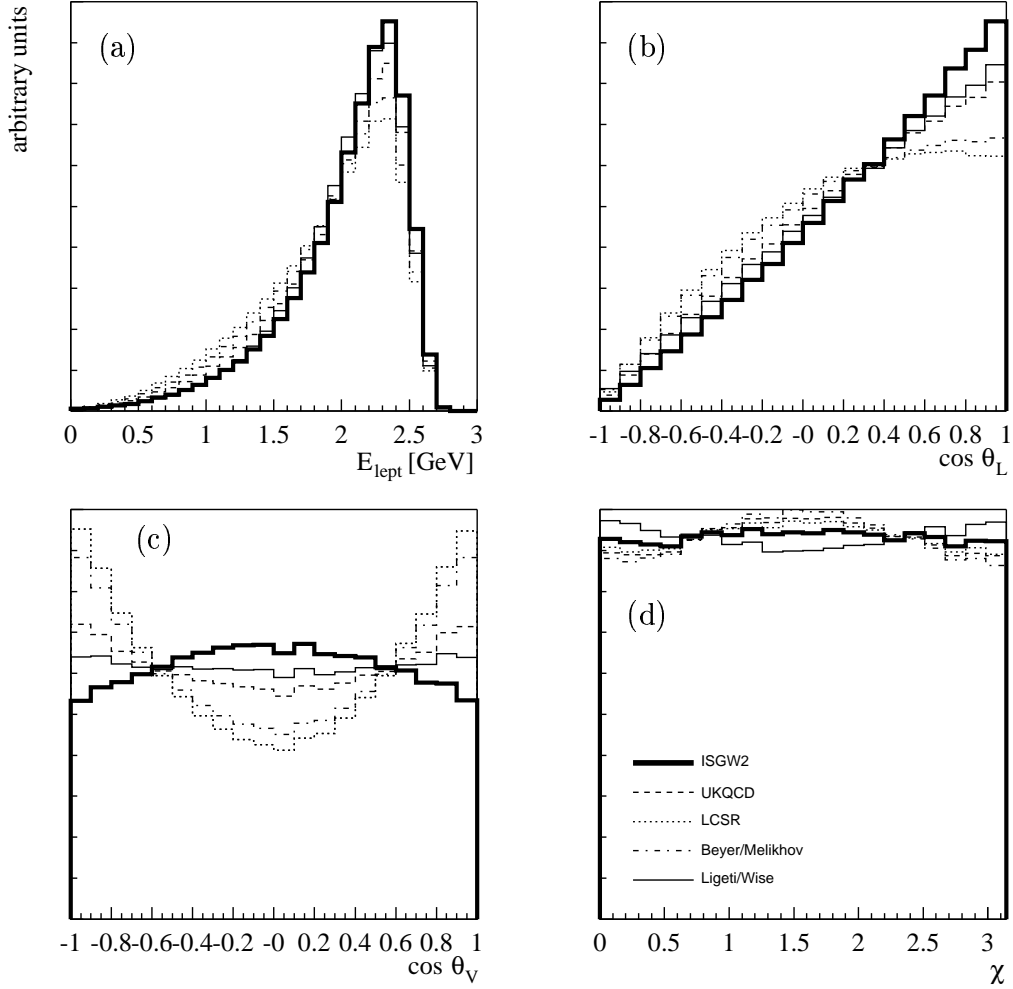


Figure 2.6: Kinematic distributions of the form-factor models: **(a)** lepton energy E_{lept} , **(b)** $\cos \theta_L$, **(c)** $\cos \theta_V$, and **(d)** χ . The angles are defined in Fig. 2.5. The following models are shown: ISGW2 model (bold solid line), UKQCD (dashed line), LCSR (dotted line), Beyer/Melikhov (dash dotted), and Ligeti/Wise (solid line).

Integrating over the angular variables, one finds

$$\frac{d\Gamma}{dq^2} = \frac{G_F^2}{96\pi^3} |V_{q'q}|^2 \frac{|\vec{p}_V| q^2}{m_P^2} \mathcal{B}(V \rightarrow P_1 P_2) \times \left[|H_+(q^2)|^2 + |H_-(q^2)|^2 + |H_0(q^2)|^2 \right], \quad (2.26)$$

where $\mathcal{B}(V \rightarrow P_1 P_2)$ is the branching fraction of the vector-meson decay. This analysis considers only a fraction of the lepton-energy spectrum in order to suppress the large backgrounds coming from the $b \rightarrow c\ell\nu$ modes. To determine the branching fractions of the signal channels, one needs to extrapolate to the full spectrum using the decay rates given above.

2.2.2 Form-Factor Models

The five form-factor models studied in this analysis are described in the following paragraphs. Fig. 2.6 shows the projections of various kinematic variables for each model. The

ISGW2 model shows the hardest lepton-energy spectrum, the Beyer/Melikhov model the softest spectrum. The q^2 spectrum has already been shown in Fig. 2.3. It is very similar for all models at high lepton energies.

Isgur Wise Model

The ISGW model proposed by Isgur, Scora, Grinstein and Wise [12] is a constituent quark model. It predicts a mix of resonant decay modes for $b \rightarrow u$ decays. Calculations are normalized at $q^2 = q_{max}^2$, where the daughter meson is at rest in the parent meson rest frame. The ISGW model was later updated to the ISGW2 [13] model, which incorporates several improvements. Constraints from heavy quark symmetry are now explicitly imposed. In particular constraints on form-factor ratios over the full q^2 range and on the slopes of form-factors near q_{max}^2 are considered. The model uses more realistic form-factor shapes and includes relativistic corrections to coupling constants of the axial vector current. It is hard to quantify systematic errors in this quark model approach. The authors estimate a theoretical error of 50% on the rate for $B \rightarrow \rho l \nu$.

The form-factor definitions used in the ISGW2 paper are as follows

$$\begin{aligned} f(q^2) &= A_1(q^2)(m_B + m_\rho) , \\ a_+(q^2) &= \frac{A_2(q^2)}{m_B + m_\rho} , \\ g(q^2) &= \frac{V(q^2)}{m_B + m_\rho} . \end{aligned} \tag{2.27}$$

The parametrization of the form-factors in this model is rather complex, see [13] for the full details.

UKQCD Model

The approach proposed by the UKQCD collaboration [14] uses lattice QCD techniques to calculate the form-factors on a discrete lattice of space-time points. All calculations are performed quenched¹ on a $24^3 \times 48$ lattice. Results are most reliable in the range $14 < q^2 < 21 \text{ GeV}^2/c^4$. Using light cone sum rules each of the form-factors are predicted to run like $m_B^{-3/2}$ at $q^2 = 0$. Heavy quark symmetry (HQS), at lowest order, is used to relate the form factors at high q^2 . Unlike in the case of heavy-to-heavy transitions HQS does not determine the overall normalization. Extra assumptions are needed to cover the full q^2 range. The use of a model by Stech [15], which satisfies all known constraints and fits the lattice data, leads to the following simplified HQS relations:

$$\begin{aligned} V(q^2) &= \left(1 + \frac{m_\rho}{m_B}\right) A_0(q^2) , \\ A_1(q^2) &= \frac{m_B^2 + m_\rho^2}{m_B(m_B + m_\rho)} \left(1 - \frac{q^2}{m_B^2 + m_\rho^2}\right) A_0(q^2) , \\ A_2(q^2) &= \frac{m_B + m_\rho}{m_B} \left(1 - \frac{2m_\rho(m_B + m_\rho)}{(m_B + m_\rho)^2 - q^2}\right) A_0(q^2) . \end{aligned} \tag{2.28}$$

¹Quenching means that virtual quark loops are neglected, thus reducing the amount of CPU time required to perform the calculation.

The lattice calculations on the four form-factors in $B \rightarrow \rho \ell \nu$ are thus used to effectively predict one form-factor. The results are extrapolated to low q^2 by fitting the function

$$A_1(q^2) = \frac{A_1(0)}{1 - q^2/M_1^2}, \quad (2.29)$$

with two fit parameters $A_1(0) = 0.27_{-0.04}^{+0.05}$ and $M_1 = 7.0_{-0.6}^{+1.2}$ GeV/ c^2 .

LCSR Model

A model using light-cone sum-rules was proposed by Ball and Braun [16]. The method of LCSR is a non perturbative approach, which combines ideas of QCD sum-rules [17] with twist-expansion characteristic of hard vector mesons at small values of q^2 [18]. The LCSR is complementary to QCD results which are most reliable at large q^2 . The model cited here includes radiative corrections, higher-twist corrections and $SU(3)$ -breaking effects. Form-factors are parametrized by the function

$$F(q^2) = \frac{F(0)}{1.0 - a(q^2/m_B^2) + b(q^2/m_B^2)^2}, \quad (2.30)$$

where $F(q^2)$ is $A_1(q^2)$, $A_2(q^2)$, or $V(q^2)$. Table 2.4 gives the values for $F(0)$, a , and b .

form-factor	$F(0)$	a	b
$A_1(q^2)$	0.261	0.29	-0.415
$A_2(q^2)$	0.223	0.93	-0.092
$V(q^2)$	0.338	1.37	0.315

Table 2.4: Values for the parameters $F(0)$, a , and b in the LCSR model. For a definition of the parameters see Eq. 2.30.

Beyer/Melikhov Model

The Beyer/Melikhov model [19] is a quark model similar to the ISGW2 model. It is however fully relativistic. Also the UKQCD lattice QCD results are used to normalize the form-factors at large q^2 . The form-factors are parametrized by

$$f(q^2) = \frac{f(0)}{1 - at^2 + bt^4}, \quad (2.31)$$

where $t^2 = q^2/M_{B^*}$, $M_{B^*} = 5.324$ GeV/ c^2 , and f is one of the form-factors defined in Eq. 2.27. The values for a , b and $f(0)$ are given in Table 2.5. The results are similar to the UKQCD model.

Ligeti/Wise Model

Ligeti and Wise propose to extract a model independent value for $|V_{ub}|$ by using the comparison of semileptonic exclusive B and D meson decays [20]. Their approach is valid

form-factor	$f(0)$	a	b
f	1.55	0.69	0.041
g	0.051	1.60	0.60
a_+	-0.04	1.40	0.50

Table 2.5: Values for the parameters $f(0)$, a , and b in the Beyer/Melikhov model. For a definition of the parameters see Eq. 2.31.

in the limit of $SU(3)$ flavor symmetry or in the limit of $SU(4)$ heavy quark spin-flavor symmetry. According to the authors the extraction of $|V_{ub}|$ is possible with a theoretical uncertainty of 10%, assuming that $SU(3)$ symmetry holds. Until further experimental data becomes available an additional uncertainty of 10% should be considered to take into account any possible breaking of $SU(3)$ symmetry [21].

The form-factors for $D \rightarrow K^* \ell \nu$ have been measured by the E791 collaboration [22]:

$$f^{(D \rightarrow K^*)}(w) = \frac{1.8 \text{ GeV}}{1 + 0.63(w - 1)}, \quad (2.32)$$

$$a_+^{(D \rightarrow K^*)}(w) = \frac{0.17 \text{ GeV}^{-1}}{1 + 0.63(w - 1)}, \quad (2.33)$$

$$g^{(D \rightarrow K^*)}(w) = \frac{0.51 \text{ GeV}^{-1}}{1 + 0.96(w - 1)}, \quad (2.34)$$

where

$$w = v_D \cdot v'_{K^*} = \frac{m_D^2 + m_{K^*}^2 - q^2}{2m_D m_{K^*}}. \quad (2.35)$$

The form-factor a_- is not measured because its contribution to the $D \rightarrow K^* \ell \nu$ decay amplitude is proportional to the lepton mass. See Eq. 2.27 for the definition of the form-factors f , a_+ and g . Heavy quark symmetry relates the $D \rightarrow K^*$ form-factors to the $B \rightarrow K^*$ form-factors:

$$f^{(B \rightarrow K^*)}(w) = \sqrt{\frac{m_B}{m_D}} \left(\frac{\alpha_s(m_b)}{\alpha_s(m_c)} \right)^{-6/25} f^{(D \rightarrow K^*)}(w), \quad (2.36)$$

$$a_+^{(B \rightarrow K^*)}(w) = \sqrt{\frac{m_D}{m_B}} \left(\frac{\alpha_s(m_b)}{\alpha_s(m_c)} \right)^{-6/25} a_+^{(D \rightarrow K^*)}(w), \quad (2.37)$$

$$g^{(B \rightarrow K^*)}(w) = \sqrt{\frac{m_D}{m_B}} \left(\frac{\alpha_s(m_b)}{\alpha_s(m_c)} \right)^{-6/25} g^{(D \rightarrow K^*)}(w). \quad (2.38)$$

The approximation $a_-^{(D \rightarrow K^*)} = -a_+^{(D \rightarrow K^*)}$ has been used. $SU(3)$ symmetry implies that the $B \rightarrow \rho$ form-factors are equal to the $B \rightarrow K^*$ form-factors. In the implementation of this model $\alpha_s(m_c) = 0.39$ and $\alpha_s(m_b) = 0.22$ is used. Note that f is most reliable in the range $1 < w < 1.3$ which is accessible for $D \rightarrow K^* \ell \nu$ decays. Nevertheless, since f changes only slightly in this range, the extrapolation is used over the entire range $1 < w < 3.5$ which is accessible for $B \rightarrow \rho \ell \nu$ decays.

Chapter 3

The *BABAR* Experiment

3.1 Introduction

The primary goal of the *BABAR* experiment is to discover and precisely measure the violation of CP symmetry in the B meson system. In addition, measurements of decay channels which are not expected to violate the CP symmetry can be used to over-constrain the unitarity triangle and either confirm a consistent picture within the Standard Model or give hints at new physics. As outlined below, several requirements must be fulfilled to achieve these two goals.

At the storage ring PEP-II, pairs of B mesons are produced in the decay of the $\Upsilon(4S)$ meson $e^+e^- \rightarrow \Upsilon(4S) \rightarrow B\bar{B}$, where $B\bar{B}$ is either a charged or a neutral pair of B mesons. The B mesons are produced in a coherent two particle state. The flavor (B or \bar{B}) of each B meson is well defined when the other B has decayed. To measure time-dependent asymmetries, one needs to measure the position of the decay vertex of each B meson and also gain knowledge on the flavor of the decaying B mesons (*tagging*). Since the B meson life-time is small and the mesons are produced almost at rest, asymmetric beam energies are needed to infer the life time of the B mesons from their decay length. At PEP-II, electrons of 9.0 GeV are collided with positrons of 3.1 GeV, corresponding to a boost $\beta\gamma = 0.55$ in positive z direction. Besides asymmetric beam-energies and an excellent vertex-detector, a good particle identification system and very high luminosities are needed to select the CP-violating decay channels which typically have a branching fraction of the order 10^{-4} . For the analysis presented in this thesis the fact that the beam energies are asymmetric is not relevant, since time-dependent observables are not measured. The *BABAR* detector has been designed as a general purpose detector which allows a multitude of measurements. The detector is described in more detail in the following sections. The most detailed description can be found in [23]. The experiment started its operation in May 1999.

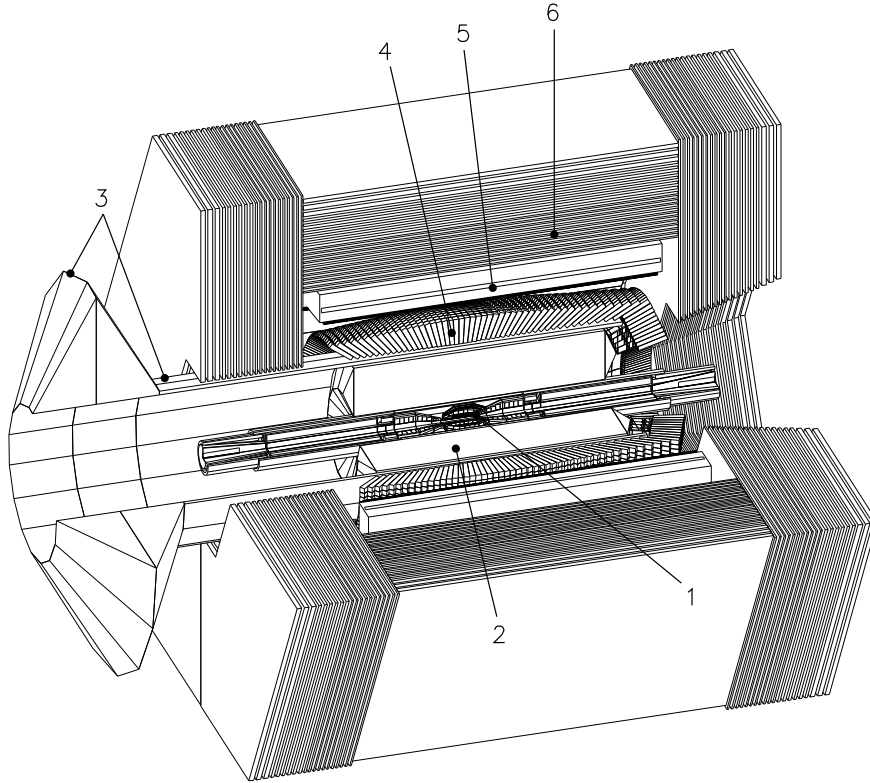


Figure 3.1: Schematic view of the *BABAR* detector. (1) Silicon Vertex Tracker, SVT, (2) Drift Chamber, DCH, (3) Cherenkov Detector, DIRC, (4) Electromagnetic Calorimeter, EMC, (5) Magnet Coil, (6) Instrumented Flux Return, IFR. The high energetic electrons enter the detector from the left and move in positive z direction.

3.2 The *BABAR* Detector

Fig. 3.2 shows the acceleration and storage system at PEP-II. Particles collide at a center of mass energy $E_{cm_s} = 10.58$ GeV in the interaction region, which is slightly offset in negative z direction with respect to the center of the detector to take account of the asymmetric nature of PEP-II. A schematic view of the *BABAR* detector is shown in Fig. 3.1. The decay products first traverse the SVT (Silicon Vertex Tracker) which is contained in the support tube, then the DCH (Drift CHamber), the DIRC (Detector for Internally Reflected Cherenkov light), the EMC (ElectroMagnetic calorimeter), the magnetic superconducting coil providing a magnetic field of 1.5 T, and finally the IFR (Instrumented Flux Return).

3.2.1 Silicon Vertex Tracker

The Silicon Vertex Tracker (SVT) shown in Fig. 3.3 allows to reconstruct the two B meson vertices with a precision of approximately $70 \mu\text{m}$ for a fully reconstructed B meson and $140 \mu\text{m}$ for the tag- B vertex. This is sufficient for the time-dependent CP asymmetry and mixing measurements since the average separation of the two B mesons is approximately $250 \mu\text{m}$.

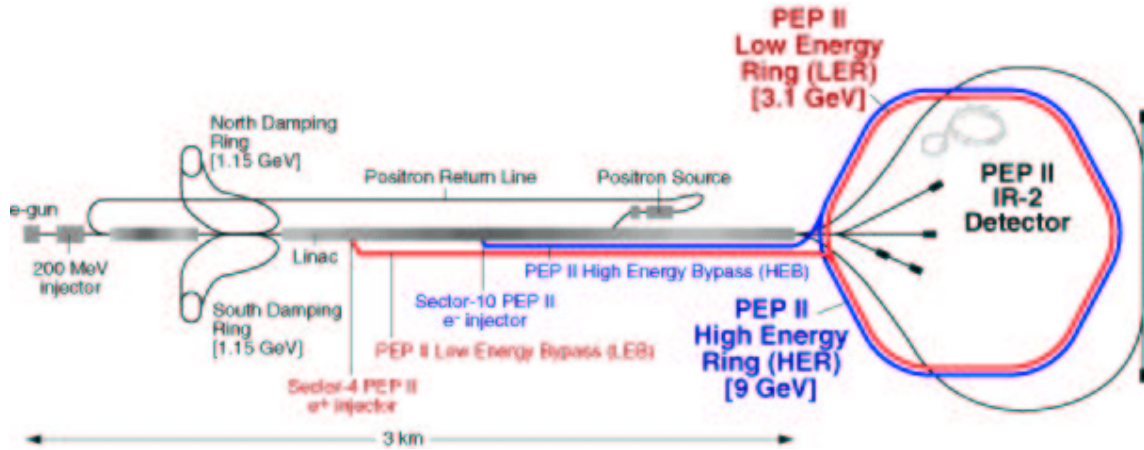


Figure 3.2: Schematic view of the acceleration and storage system of PEP-II. Electrons and positrons are accelerated to their nominal energy by the SLC (Stanford Linear Collider) prior to their injection into the two separate storage rings.

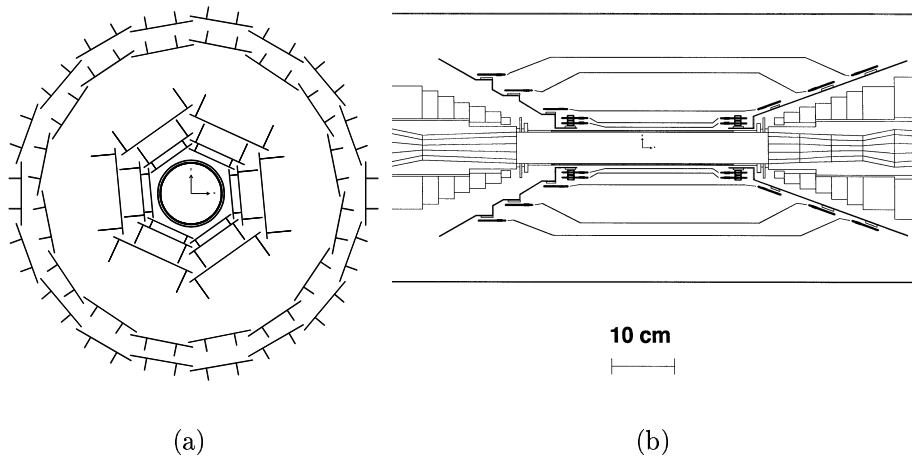


Figure 3.3: Schematic view of the Silicon Vertex Tracker, SVT, (a) xy-view, (b) xz-view.

The SVT consists of 5 concentric cylindrical layers of silicon microstrip detectors with radii between 32 mm and 144 mm and covers a polar angle of 20.1° to 150.2° . Each layer is divided azimuthally into overlapping detector modules to provide full azimuthal coverage. The innermost layers close to the interaction point are most important for a precise track reconstruction. They have a point resolution of $10\text{--}15\ \mu\text{m}$. The outer layers with a resolution of $30\text{--}40\ \mu\text{m}$ are important for pattern recognition and matching with DCH tracks. The track reconstruction uses both information from SVT and DCH to obtain a high track efficiency. Tracks found in the drift chamber are extrapolated to the SVT and matched with SVT hits and vice versa. Low momentum tracks, mainly slow pions with $p_t < 100\ \text{MeV}/c$ from D^* decays, do not reach the DCH and are reconstructed separately using the remaining SVT hits.

3.2.2 Drift Chamber

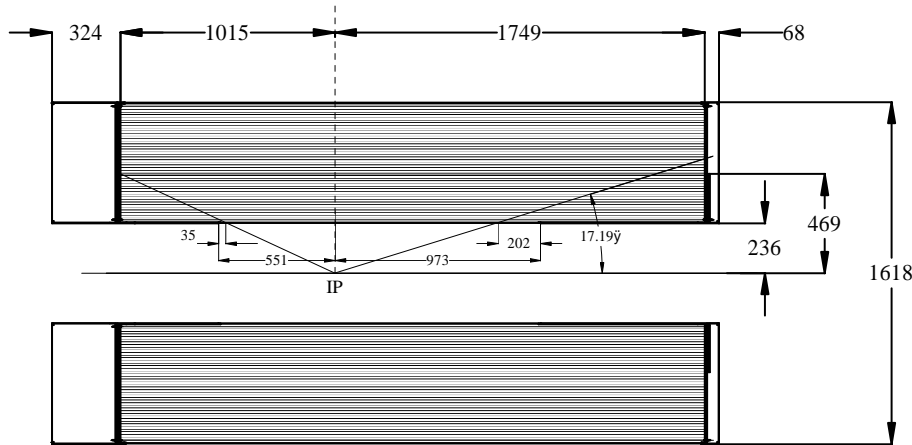


Figure 3.4: Schematic xz-view of the drift chamber DCH

The drift chamber, DCH, is the main tracking device of the detector. It measures the direction and momentum of particles with $p_t > 100 \text{ MeV}/c$ with high efficiency and a spatial resolution of better than $140 \mu\text{m}$, and also provides a dE/dx measurement with a resolution of 7%. For tracks with $p_t > 1 \text{ GeV}/c$, the momentum resolution is $\sigma_{p_t} \approx 0.3\% \cdot p_t$. The angular polar acceptance in the laboratory frame is $17^\circ < \theta < 150^\circ$.

A schematic side view of the DCH is shown in Fig. 3.4. The DCH is a 280-cm long cylinder with an inner radius of 26.6 cm and an outer radius of 80.9 cm. There are 7104 hexagonal drift cells with a typical dimension of $1.2 \times 1.8 \text{ cm}^2$ arranged in 10 super-layers with 4 layers each. The sense wires are made of gold-plated Tungsten-rhenium and have a diameter of $20 \mu\text{m}$. Each wire is surrounded by six $80 - 100 \mu\text{m}$ -thick aluminum field wires. The wires within different super-layers show different stereo angles. There are axial (A), positive (U), and negative (V) stereo angles with their absolute value increasing with radius of each layer. The arrangement follows the pattern AUVAUVAUVA. The chamber is operated with a mixture of Helium and Isobutane in the ratio 80% : 20%. The voltage of the sense wires has been 1960 V originally, but has been varied later, first to 1900 V and finally to 1930 V.

3.2.3 Cherenkov Detector

The DIRC, Detector for Internally Reflected Cherenkov light, is a Cherenkov detector with a novel design. Its primary goal is the pion and kaon separation to enhance the flavor tagging of the non-CP B meson and to distinguish between different CP channels. In the analysis presented in this thesis, it is used as a kaon veto for the pion selection. The DIRC provides excellent kaon identification up to momenta of about $2 \text{ GeV}/c$. Kaons start radiating Cherenkov photons above $460 \text{ MeV}/c$.

A schematic view of the DIRC is shown in Fig. 3.5. The detector consists of 144 bars of synthetic quartz arranged in a 12-sided polygonal barrel shape. The bars are 4.9 m

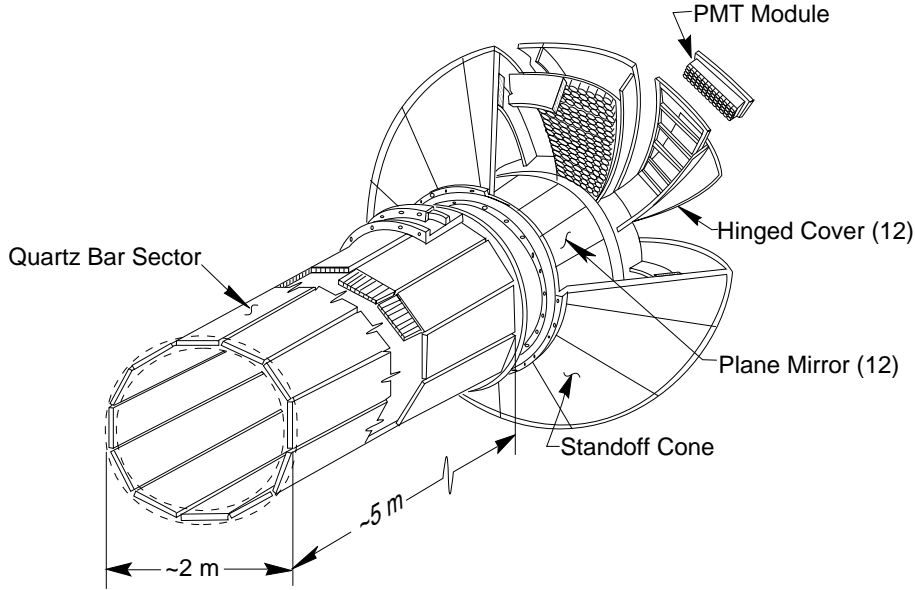


Figure 3.5: Schematic view of the Cherenkov detector, DIRC.

long and have a $1.7 \times 3.5 \text{ cm}^2$ rectangular cross-section. The angular coverage in the center of mass frame is 87% in polar angle and 93% in azimuthal angle. The DIRC is located just inside the calorimeter. The total amount of material at normal incidence corresponds to 19% of a radiation length. The working principle of the DIRC is shown in Fig. 3.6 (a). When charged particles traverse the quartz bars, Cherenkov radiation is emitted at the angle

$$\cos \theta_C = \frac{\sqrt{(1 + (m/p)^2)}}{n}, \quad (3.1)$$

where $n = 1.453$ is the refractive index of the radiator medium. The photons are captured by internal total reflection and transported to the Stand Off Box (SOB) at the backward end of the detector, where the Cherenkov image is allowed to expand in a tank of 6 m^3 purified water before it is projected on an array of 11,000 photo-multiplier tubes (PMTs). Each PMT has a diameter of 2.82 cm with an average distance of 1.2 m to the end of the quartz bars. Except for a number of discrete ambiguities, the Cherenkov angle is preserved during this process. Measurements of the photon arrival time and pattern recognition algorithms are used to resolve these ambiguities. The angle $\cos \theta_C$ together with the measured momentum from the drift chamber delivers a mass hypothesis for the particle. A simulated event display with Cherenkov rings visible by the pure eye is shown in Fig. 3.6 (b). The achieved 2.4 mrad θ_C resolution at $p = 4 \text{ GeV}/c$ allows for a three σ separation between kaons and pions.

3.2.4 Electromagnetic Calorimeter

The Electromagnetic Calorimeter EMC is used for electron-pion separation and the reconstruction of photons and neutral pions. It measures the position of the particle's impact point, the deposited energy and the cluster shape. On average, generic B meson decays contain 5.5 photons with about half of the photon energies below 250 MeV.

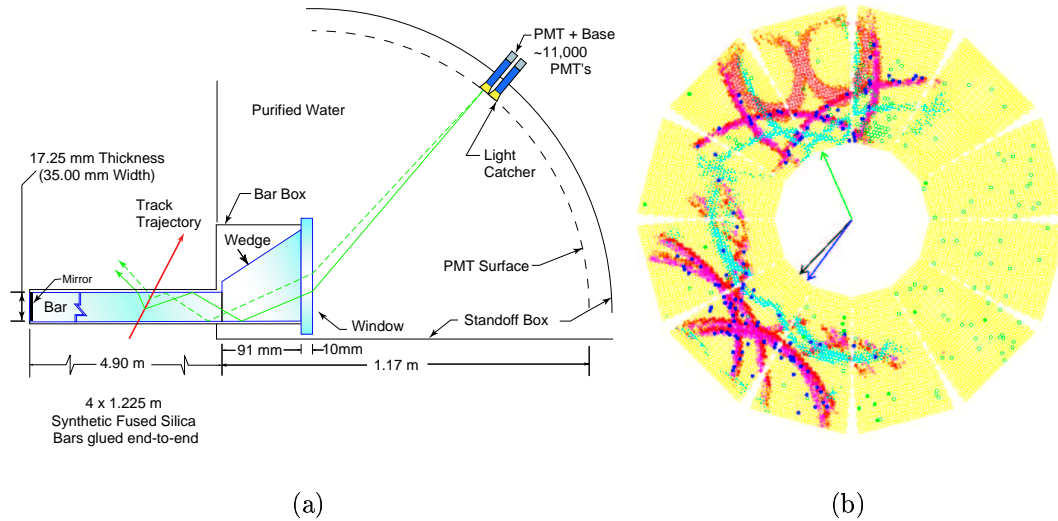


Figure 3.6: Working principle of the DIRC. (a) Sketch of the photon path, and (b) the display of a simulated event.

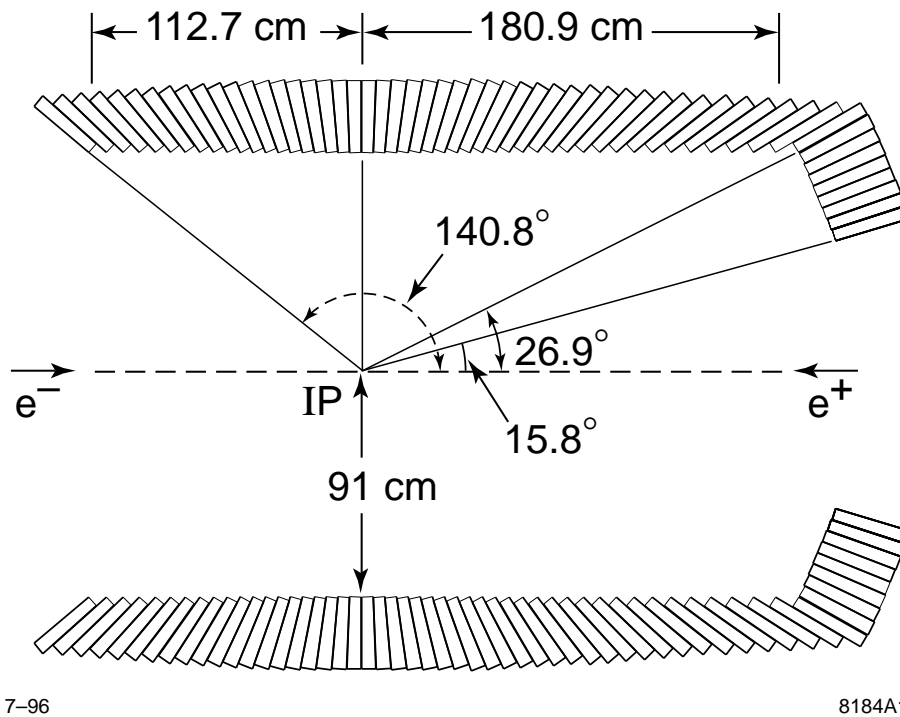


Figure 3.7: Schematic side view of the electromagnetic calorimeter, EMC. The EMC consists of a cylindrical barrel with 5760 CsI crystals and a forward conic endcap with 820 crystals.

The EMC was therefore designed to measure photons at very low energies, down to approximately 10 – 20 MeV. The measurement of the deposited energy and the clus-

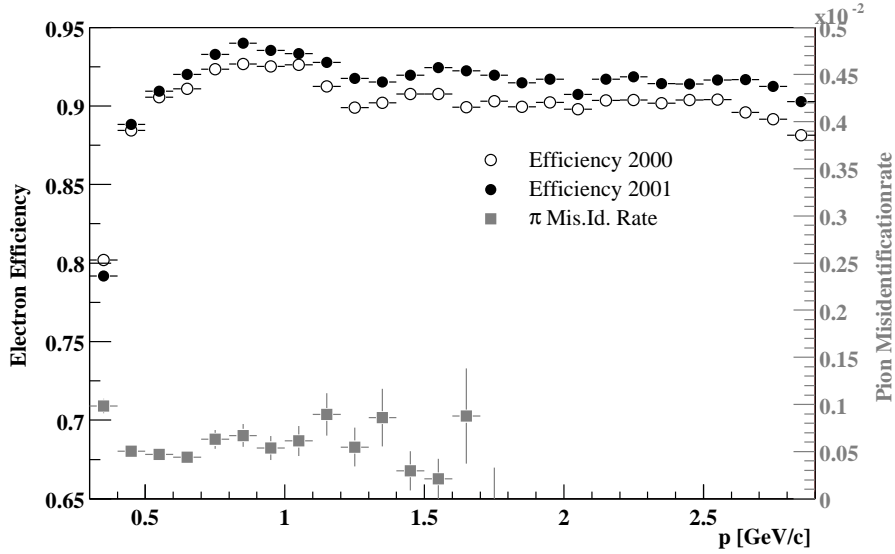


Figure 3.8: Electron efficiency and pion misidentification rate. Note that the misidentification rate uses a different scale.

ter shape allows for an excellent electron identification with high efficiency and low misidentification rate. An energy resolution of

$$\frac{\sigma_E}{E} = \frac{(2.32 \pm 0.30)\%}{\sqrt[4]{E(\text{ GeV})}} \oplus (1.85 \pm 0.12)\% \quad (3.2)$$

and an angular resolution for the polar angle θ and the azimuthal angle ϕ of

$$\sigma_\theta = \sigma_\phi = \left(\frac{3.87 \pm 0.07}{\sqrt{E(\text{ GeV})}} \pm 0.04 \right) \text{ mrad} \quad (3.3)$$

has been achieved. Fig. 3.8 shows the electron identification efficiency and pion misidentification rate as a function of the electron momentum [29]. In the energy region above 2 GeV, which is relevant for the analysis presented here, the efficiency (misidentification rate) is approximately 92% (0.001%). The efficiencies and misidentification rates have been determined from pure data control samples. The efficiency in the year 2001 is higher due to improvements of the calorimeter electronics.

The EMC consists of 6580 crystals made of CsI(Tl) with a cylindrical barrel section ($26.9^\circ < \theta < 140.8^\circ$, 48 rows with 120 crystals in ϕ direction each) and a forward conic endcap ($15.8^\circ < \theta < 26.9^\circ$, 820 crystals arranged in 8 rings). The crystals are of trapezoidal shape with typical transverse dimensions of $47 \times 47 \text{ mm}^2$ at the front face, flaring out towards the back to about $60 \times 60 \text{ mm}^2$. The barrel has an inner radius of 91 cm and an outer radius of 136 cm. It is located inside the magnet cryostat. The crystals are grouped in 280 modules, each spanning 7×3 crystals in θ and ϕ . The modules are made from $300 \text{ }\mu\text{m}$ - thick carbon fiber composite material. The crystals are supported from the back to minimize amount of material in front of them. Due to the short radiation length ($X_0 = 1.85 \text{ cm}$) and small Molière radius ($R_m = 3.8 \text{ cm}$) of the CsI crystals, electromagnetic clusters are almost fully contained in the detector and can be measured precisely. To account for the boost, which leads to higher energies at

smaller polar angles, the crystal lengths increase from 29.76 cm ($16.1X_0$) in the backward region to 32.55 cm ($17.6X_0$) in the endcap. Mounted on the back of each crystal, two silicon PIN diodes, covering an area of 4 cm^2 , collect scintillation light. Preamplifiers are connected to each diode. The angular coverage of the EMC in the center of mass frame (laboratory frame) is $-0.916 < \cos(\theta^*) < 0.895$ ($-0.775 < \cos(\theta) < 0.962$).

3.2.5 Instrumented Flux Return

The Instrumented Flux Return IFR has been instrumented with Resistive Plate Chambers (RPCs) to identify muons and neutral hadrons such as the K_L meson. It consists of a central barrel part and two endcap plugs as shown in Fig. 3.9. The angular coverage is 300 mrad in the forward and 400 mrad in the backward direction. The iron is segmented in 18 plates with a total thickness of 65 cm in the barrel and 60 cm in the endcaps. A novel feature is the graded segmentation which varies from 2 cm for the inner plates to 10 cm for the outermost plates. Monte Carlo studies have shown that the K_L identification can be improved in this way. In the barrel region, there are 21 active detector layers: a double layer of cylindrical RPCs between the solenoidal coil and the electromagnetic calorimeter, an inner layer of planar RPCs between the solenoidal coil and the iron, 17 layers in the gaps, and one last layer outside the iron structure. The total area covered by the detector exceeds 1000 m^2 . The active volume is filled with a gas mixture based on comparable quantities of Argon and Freon 134A ($C_2H_2F_4$) and a small amount of Isobutane. The chambers work in streamer mode.

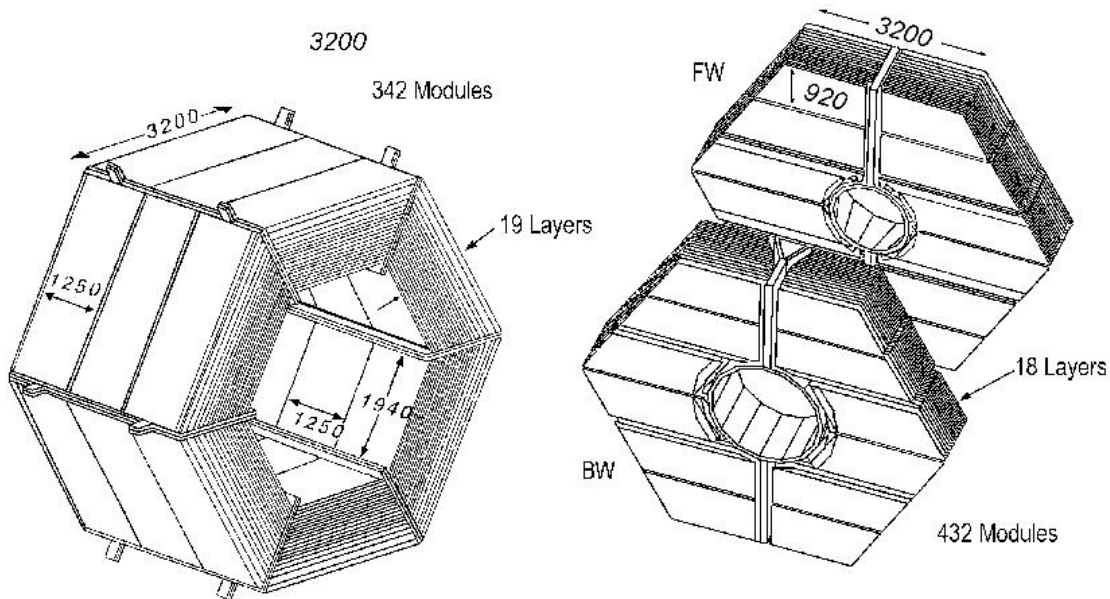


Figure 3.9: Schematic view of the instrumented flux return, IFR, barrel (left) and endcaps (right).

Chapter 4

Analysis Strategy

This chapter describes the data sets used in this analysis and the Monte Carlo simulations used to model the data. The event selection criteria and the applied fit method are described in detail.

4.1 Dataset

Table 4.1 shows a summary of all data subsets used. The total luminosity is 50.5 fb^{-1} on-resonance data (corresponding to 55.2 million $B\bar{B}$ meson pairs) and 7.7 fb^{-1} off-resonance data. The off-resonance data have been recorded at an energy of $40 \text{ MeV}/c^2$ below the $\Upsilon(4S)$ mass.

The number of $B\bar{B}$ events was obtained by subtracting the luminosity scaled number of loosely selected multihadron events in on- and off-resonance data samples, and dividing by the $B\bar{B}$ selection efficiency as determined from Monte Carlo simulations. This was done in a separate study which is described in [24]. The number of $B\bar{B}$ events is known with a systematic precision of 1.6%.

The luminosity of each datasample has been obtained by counting Bhabha and dimuon events in the central detector region. The details of this study are described in [25]. The absolute luminosities are known with a precision of 1.5%. The ratio of on- and off-resonance luminosities, which is relevant for this analysis, is known to even better precision.

4.2 Monte Carlo Simulation

This analysis uses Monte Carlo events which have been produced by the *BABAR* collaboration at SLAC, in Rutherford, in Dresden and at many other computing centers. In addition a large part of the signal Monte Carlo samples have been produced privately in Dresden. The simulation uses the simulation package Geant4 [26].

year-block-subset	luminosity [pb^{-1}]	# $B\bar{B}$ pairs [10^6]
2000-b1-s0-r10B-on	2165	2.223
2000-b1-s0-r10B-off	141	<i>off-res.</i>
2000-b1-s1-r10B-on	281	0.295
2000-b1-s2-r10B-off	1069	<i>off-res.</i>
2000-b1-s2-r10B-on	8258	9.006
total block 1	on: 10.704 (off: 1.210)	11.524
2000-b2-s0-r10B-on	1900	2.043
2000-b2-s0-r10B-off	399	<i>off-res.</i>
2000-b2-s1-r10B-on	898	0.975
2000-b2-s2-r10B-on	6774	7.370
2000-b2-s2-r10B-off	1003	<i>off-res.</i>
total block 2	on: 9.572 (off: 1.402)	10.388
total year 2000	on: 20.276 (off: 2.612)	21.912
2001-b1-s2-r10A-on	10581	11.669
2001-b1-s2-r10A-off	1419	<i>off-res.</i>
2001-b1-s3-r10A-on	6807	7.400
2001-b1-s3-r10A-off	1052	<i>off-res.</i>
2001-b1-s4-r10B-on	4673	5.163
2001-b1-s5-r10B-on	3982	4.395
2001-b1-s6-r10B-on	4193	4.626
2001-b1-s6-r10B-off	1315	<i>off-res.</i>
total year 2001	on: 30.236 (off: 3.786)	33.253
2002-b1-s0-r10B-off	1337	<i>off-res.</i>
2002-b1-s2-r10B-off	923	<i>off-res.</i>
total year 2002	off: 2.260	
total	on: 50.512 (off: 8.658)	55.165

Table 4.1: Summary of all data runs used in this analysis. For year 2000 block 1 corresponds to data taken with the DCH voltage at 1900V and block 2 at 1960V. In the years 2001 and 2002 the DCH voltage was 1930V.

Table 4.2 shows a summary of all Monte Carlo events used. The *generic* sample contains events where both B mesons decay generically. The so called *hard-lepton* sample is identical to the generic sample, but it requires at least one lepton with $E_{lept}^{cm} > 1.5$ GeV on generator level. For this analysis a dedicated *very hard-lepton* sample has been produced requiring a lepton with $E_{lept}^{cm} > 2.2$ GeV. The *no-charm* sample is used to enhance the statistics for the $b \rightarrow u$ downfeed component. In this sample one B meson is required to decay into a light quark ($b \rightarrow u$).

All signal modes have been generated using the ISGW2 model [13]. In addition to the ISGW2 model the signal Monte Carlo samples have also been generated with a uniform distribution in phase space. These samples are used to simulate different form-factor models using a reweighting technique (see section 4.5).

type	# events	luminosity equivalent [fb ⁻¹]	assumed br. fraction or σ
generic B^+B^-	$25.118 \cdot 10^6$	46	$\sigma_{b\bar{b}} = 1.1$ nb
generic $B^0\bar{B}^0$	$26.034 \cdot 10^6$	47	$\sigma_{b\bar{b}} = 1.1$ nb
hard-lepton B^+B^-	$21.361 \cdot 10^6$	39	$\sigma_{b\bar{b}} = 1.1$ nb
hard-lepton $B^0\bar{B}^0$	$21.504 \cdot 10^6$	39	$\sigma_{b\bar{b}} = 1.1$ nb
very hard-lepton B^+B^-	$179.783 \cdot 10^6$	327	$\sigma_{b\bar{b}} = 1.1$ nb
very hard-lepton $B^0\bar{B}^0$	$190.554 \cdot 10^6$	346	$\sigma_{b\bar{b}} = 1.1$ nb
no-charm $B^0\bar{B}^0$	$108.659 \cdot 10^6$	99	$\sigma_{b\bar{b}} = 1.1$ nb
$B^+ \rightarrow \rho^0 \ell^+ \nu + \text{CC ISGW2}$	556000	≈ 1944	$1.3 \cdot 10^{-4}$
$B^0 \rightarrow \rho^- \ell^+ \nu + \text{CC ISGW2}$	609200	≈ 1065	$2.6 \cdot 10^{-4}$
$B^+ \rightarrow \pi^0 \ell^+ \nu + \text{CC ISGW2}$	140000	≈ 707	$0.9 \cdot 10^{-4}$
$B^0 \rightarrow \pi^- \ell^+ \nu + \text{CC ISGW2}$	176000	≈ 444	$1.8 \cdot 10^{-4}$
$B^+ \rightarrow \omega \ell^+ \nu + \text{CC ISGW2}$	341200	≈ 1193	$1.3 \cdot 10^{-4}$
$B^+ \rightarrow \rho^0 \ell^+ \nu + \text{CC PHSP}$	1277500	≈ 4467	$1.3 \cdot 10^{-4}$
$B^0 \rightarrow \rho^- \ell^+ \nu + \text{CC PHSP}$	1262200	≈ 2207	$2.6 \cdot 10^{-4}$
$B^+ \rightarrow \omega \ell^+ \nu + \text{CC PHSP}$	639000	≈ 2234	$1.3 \cdot 10^{-4}$
$c\bar{c}$	$50 \cdot 10^6$	≈ 38	$\sigma_{c\bar{c}} = 1.3$ nb
$u\bar{u}, d\bar{d}, s\bar{s}$	$88 \cdot 10^6$	≈ 42	$\sigma_{u\bar{u}, d\bar{d}, s\bar{s}} = 2.1$ nb

Table 4.2: Summary of all Monte Carlo samples used in this analysis. The (*very*) *hard-lepton* sample is generated from generic $B\bar{B}$ events requiring a lepton with $p^* > 1.5$ GeV/ c ($p^* > 2.2$ GeV/ c). In the *no-charm* sample one B meson always decays as $b \rightarrow u$. The higher mass $b \rightarrow u\ell\nu$ states are contained in the *generic*, *hard-lepton*, *very hard-lepton*, and *no-charm* samples.

The other resonant $b \rightarrow u$ modes, which contribute as downfeed background in this analysis, have been generated according to the ISGW2 model. The branching fractions that have been used for all semileptonic $b \rightarrow u\ell\nu$ decays are shown in Tables 4.3 and 4.4. The dominant decay modes and branching fractions for the a , f , b , h and η mesons used in the Monte Carlo simulation are listed in Tables 4.5, 4.6 and 4.7. Besides the resonant $b \rightarrow u$ modes there is a non-resonant contribution. The model implemented here is described in [27]. The particle X_u in tables 4.3 and 4.4 represents the non-resonant semileptonic $b \rightarrow u\ell\nu$ modes. Table 4.8 lists the inclusive $b \rightarrow u\ell\nu$ branching fraction as measured by different experiments.

The decays $B \rightarrow D^*\ell\nu$ have been simulated using heavy quark effective theory (HQET). The modes $B \rightarrow D^*\pi\ell\nu$ are simulated according to the Goity Roberts model [28]. All other resonant $b \rightarrow c\ell\nu$ modes are implemented according to the ISGW2 model. The inclusive $b \rightarrow c\ell\nu$ rate was originally taken as 10.4%, but has been rescaled to 10.85% corresponding to the latest *BABAR* measurement [29]. The dominating background arises from $B \rightarrow D^*\ell\nu$ decays. The branching fractions used for various background modes are listed in Table 4.9.

A comparison of continuum Monte Carlo simulation to off-resonance data shows discrepancies in the normalization and shape of some distributions. Therefore continuum

B^0 decay	branching fraction
$B^0 \rightarrow \rho^\pm l\nu$	$2.60 \cdot 10^{-4}$
$B^0 \rightarrow \pi^\pm l\nu$	$1.80 \cdot 10^{-4}$
$B^0 \rightarrow a_0^\pm l\nu$	$0.36 \cdot 10^{-4}$
$B^0 \rightarrow a_1^\pm l\nu$	$4.11 \cdot 10^{-4}$
$B^0 \rightarrow a_2^\pm l\nu$	$0.36 \cdot 10^{-4}$
$B^0 \rightarrow b_1^\pm l\nu$	$2.55 \cdot 10^{-4}$
$B^0 \rightarrow X_u^\pm l\nu$	$4.62 \cdot 10^{-4}$
Total	$16.40 \cdot 10^{-4}$

Table 4.3: Branching fractions of the generated $B^0 \rightarrow H_u l\nu$ decay modes. The leptons are electrons or muons.

B^\pm decay	branching fraction
$B^\pm \rightarrow \rho^0 l\nu$	$1.30 \cdot 10^{-4}$
$B^\pm \rightarrow \omega l\nu$	$1.30 \cdot 10^{-4}$
$B^\pm \rightarrow \pi^0 l\nu$	$0.90 \cdot 10^{-4}$
$B^\pm \rightarrow \eta l\nu$	$0.18 \cdot 10^{-4}$
$B^\pm \rightarrow \eta' l\nu$	$0.30 \cdot 10^{-4}$
$B^\pm \rightarrow a_0^0 l\nu$	$0.18 \cdot 10^{-4}$
$B^\pm \rightarrow a_1^0 l\nu$	$2.06 \cdot 10^{-4}$
$B^\pm \rightarrow b_1^0 l\nu$	$1.20 \cdot 10^{-4}$
$B^\pm \rightarrow f_0^0 (f_0^{0'}) l\nu$	$0.09 \cdot 10^{-4}$
$B^\pm \rightarrow f_1^0 (f_1^{0'}) l\nu$	$1.02 \cdot 10^{-4}$
$B^\pm \rightarrow f_2^0 (f_2^{0'}) l\nu$	$0.90 \cdot 10^{-4}$
$B^\pm \rightarrow h_1^0 (h_1^{0'}) l\nu$	$0.60 \cdot 10^{-4}$
$B^\pm \rightarrow X_u^0 l\nu$	$4.62 \cdot 10^{-4}$
Total	$17.26 \cdot 10^{-4}$

Table 4.4: Branching fractions of the generated $B^\pm \rightarrow H_u l\nu$ decay modes. The leptons are electrons or muons.

meson	decay mode	branching fraction
a_0^0	$\eta\pi^0$	0.900
	K^+K^-	0.100
a_0^\pm	$\eta\pi^\pm$	0.900
	\bar{K}^0K^+	0.100
a_1^\pm	$\rho^0\pi^\pm$	0.492
	$\rho^\pm\pi^0$	0.508
a_1^0	$\rho^+\pi^-$	0.500
	$\rho^-\pi^+$	0.500
a_2^\pm	$\rho^0\pi^\pm$	0.350
	$\rho^\pm\pi^0$	0.350
	$\eta\pi^\pm$	0.144
a_2^0	$\omega\pi^\pm\pi^0$	0.105
	$\rho^+\pi^-$	0.350
	$\rho^-\pi^+$	0.350
	$\eta\pi^0$	0.144
	$\omega\pi^+\pi^-$	0.105

Table 4.5: The dominant decay modes of the a mesons as they have been used in the Monte Carlo simulation. Only the modes with a branching fraction $> 10\%$ are listed.

meson	decay mode	branching fraction
f_0	$\pi^+\pi^-$	0.520
	$\pi^0\pi^0$	0.260
	K^+K^-	0.110
f'_0	$\pi^+\pi^-$	0.520
	$\pi^0\pi^0$	0.260
f_1	$\rho^0\pi^+\pi^-$	0.150
	$a_0^0\pi^0$	0.140
	$a_0^+\pi^-$	0.140
f'_1	$a_0^-\pi^+$	0.140
	$K^+K^-\pi^0$	0.250
	$K^0\bar{K}^0\pi^0$	0.250
	$\bar{K}^0K^+\pi^-$	0.250
f_2	$K^0K^-\pi^+$	0.250
	$\pi^+\pi^-$	0.565
f'_2	$\pi^0\pi^0$	0.282
	K^+K^-	0.444
	$K_S^0K_S^0$	0.222
	$K_L^0K_L^0$	0.222
	$\eta\eta$	0.103

Table 4.6: The dominant decay modes of the f mesons as they have been used in the Monte Carlo simulation. Only the modes with a branching fraction $> 10\%$ are listed.

meson	decay mode	branching fraction
b_1^0	$\omega\pi^0$	0.998
b_1^+	$\omega\pi^+$	0.998
h_1	$\rho^+\pi^-$	0.333
	$\rho^-\pi^+$	0.333
	$\rho^0\pi^0$	0.333
h'_1	$K^{*+}K^-$	0.250
	$K^{*-}K^+$	0.250
	$\bar{K}^{*-}K^0$	0.250
	$K^{*-}\bar{K}^0$	0.250
η	$\gamma\gamma$	0.393
	$\pi^0\pi^0\pi^0$	0.321
	$\pi^-\pi^+\pi^0$	0.232
η'	$\pi^+\pi^-\eta$	0.437
	$\pi^0\pi^0\eta$	0.208
	$\rho^0\gamma$	0.302

Table 4.7: The dominant decay modes of the b , h and η mesons as they have been used in the Monte Carlo simulation. Only the modes with a branching fraction $> 10\%$ are listed.

experiment	branching fraction $b \rightarrow ul\nu$ ($\times 10^3$)	reference
LEP	1.74 ± 0.37 (stat+syst) ± 0.38 ($b \rightarrow c$) ± 0.2 ($b \rightarrow u$)	[30]
OPAL	1.63 ± 0.57 (stat+syst) $^{+0.44}_{-0.52}$ ($b \rightarrow c$) ± 0.25 ($b \rightarrow u$)	[31]
CLEO	1.77 ± 0.29 (stat) ± 0.38 (syst)	[32]
BABAR	2.05 ± 0.27 (stat) ± 0.46 (syst)	[33]

Table 4.8: Measured $b \rightarrow ul\nu$ branching fraction in different experiments. The combined LEP result does not include the OPAL result. The preliminary BABAR result relies on input from the CLEO measurement [32] to extract the total branching fraction from the measured partial branching fraction.

Monte Carlo is not used for background subtraction in this analysis, but only for a neural net training (see section 4.3.6), a cut optimization (see section 4.3.7) and a toy Monte Carlo study (see section 4.4.4).

4.2.1 Corrections to the Monte Carlo Simulation

The Monte Carlo simulation has been corrected on analysis level to match the data as precisely as possible. The following corrections have been applied:

- Each track of the $B \rightarrow (\rho, \omega, \pi)\ell\nu$ final state has been weighted by an efficiency correction factor. The correction is a function of the angles θ , ϕ , the momentum of the track, and the event multiplicity. The correction factors were derived in a separate tracking efficiency study [34, 35, 36].
- The electron and kaon selection efficiencies and the misidentification probabilities have been obtained from data control samples in a separate study [37]. Elec-

$B \rightarrow D\ell\nu$	2.69 %
$B \rightarrow D^*\ell\nu$	4.68 %
$B \rightarrow D^{(*)}(\pi)\ell\nu$	3.49 %
total	10.86 %

Table 4.9: Branching fractions used for the generation of the semileptonic $b \rightarrow c$ background modes.

trons and kaons in the Monte Carlo simulations are selected according to these efficiencies and misidentification probabilities. Technically this is implemented by generating a uniformly distributed random number for each track. A track is selected or discarded depending on the generated random number and the value of the efficiency as determined from the control samples.

- A small fraction of π^0 mesons is randomly discarded to better match the π^0 reconstruction efficiency found in the data. The exact fraction has been obtained in a separate study [38].
- The energy measurement of all photons has been smeared by 1.5% to better match the energy resolution found in the data [39].

The histograms in this chapter show a comparison between on-resonance data, with off-resonance data and fake electrons subtracted (see section 4.3.2), and generic $B\bar{B}$ Monte Carlo simulation. The histograms have been made before fitting the data. Nevertheless, the agreement of data and Monte Carlo simulation is good. For these comparisons only leptons with center-of-mass energy greater than 2.0 GeV are selected and all cuts, except the cut being studied, are applied.

4.3 Event Selection

All quantities that will be used are boosted in the rest frame of the $\Upsilon(4S)$ meson unless stated otherwise.

Two lepton-energy regions will be considered in this analysis:

- **LOLEP:** $2.0 \text{ GeV} \leq E_{\text{lept}} < 2.3 \text{ GeV}$
- **HILEP:** $2.3 \text{ GeV} \leq E_{\text{lept}} < 2.7 \text{ GeV}$

The HILEP region is most sensitive to the signal because semileptonic $b \rightarrow c\ell\nu$ decays are almost completely suppressed in this region for kinematical reasons. In the LOLEP region, $b \rightarrow c$ decays dominate. Below 2 GeV, a study has shown that the exact modeling of the poorly known $b \rightarrow u$ backgrounds has large influence on the fit result. Therefore this region is not included in this analysis.

4.3.1 Multihadron Selection

Multihadron events are selected according to the following requirements:

- The Fox Wolfram moments [40] are defined as

$$H_l = \sum_{i,j} \frac{|p_i||p_j|}{E_{vis}^2} P_l(\cos \theta_{ij}) , \quad (4.1)$$

where $p_{i,j}$ are the particle momenta, θ_{ij} is the opening angle between particles i and j , P_l are Legendre polynomials, and E_{vis} is the total visible energy of the event. For the 2nd normalized Fox Wolfram Moment $\mathcal{R}_2 = H_2/H_0$ calculated with *good tracks*¹ and *good bumps*² it is required that $\mathcal{R}_2 < 0.4$. The \mathcal{R}_2 distributions for signal and background are shown in Fig. 4.1(a). Good agreement between data and Monte Carlo simulation is observed, see Fig. 4.1(b).

- Either $NTracks \geq 5$ or ($NTracks \geq 4$ and $NBumps \geq 5$), where $NTracks$ is the number of good tracks and $NBumps$ is the number of good bumps.

After all cuts one obtains a signal efficiency between 80% and 90%, depending on the decay channel and electron energy region.

4.3.2 Electron Selection

Identification Algorithm

A likelihood based electron selector [29] is used to identify electrons. Good tracks within the good DCH and EMC acceptance $-0.72 < \cos \theta_{e,lab} < 0.92$ are considered as electron candidates. The algorithm uses information from all subdetectors and combines them in a likelihood function. With the very low fake rate of the likelihood selector (approx. 0.1% for $E_{e,lab} > 1.5$ GeV) the fake backgrounds are almost negligible.

J/ψ Veto

Electrons which are likely to come from a $J/\psi \rightarrow e^+e^-$ decay are rejected. A J/ψ meson is reconstructed from two oppositely charged electron tracks which have an invariant mass $3.00 < M_{l+l^-} < 3.14$ GeV. According to Monte Carlo simulation the efficiency for rejecting electrons above 2 GeV from J/ψ decays after all other cuts is 73%.

Photon Conversions

Electrons which are likely to have their origin in a photon conversion are rejected, too. The conversion finder algorithm requires the following

¹see section 4.3.3 for the definition of a *good track*

²*BABAR* software distinguishes between *bumps* and *clusters*. A cluster is a region of adjacent crystals with deposited energy. A cluster will be splitted in two or more bumps if the shape of the energy deposition indicates that more than the cluster contains energy from more than one particle. See 4.3.3 for the definition of a *good bump*.

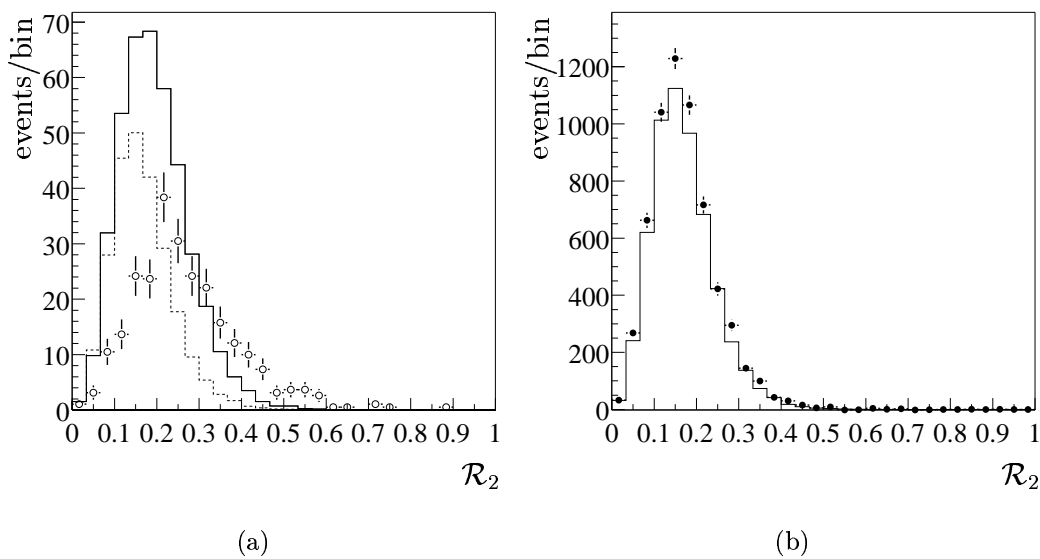


Figure 4.1: The \mathcal{R}_2 distribution: **(a)** for the signal $B^+ \rightarrow \rho^0 e^+ \nu$ (solid line), the $b \rightarrow cl\nu$ background events (dashed line), and off-resonance data (open points). The normalization is arbitrary. **(b)** Comparison between on-resonance data (points), with off-resonance data and fake electrons subtracted, and generic $B\bar{B}$ Monte Carlo simulation as described in section 4.2.1 (solid line).

- invariant mass of the electron pair $M_{e^+e^-} < 0.03 \text{ GeV}/c^2$
- closest distance of the trajectories in the xy -plane $\text{doca}_{xy} < 0.5 \text{ cm}$
- closest distance of γ trajectory to the detector origin $d < 3.0 \text{ cm}$
- distance of the points of closest approach along the direction of the beam axis $\Delta z < 1.0 \text{ cm}$

According to Monte Carlo simulation the efficiency for rejection of electrons above 2.0 GeV from photon conversions after all other cuts is 37%.

Fake Electrons

Some hadrons are not rejected by the electron identification algorithm. In the following these are called *fake electrons*. The probability that a hadron fakes an electron is rather small ($< 0.1\%$). For muons it would be significantly larger. Therefore muons are not used in this analysis. The shapes of the *fake electron* distributions are determined from data: The analysis is repeated with tracks that do *not* satisfy the electron identification requirements. The distributions are then scaled with a factor proportional to the fake rates. This has to be done for the on-resonance and off-resonance data. The calculation of the weight is elaborated below.

The measured sample of tracks not identified as electrons consists of

$$N_{\text{non-e}}^{\text{meas}} = \epsilon \cdot N_{\text{non-e}}^{\text{tot}} + n_e \quad (4.2)$$

with

$$\epsilon = f_\pi(1 - \eta_\pi) + f_K(1 - \eta_K) + f_p(1 - \eta_p) + f_\mu(1 - \eta_\mu) , \quad (4.3)$$

where

- $N_{\text{non-e}}^{\text{tot}}$ is the true total number of tracks that are not electrons.
- f_i , where $i = \pi, K, p, \mu$, are the fractions of particles with respect to $N_{\text{non-e}}^{\text{tot}}$. Monte Carlo simulation is used to determine these fractions.
- $\eta_i = \eta_i(p, \theta, \phi)$, where $i = \pi, K, p, \mu$, are the misidentification probabilities that a particle of type i is misidentified as an electron. These probabilities depend on the selector used and some kinematic variables of the tracks. The fake rates have been determined from data control samples. The approximation $\eta_\mu \approx 0$ is made.
- n_e is the number of electrons that have not been identified by the selector.

Therefore the measured sample of tracks not identified as electrons with the likelihood selector is

$$N_{\text{non-e(Lik)}}^{\text{meas}} = \epsilon_{\text{Lik}} \cdot N_{\text{non-e}}^{\text{tot}} + n_{e_{\text{Lik}}} , \quad (4.4)$$

where ϵ_{Lik} is given by Eq. 4.3 using the mis-identification probabilities for the likelihood based selector. To avoid an electron contamination of the measured *fake electron* distributions ($N_{\text{non-e}}^{\text{meas}}$), a selector with looser cuts is used: The *loose electron selector*. In that case, the efficiency of selecting an electron is approximately 100% and therefore $n_e \approx 0$ in Eq. 4.2. Using the loose selector, the measured number of tracks not identified as electrons is

$$N_{\text{non-e(Loose)}}^{\text{meas}} = \epsilon_{\text{Loose}} \cdot N_{\text{non-e}}^{\text{tot}} , \quad (4.5)$$

where ϵ_{Loose} is given by Eq. 4.3 using the mis-identification probabilities for the loose selector.

The number of fake electrons selected by the likelihood based electron selector is then

$$\begin{aligned} N_{\text{fake}} &= N_{\text{non-e}}^{\text{tot}} - (N_{\text{non-e(Lik)}}^{\text{meas}} - n_{e_{\text{Lik}}}) \\ &= N_{\text{non-e}}^{\text{tot}} - (\epsilon_{\text{Lik}} \cdot N_{\text{non-e}}^{\text{tot}} + n_{e_{\text{Lik}}} - n_{e_{\text{Lik}}}) \\ &= (1 - \epsilon_{\text{Lik}}) N_{\text{non-e}}^{\text{tot}} \\ &= \frac{1 - \epsilon_{\text{Lik}}}{\epsilon_{\text{Loose}}} N_{\text{non-e(Loose)}}^{\text{meas}} \end{aligned} \quad (4.6)$$

$$= w \cdot N_{\text{non-e(Loose)}}^{\text{meas}} , \quad (4.7)$$

where Eq. 4.4 and 4.5 have been used. N_{fake} will be determined for the on-resonance data ($N_{\text{fake,on}}$) and off-resonance data ($N_{\text{fake,off}}$) in bins of i . i runs over $M_{\pi\pi(\pi)}$, ΔE , the two lepton-energy regions (HILEP, LOLEP), and the five signal modes ($B^+ \rightarrow \rho^0 e^+ \nu$, $B^0 \rightarrow \rho^- e^+ \nu$, $B^+ \rightarrow \pi^0 e^+ \nu$, $B^0 \rightarrow \pi^- e^+ \nu$, and $B^+ \rightarrow \omega e^+ \nu$). The number of fake electrons for the $B\bar{B}$ contribution is

$$N_{\text{fake},B\bar{B}}^i = N_{\text{fake,on}}^i - k \cdot N_{\text{fake,off}}^i , \quad (4.8)$$

where k is the ratio of on-resonance to off-resonance luminosities. The fake electron distributions have been determined using 2.9 fb^{-1} on-resonance and 2.0 fb^{-1} off-resonance

	on-resonance	off-resonance
$\langle f_\pi \rangle$	$(68.0 \pm 2.5)\%$	$(62.3 \pm 0.8)\%$
$\langle f_K \rangle$	$(12.6 \pm 1.1)\%$	$(28.4 \pm 0.5)\%$
$\langle f_p \rangle$	0	$(0.6 \pm 0.08)\%$
$\langle f_\mu \rangle$	$(19.4 \pm 1.3)\%$	$(8.4 \pm 0.3)\%$

Table 4.10: Fractions of particles with respect to the total number of tracks that are not electrons.

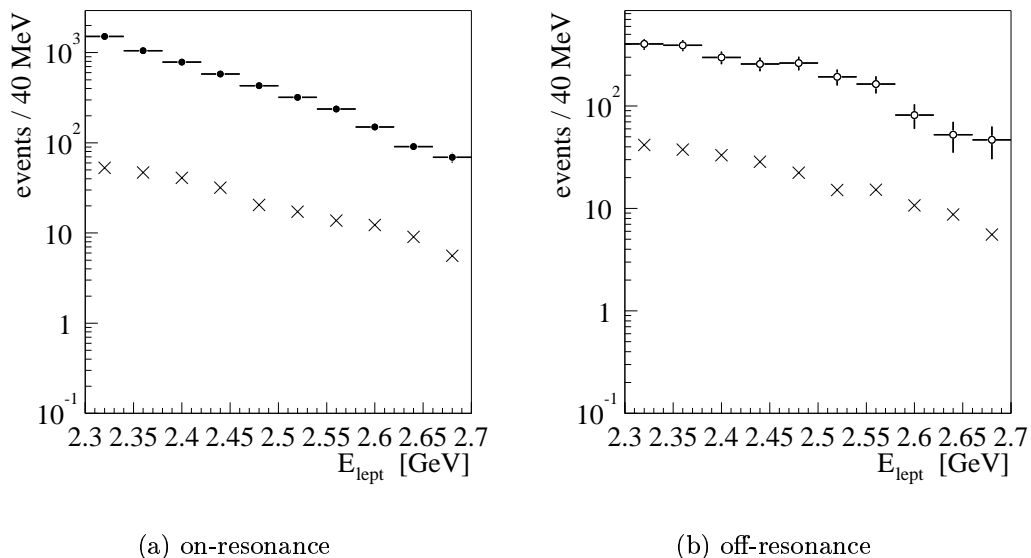


Figure 4.2: The fake-lepton E_{lept} -distribution for the sum of the signal vector modes is shown with crosses, after all cuts applied: **(a)** on-resonance data **(b)** off-resonance data. The solid (open) points show the on-resonance (off-resonance) data for comparison. Note the logarithmic scale.

data selected randomly from all data runs (see Table 4.1). A normalization to the total on-resonance and off-resonance luminosities has been performed.

Typical average values of w are $0.8 \cdot 10^{-3}$ for on-resonance and $1 \cdot 10^{-3}$ for off-resonance data. There is no strong momentum dependence. The mean fractions of pions, kaons, protons, and muons, which are used for the on-resonance and off-resonance data fake electron determination are listed in Table 4.10. These have been obtained from $B\bar{B}$ and continuum Monte Carlo simulation.

Fig. 4.2 shows the amount of misidentified electrons in on- and off-resonance data as determined by the method described in this section. Table 4.11 shows the number of fake leptons in the HILEP region for the three modes $B^+ \rightarrow \rho^0 \ell^+ \nu$, $B^0 \rightarrow \rho^- \ell^+ \nu$, and $B^+ \rightarrow \omega \ell^+ \nu$. All cuts of the selection have been applied.

	on-resonance	off-resonance	$\Upsilon(4S)$
fake electrons	246 ± 2 (4.7%)	37 ± 2 (10.1%)	30 ± 13 (0.98%)
data yield	5221	368	3074

Table 4.11: Number of fake electrons for the sum of the vector signal modes in the HILEP region. All cuts have been applied. The errors are statistical only. The selected on-resonance and off-resonance data yield is given for comparison. The numbers in parantheses are the fractions of fake leptons in the on-resonance, off-resonance, and $\Upsilon(4S)$ data yields.

The systematic error on the weights w_i is determined by the finite size of the data control samples which have been used to determine the electron identification efficiencies and by a possible bias due to the specific data selection of the control samples. The error is estimated to be approximately 20% [42] and is therefore negligible compared to the statistical error on the $\Upsilon(4S)$ fake-lepton contribution quoted in Table 4.11.

4.3.3 Hadron Selection

For the hadron reconstruction, good tracks with

- distance of closest approach to the primary vertex in the xy -plane $\text{doca}_{xy} < 1.0$ cm
- distance of closest approach to the primary vertex in z -direction $\Delta z < 3.0$ cm
- number of DCH hits $N_{DCHhits} \geq 12$
- azimuthal angle $0.41 < \theta_{lab} < 2.54$
- *not* identified as kaon

are used. In the $B \rightarrow \pi \ell \nu$ channels the pion must have $p_\pi > 200$ MeV/ c . The cuts for the other channels are described below.

π^0 Reconstruction

π^0 mesons are assembled from two photons fitted to the primary vertex with an invariant mass $120 < M_{\gamma\gamma} < 145$ MeV/ c^2 corresponding to $\pm 2\sigma$ from the nominal mass on average, see Fig. 4.3. $p_{\pi^0} > 200$ MeV/ c is required. For photons, good bumps with

- calibrated lab energy $E_{\gamma,lab} > 30$ MeV
- lateral moment $\text{LAT} < 0.8$ [29].

are required.

ρ Reconstruction

To reconstruct the neutral ρ meson two oppositely charged tracks, or a track and a π^0 in case of the charged ρ are combined. To suppress combinatorial backgrounds it is required that the pion with the highest momentum must have $p_\pi^{\max} > 400$ MeV/ c and the other pion $p_\pi > 200$ MeV/ c . There is no cut on the ρ mass.

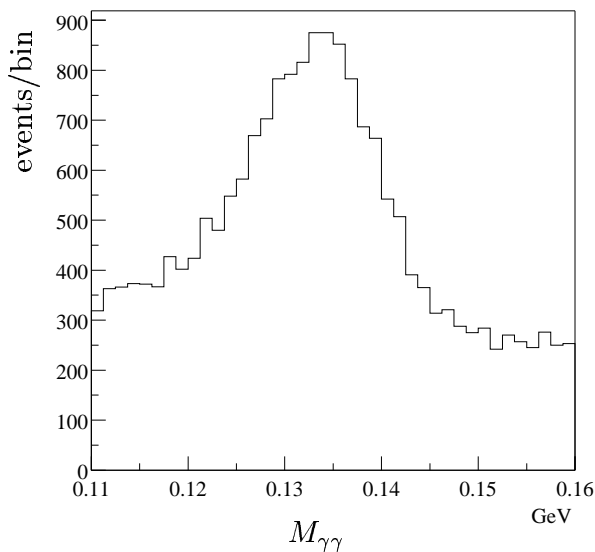


Figure 4.3: The two- γ invariant-mass spectrum for π^0 combinations with $E_{\gamma\gamma} > 325$ MeV.

ω Reconstruction

For the ω meson two oppositely charged tracks are combined with a π^0 . The ω invariant mass must lie within ± 80 MeV/ c^2 of the nominal mass $M_\omega = 782.57$ MeV [22]. To suppress combinatorial backgrounds for all three pions it is required that $p_\pi > 100$ MeV/ c .

4.3.4 Missing Momentum

The missing momentum is defined as

$$\vec{p}_{\text{miss}} = - \sum_{\text{tracks}} \vec{p}_i - \sum_{\text{clusters}} \vec{p}_i, \quad (4.9)$$

where the sums run over all reconstructed and accepted good tracks and good photons in the event. The missing momentum can either be attributed to a neutrino or to missing tracks and photons owing to detector geometry or reconstruction efficiencies. Geometry is well modeled in Monte Carlo simulation, but the influence of efficiencies has to be studied carefully.

Fig. 4.4 shows the distributions of $|\vec{p}_{\text{miss}}| - |\vec{p}_\nu|$ for (a) the nominal tracking efficiency (as given by a separate tracking efficiency study [34, 35, 36]), (b) with a 1% increased tracking efficiency, (c) a 1% decreased tracking efficiency, and (d) a 2.5% increased photon efficiency. The algorithm used to simulate different tracking efficiencies is described in section 5.4.1. These distributions are fitted with two Gaussian functions: Parameters p_0 (arbitrary normalization), p_1 (mean) and p_2 (sigma) are the parameters of the narrow core Gaussian and p_3 , p_4 and p_5 the parameters of the wide Gaussian that describes the tail to the left. This tail is caused by lost tracks and clusters. The smaller tail on the right is due to doubly counted energy and other resolution effects. As can be seen from the figures, the impact of the tracking and photon efficiencies on the width of

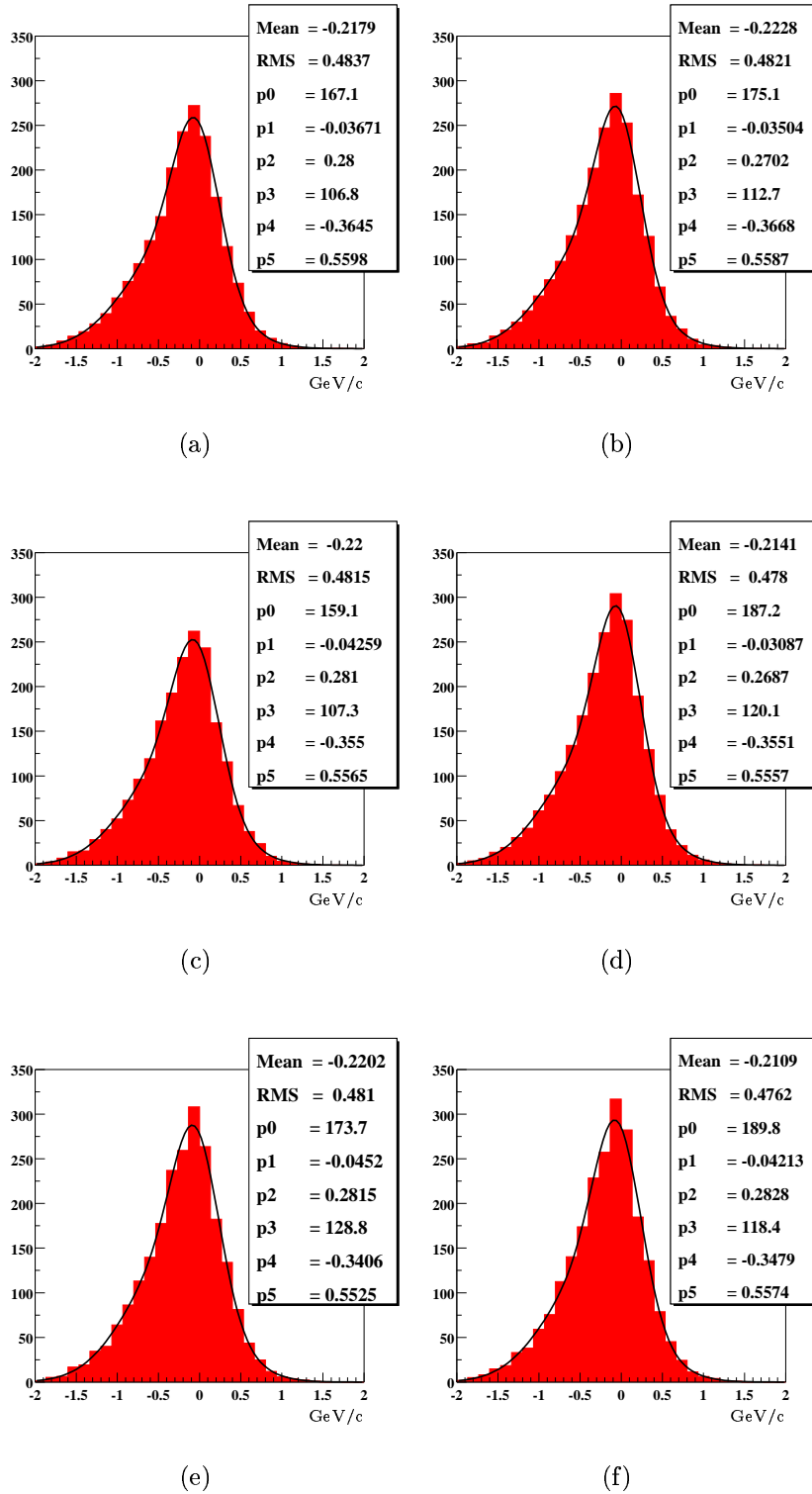


Figure 4.4: Resolution $|\vec{p}_{\text{miss, reco}}| - |\vec{p}_{\text{miss, truth}}|$ of the missing momentum for (a) the nominal tracking efficiency, (b) with a 1% increased tracking efficiency, (c) a 1% decreased tracking efficiency, (d) a 2.5% increased photon efficiency, (e) with twice the fraction of events with at least one K_L meson, (f) with twice the fraction of events with at least one neutron.

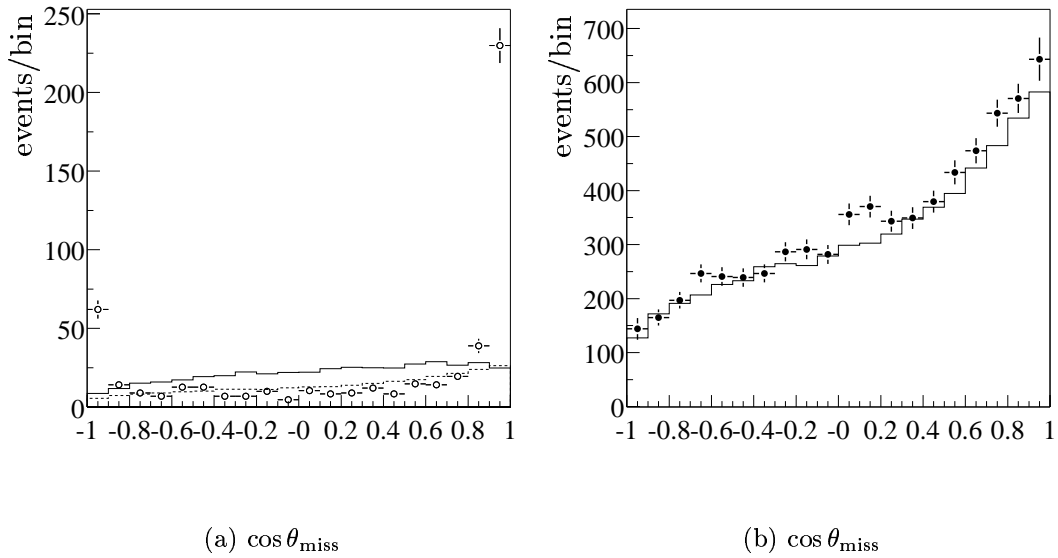


Figure 4.5: The $\cos \theta_{\text{miss}}$ distribution: **(a)** for the signal $B^+ \rightarrow \rho^0 e^+ \nu$ (solid line), the $b \rightarrow c \ell \nu$ background events (dashed line) and off-resonance data (open points). The normalization is arbitrary. **(b)** Comparison between on-resonance data (points), with off-resonance data and fakes subtracted, and generic $B\bar{B}$ Monte Carlo simulation as described in section 4.2.1 (solid line).

the $|\vec{p}_{\text{miss}}| - |\vec{p}_\nu|$ distribution is rather small. The width is dominated by the geometric acceptance of the detector and other effects (undetected particles like K_L mesons or further neutrinos). Thus, the tracking efficiency corrections, see section 4.2.1 and 5.4.1, are only applied to the electron and the pions from ρ and ω decays and not to the other tracks in the event.

According to Monte Carlo simulation, 22% (36%) of all signal events contain at least one K_L meson (neutron). Fig. 4.4 (e) shows the change of resolution when the fraction of events which contain at least one K_L meson is increased by a factor of 2. Fig. 4.4 (f) shows the resolution after increasing the fraction of events with a neutron by a factor of 2. In both cases one can see a very small increase in width. The fit result for the branching fraction $B \rightarrow \rho \ell \nu$ is not sensitive to the precise number of K_L mesons or neutrons present.

It is required that

$$|\cos \theta_{\text{miss}}| < 0.9, \quad (4.10)$$

where θ_{miss} is the angle between \vec{p}_{miss} and the beam axis. This rejects events with high momentum particles close to the beam axis and especially continuum events (see Fig. 4.5). Continuum is suppressed by 40%, the signal only by 10%. The influence of this cut on the $|\vec{p}_{\text{miss}}| - |\vec{p}_\nu|$ resolution is unfortunately rather small.

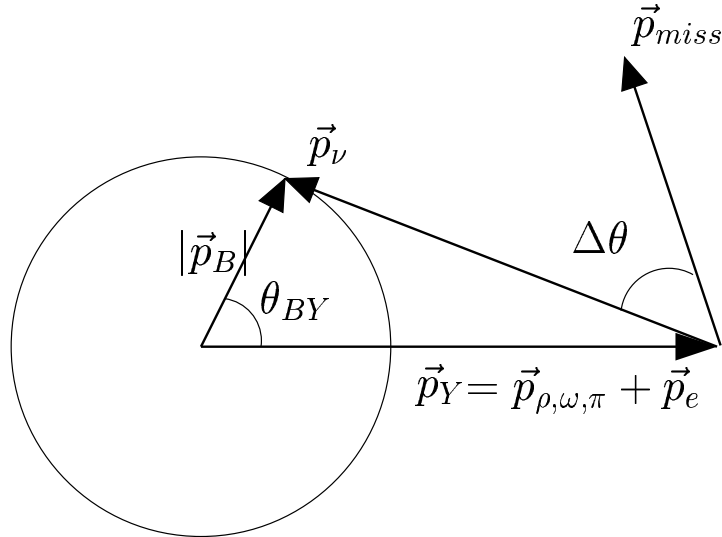


Figure 4.6: Angles θ_{BY} and $\Delta\theta$ defined in the $\mathcal{T}(4S)$ frame.

4.3.5 Consistency Cuts

The angle θ_{BY} is defined in Fig. 4.6. The four-momentum $p_Y = p(\rho, \omega, \pi) + p_l$ has to be consistent with a B meson decay. For the four-momentum of the neutrino in a $B \rightarrow (\rho, \omega, \pi)l\nu$ event, one must have

$$p_\nu^2 = 0 = (p_B - p_Y)^2 = M_B^2 + M_Y^2 - 2(E_B E_Y - |\vec{p}_B| |\vec{p}_Y| \cos \theta_{BY}). \quad (4.11)$$

The four vector of the B meson, p_B , has an unknown direction. Nevertheless, Eq. 4.11 can be resolved for $\cos \theta_{BY}$ because the energy of the B meson is known:

$$\cos \theta_{BY} = \frac{2E_B E_Y - M_B^2 - M_Y^2}{2|\vec{p}_B| |\vec{p}_Y|}. \quad (4.12)$$

For each reconstructed decay one must have $|\cos \theta_{BY}| < 1$. The $\cos \theta_{BY}$ distribution is shown in Fig. 4.7. Background will tend to have non-physical values of $\cos \theta_{BY}$. Background coming from the continuum will also be rejected. Extensions of $|\cos \theta_{BY}| > 1$ are due to detector resolution. Therefore it is required that

$$|\cos \theta_{BY}| < 1.1. \quad (4.13)$$

The signal efficiency of this cut is almost 100%. It rejects more than 60% of the $b \rightarrow cl\nu$ and 80% of the continuum background (see Tables 4.12 and 4.13). As can be seen in Fig. 4.7, the Monte Carlo simulation reproduces the data well.

The direction of the missing momentum \vec{p}_{miss} can be compared with that of the neutrino momentum $\vec{p}_\nu = \vec{p}_B - \vec{p}_Y$ as inferred from the B meson decay. The latter is known up to an azimuthal ambiguity about the \vec{p}_B direction because the modulus, but not the direction of the B meson momentum is known. The angle $\Delta\theta$ between \vec{p}_{miss} and \vec{p}_ν can be written as

$$\cos \Delta\theta = \frac{\vec{p}_\nu \cdot \vec{p}_{\text{miss}}}{|\vec{p}_\nu| |\vec{p}_{\text{miss}}|} = \frac{\vec{p}_B \vec{p}_{\text{miss}} - \vec{p}_Y \vec{p}_{\text{miss}}}{|\vec{p}_\nu| |\vec{p}_{\text{miss}}|}, \quad (4.14)$$

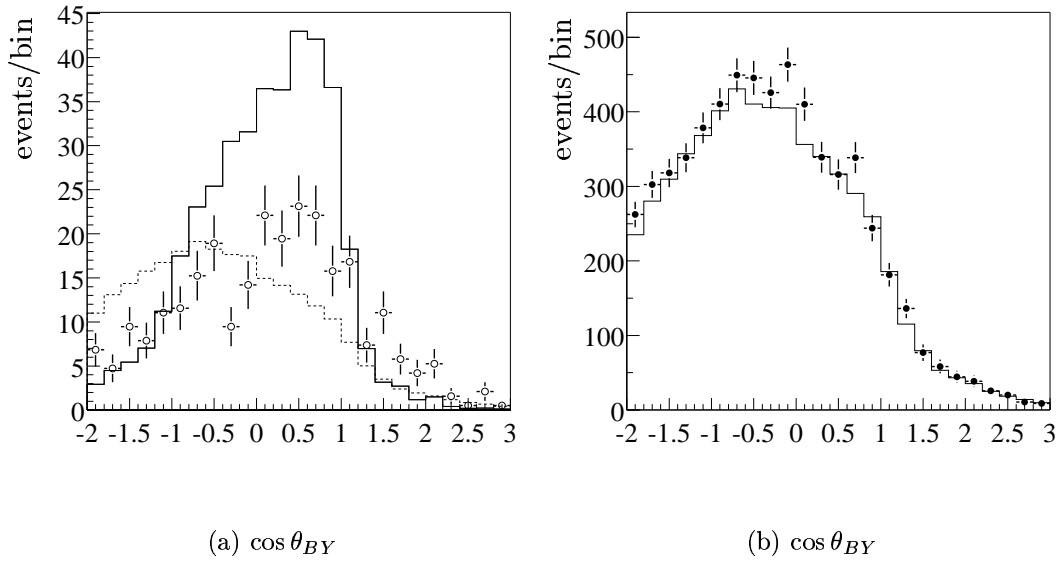


Figure 4.7: The $\cos \theta_{BY}$ distribution: **(a)** for the signal $B^+ \rightarrow \rho^0 e^+ \nu$ (solid line), the $b \rightarrow cl\nu$ background events (dashed line) and off-resonance data (open points). The normalization is arbitrary. **(b)** Comparison between on-resonance data (points), with off-resonance data and fakes subtracted, and generic $B\bar{B}$ Monte Carlo simulation as described in section 4.2.1 (solid line).

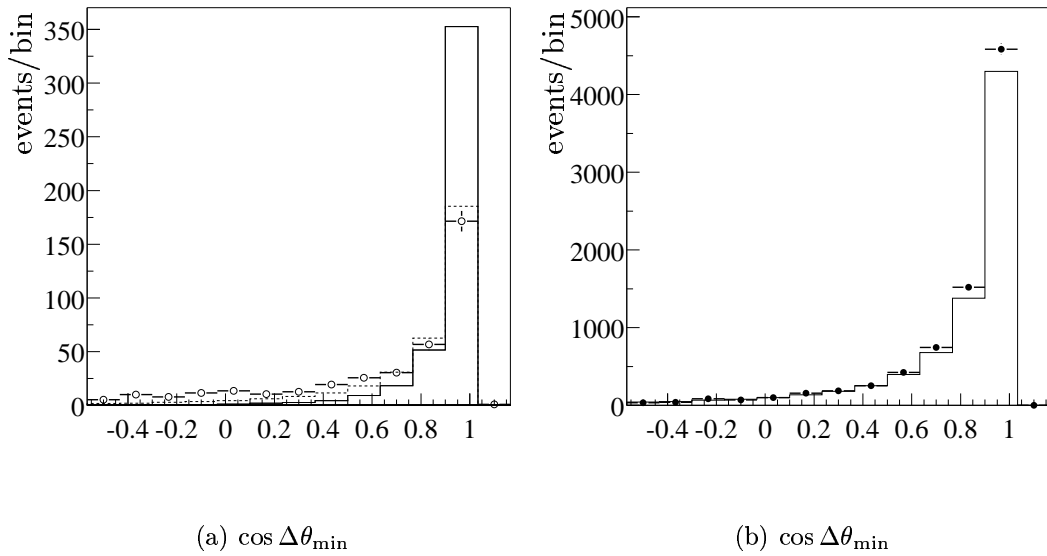


Figure 4.8: The $\cos \Delta \theta_{\min}$ distribution: **(a)** for the signal $B^+ \rightarrow \rho^0 e^+ \nu$ (solid line), the $b \rightarrow cl\nu$ background events (dashed line) and off-resonance data (open points). The normalization is arbitrary. **(b)** Comparison between on-resonance data (points), with off-resonance data and fakes subtracted, and generic $B\bar{B}$ Monte Carlo simulation as described in section 4.2.1 (solid line).

where

$$\begin{aligned}\vec{p}_B \vec{p}_{\text{miss}} &= |\vec{p}_B| |\vec{p}_{\text{miss}}| \cos \theta_{B,\text{miss}} , \text{ and} \\ \vec{p}_Y \vec{p}_{\text{miss}} &= |\vec{p}_Y| |\vec{p}_{\text{miss}}| \cos \theta_{Y,\text{miss}} .\end{aligned}\tag{4.15}$$

The smallest possible angle, denoted by $\Delta\theta_{\text{min}}$, is obtained when the momenta of \vec{p}_Y , \vec{p}_ν , and \vec{p}_{miss} are aligned in the same plane. In this case

$$\begin{aligned}\cos \theta_{B,\text{miss}} &= \cos(\theta_{BY} - \theta_{Y,\text{miss}}) \\ &= \cos \theta_{BY} \cos \theta_{Y,\text{miss}} + \sin \theta_{BY} \sin \theta_{Y,\text{miss}} .\end{aligned}\tag{4.16}$$

With these two relations and $|\vec{p}_\nu| = E_\nu = E_{\mathcal{Y}(4S)}/2 - E_Y$, $\cos \Delta\theta_{\text{min}}$ can be calculated from Eq. 4.14.

The $\cos \Delta\theta_{\text{min}}$ distribution is shown in Fig. 4.8. The cut optimization (see section 4.3.7) yields

$$0.8 < \cos \Delta\theta_{\text{min}} \leq 1.0 .\tag{4.17}$$

The efficiencies of this cut are given in Tables 4.12 and 4.13.

After all the cuts described above, there can still be many signal candidate combinations per event. This is because the width of the ρ is large and also because five different modes are reconstructed ($B^+ \rightarrow \rho^0 e^+ \nu$, $B^0 \rightarrow \rho^- e^+ \nu$, $B^+ \rightarrow \pi^0 e^+ \nu$, $B^0 \rightarrow \pi^- e^+ \nu$, and $B^+ \rightarrow \omega e^+ \nu$). To avoid statistical difficulties related to many number of combinations, only one candidate is chosen per event after all other cuts have been applied. The criterion is

$$|\vec{p}_{\text{had}} + \vec{p}_\ell + \vec{p}_{\text{miss}}| \text{ closest to } |\vec{p}_B| .\tag{4.18}$$

The $|\vec{p}_{\text{had}} + \vec{p}_\ell + \vec{p}_{\text{miss}}|$ distribution is shown in Fig. 4.9. The efficiency of this selection on the signal is near 85% .

4.3.6 Continuum Rejection

Continuum events $e^+e^- \rightarrow q\bar{q}$, where $q = u, d, s, c$, are an important background at high lepton energies. At the $\mathcal{Y}(4S)$ center-of-mass energy, the cross section for continuum events is three times larger than for $\mathcal{Y}(4S) \rightarrow B\bar{B}$ decays. Since the amount of available off-resonance data which can be used to characterize the continuum is quite low, one needs to find efficient cuts to reject continuum backgrounds.

One can use the fact that the B mesons are produced nearly at rest. Their decay products are distributed roughly uniformly in solid angle. In contrast, continuum events have a much more collimated (jet-like) event topology. Various quantities can be used to describe the overall distribution of tracks and photons in the event:

- The ratio of the second to zeroth Fox-Wolfram moments. This ratio of moments tends to be close to zero for spherical events and up to unity for jet-like events. This variable has already been discussed in section 4.3.1. It is required that $\mathcal{R}_2 < 0.4$.
- The output of a neural net (14:14:1) with the following 14 variables:

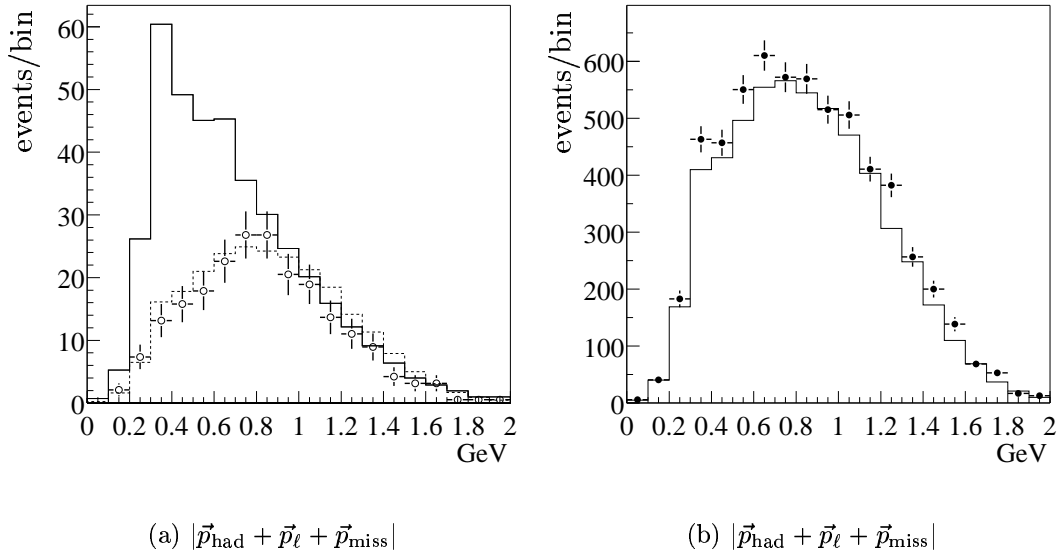


Figure 4.9: $|\vec{p}_{\text{had}} + \vec{p}_\ell + \vec{p}_{\text{miss}}|$ distribution: **(a)** for the signal $B^+ \rightarrow \rho^0 e^+ \nu$ (solid line), the $b \rightarrow c \ell \nu$ background events (dashed line) and off-resonance data (open points). The normalization is arbitrary. **(b)** Comparison between on-resonance data (points), with off-resonance data and fakes subtracted, and generic $B\bar{B}$ Monte Carlo simulation as described in section 4.2.1 (solid line).

- The track and CsI cluster energies in nine cones around the lepton-momentum axis.
- $|\cos \theta_{\text{thrust}}|$, where θ_{thrust} is the angle between the thrust axis of the Y system and the thrust axis of the rest of the event. The thrust axis is defined to be the direction which maximizes the sum of the longitudinal momenta of the particles.
- $|\cos \theta_{\text{thrust}, Y}|$, where $\theta_{\text{thrust}, Y}$ is the angle between the thrust of the Y system and the beam axis.
- $|\cos \theta_{\text{lept, rest}}|$, where $\theta_{\text{lept, rest}}$ is the angle between the direction of the lepton and the direction of the total momentum of all tracks except the Y system.
- Momentum of the track with the angle closest to the lepton ($P_{\text{closest track}}$).
- $S_{//} \equiv \sum \vec{p}_i \cdot \vec{n}_{\text{lept}} / \sum |\vec{p}_i|$, where \vec{n}_{lept} is the direction of the lepton and \vec{p}_i is the momentum of all tracks except the lepton.

These variables have been chosen among others using a step by step procedure: The most discriminating variable is chosen first; all other variables are then tested to see which one is the most discriminating together with the first variable; the third one is chosen in the same way, etc.; the discriminating efficiency is improved everytime a variable is added until a plateau is reached.

A comparison between data and Monte Carlo simulation for all input variables is shown in Figs. 4.10 and 4.11. The neural net output itself for the $B^+ \rightarrow \rho^0 \ell^+ \nu$ and $B^0 \rightarrow \rho^- \ell^+ \nu$ channels is shown in Fig. 4.13. In all cases rather good agreement is observed.

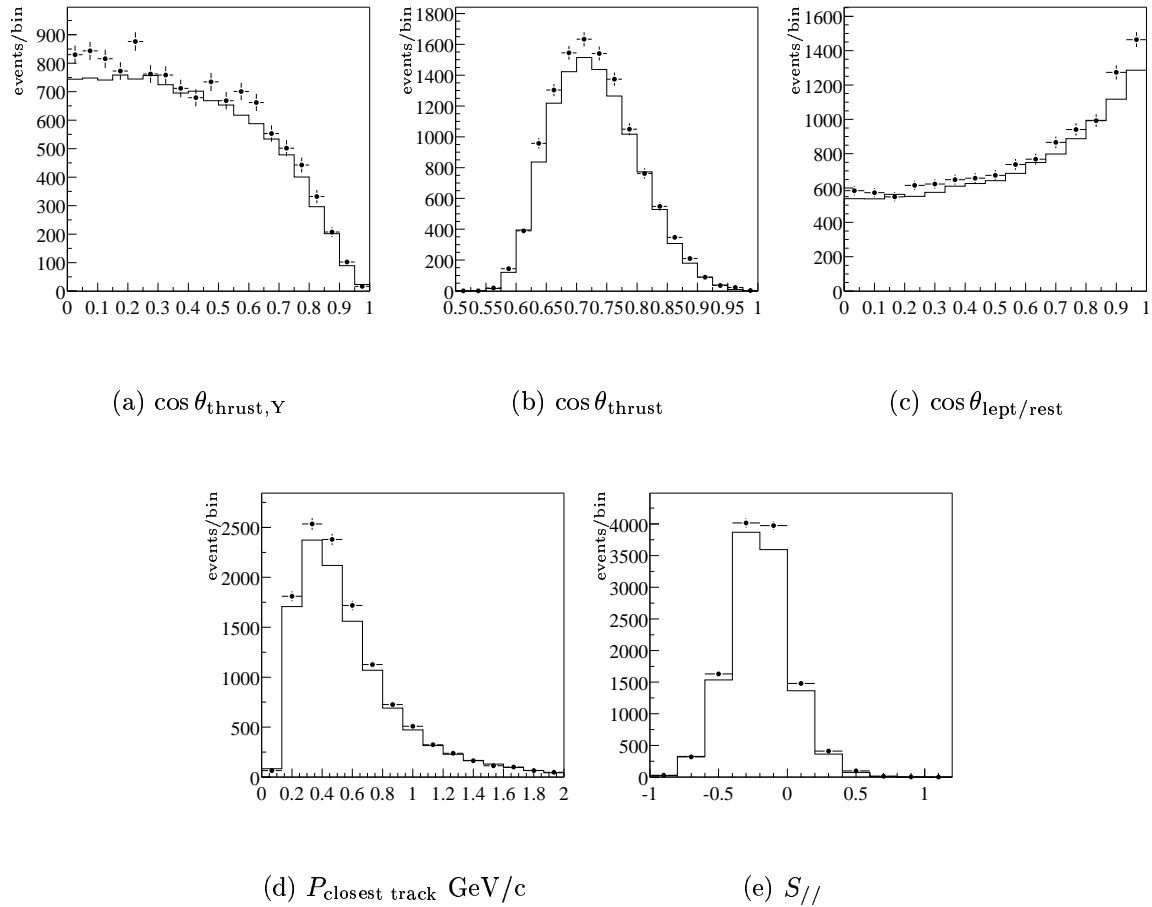


Figure 4.10: Comparison between on-resonance data (points), with off-resonance data and fakes subtracted, and generic $B\bar{B}$ Monte Carlo simulation (solid line) of some variables used as input to the neural net (see text). The data and Monte Carlo samples used for these comparisons are described in section 4.2.1.

The neural net has been trained using the true (according to Monte Carlo truth matching) signal combinations from the generic B meson decay sample including the hard-lepton sample. In this way a possible statistical bias will be avoided since the training sample is independent of the events in the signal Monte Carlo samples used in the fit. For the continuum a Monte Carlo simulation has been used to obtain a training sample. The same net training is used for all five signal channels. The output of the neural net is shown in Fig. 4.12. The cut on the net output has been optimized, see section 4.3.7:

$$\mathcal{O}_{\text{net}} > 0.6. \quad (4.19)$$

This cut suppresses approximately 90% of the remaining signal candidates from off-resonance data after all other cuts have been applied. The survival probability for Monte Carlo signal candidates is approximately 60%.

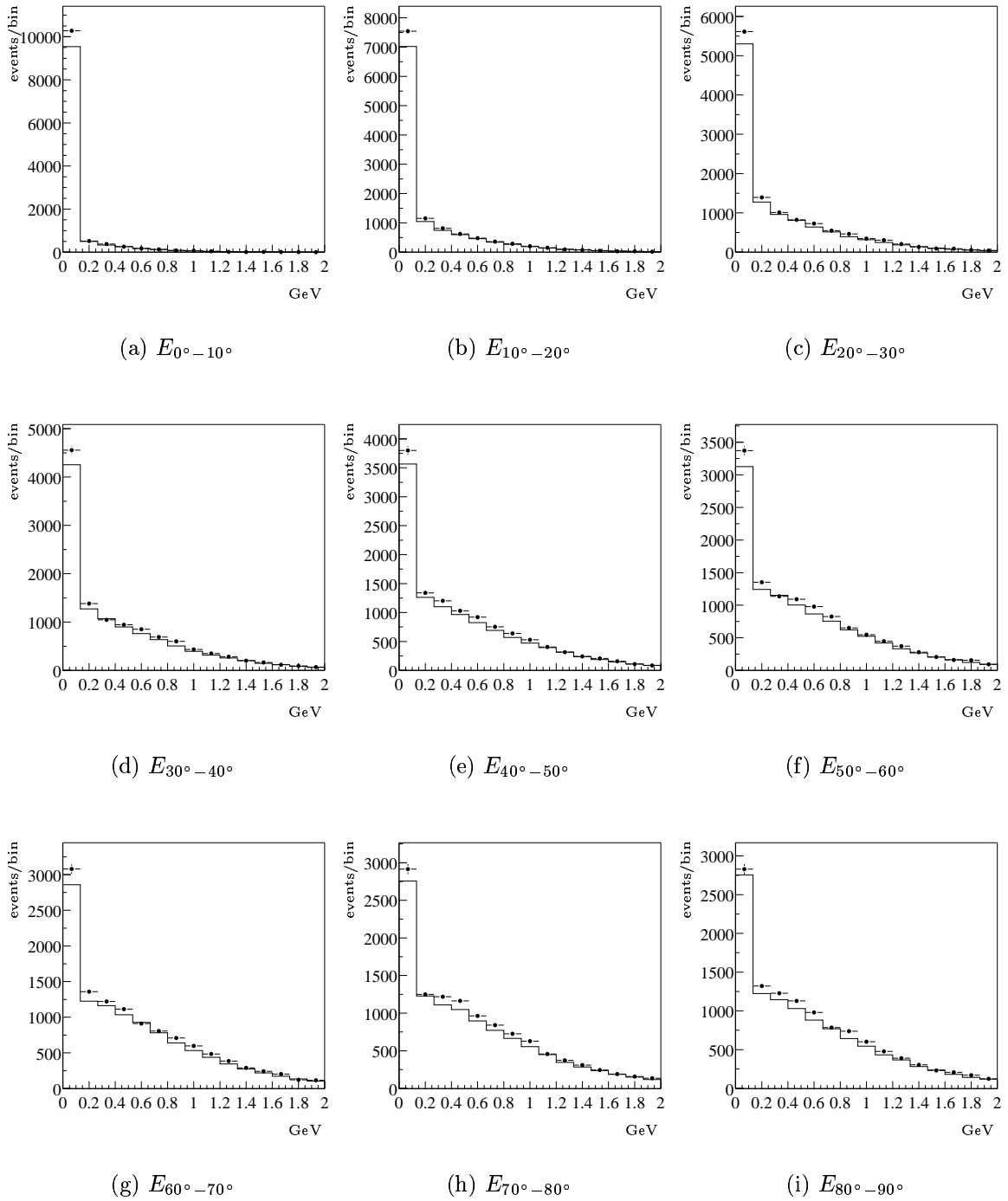


Figure 4.11: Distribution of $E_{\alpha_1-\alpha_2} \equiv \sum_i |\vec{p}_i| + \sum_j E_j$, where \vec{p}_i and E_j are the momentum of the track i and the energy of the cluster j for $\alpha_1 < \theta' \leq \alpha_2$ with θ' defined as $\theta' \equiv \theta$ if $\theta \leq 90^\circ$ and $\theta' \equiv 180 - \theta$ if $\theta > 90^\circ$, where θ is the angle between the track (or the cluster) and the lepton. The on-resonance data (points), with off-resonance data and fakes subtracted, are compared with generic $B\bar{B}$ Monte Carlo simulation (solid line). The $B\bar{B}$ Monte Carlo simulation has been normalized to the number of $B\bar{B}$ mesons in the data. The data and Monte Carlo samples used for these comparisons are described in section 4.2.1

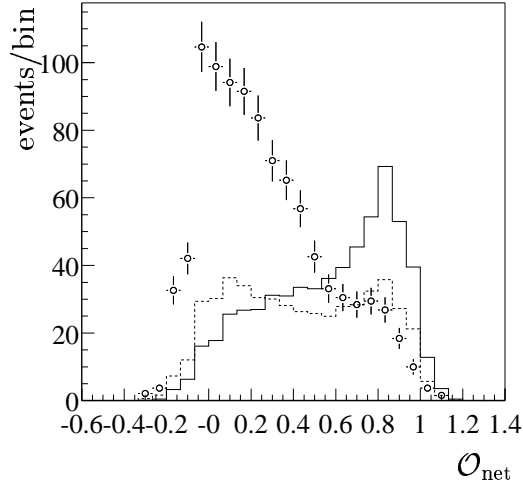


Figure 4.12: The neural net output distribution for the signal $B^+ \rightarrow \rho^0 e^+ \nu$ (solid line), the $b \rightarrow cl\nu$ background events (dashed line) and off-resonance data (open points). The normalization is arbitrary.

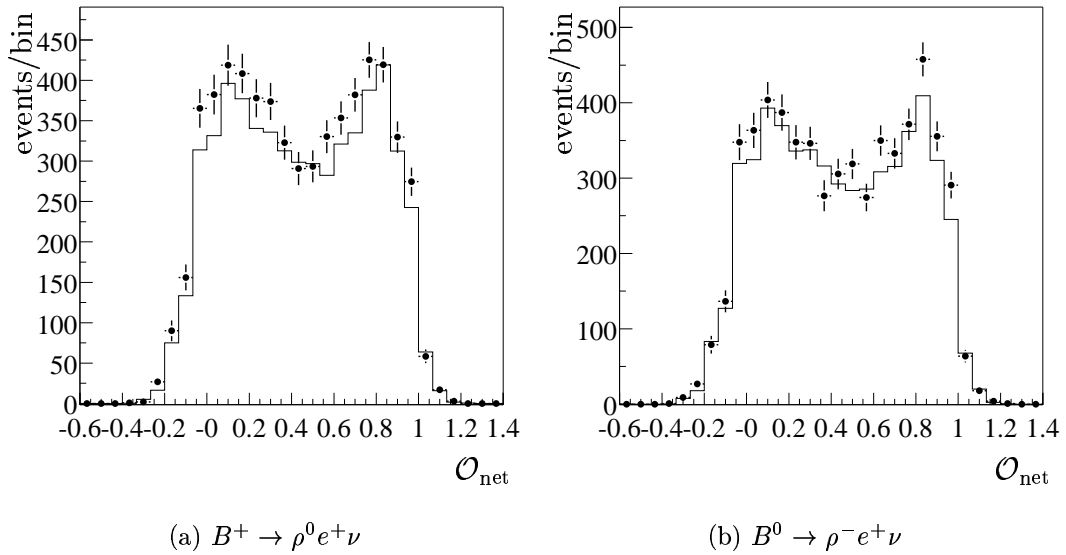


Figure 4.13: Comparison between on-resonance data (points), with off-resonance data and fakes subtracted, and generic $B\bar{B}$ Monte Carlo simulation (solid line) of the neural net output for (a) $B^+ \rightarrow \rho^0 e^+ \nu$ and (b) $B^0 \rightarrow \rho^- e^+ \nu$.

4.3.7 Cut Optimization

The relative error on the measured branching fraction choosing different values for the cuts has been studied. Subject to variation are the following cuts:

- $\cos \Delta\theta_{\min}$
- neural net output \mathcal{O}_{net}
- maximum lepton energy E_{max} in the HILEP region

The cut on the variable $\cos \theta_{BY}$ will not be optimized since the cut boundaries are given by the physical allowed range for signal events and one should avoid to cut into a region of large variation in the signal efficiency. The relative error f can be estimated by

$$f = \frac{\sigma_S}{S} = \sqrt{\frac{S + k \cdot B + k^2 \cdot B + C}{S^2}}, \quad (4.20)$$

where S is the number of Monte Carlo signal events ($B^0 \rightarrow \rho^- e^+ \nu$ and $B^+ \rightarrow \rho^0 e^+ \nu$ events including crossfeeds from other signal channels and assuming the branching fractions from Tables 4.3 and 4.4), B the number of off-resonance events, C the number of all other background events as determined from Monte Carlo simulation and k is the ratio of on to off-resonance luminosities. This can be derived as follows: The number of signal events is $S = N - kB - C$, where N is the number of on-resonance events. Taking \sqrt{N} and \sqrt{B} as errors for N and B one finds by error propagation $\sigma_S = \sqrt{N + k^2 \cdot B}$. With $N = S + kB + C$, f is the the relative error on S .

This study was done for the HILEP region where this analysis is most sensitive to the signal. The generic B meson decays samples (including the hard-lepton, very hard-lepton and no-charm samples), the signal Monte Carlo samples and the continuum Monte Carlo is used in this study. It is preferred to use continuum Monte Carlo for this optimization to avoid a statistical bias due to the low off resonance data statistics.

Fig. 4.14 shows the function f (Eq. 4.20) when varying one cut and fixing the two other cuts at the following values: $E_{\text{max}} < 2.7$ GeV, $\mathcal{O}_{\text{net}} > 0.6$, and $\cos \Delta\theta_{\min} > 0.8$. The cuts are chosen in such a way that they are in a flat region close to the minimum of the function f . The chosen cut values are indicated by lines in Fig. 4.14. In the case of the neural net output the cut is chosen slightly left of the minimum to avoid cutting into a steep slope of the signal efficiency and also to maintain a reasonably large signal efficiency.

4.3.8 Selection Results

Table 4.12 shows the selection efficiency in the five signal modes for events, where all tracks and clusters have been reconstructed and selected correctly (according to Monte Carlo truth). Note that the efficiencies which are relevant for the final extraction of the branching fraction are different and do not depend on Monte Carlo truth. These will be quoted later in this section. In Table 4.12 the efficiency is defined as the number

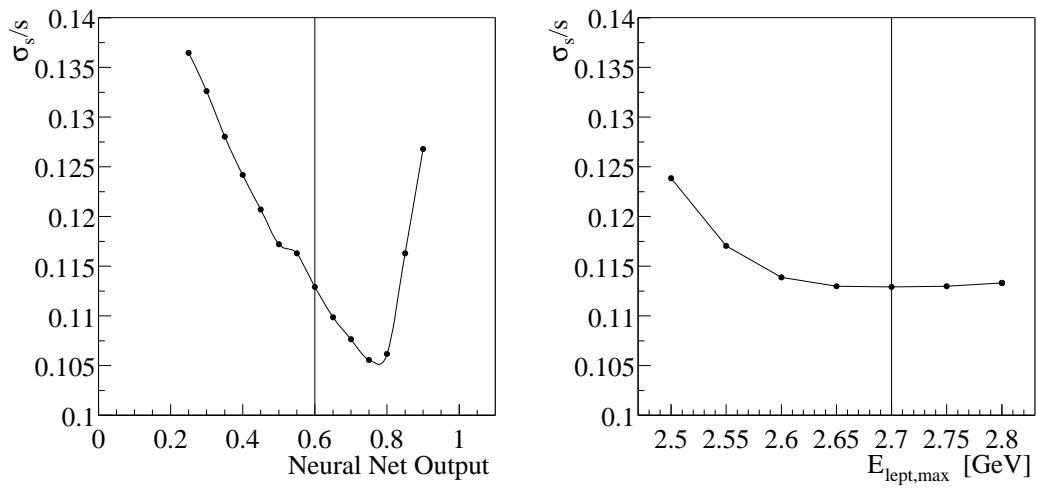
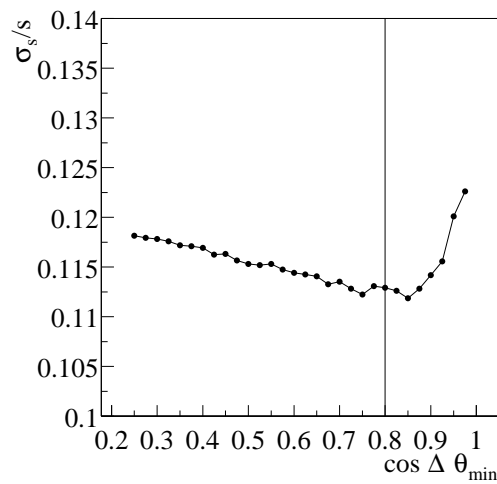
(a) \mathcal{O}_{net} (b) E_{max} (c) $\cos \Delta \theta_{\text{min}}$

Figure 4.14: The expected relative error on the branching fraction as function of the cut value on a selected variable (fixing the other cuts): **(a)** Neural net output \mathcal{O}_{net} , **(b)** maximum lepton energy, **(c)** $\cos \Delta \theta_{\text{min}}$.

cut	$\rho^0 e^+ \nu$	$\rho^+ e^- \nu$	$\pi^0 e^+ \nu$	$\pi^+ e^- \nu$	$\omega e^+ \nu$
generated	100 / 100	100 / 100	100 / 100	100 / 100	100 / 100
reconstructed	66.1 / 53.1	41.4 / 34.1	59.5 / 51.1	79.7 / 70.2	18.3 / 15.9
$N_{\text{tracks}}, N_{\text{cluster}}$	97.5 / 97.5	89.6 / 89.9	71.0 / 72.2	86.6 / 86.4	98.5 / 98.3
$\mathcal{R}_2 < 0.4$	90.1 / 84.4	91.5 / 85.3	89.4 / 81.6	88.0 / 82.1	88.3 / 80.6
$-0.72 < \cos \theta_e < 0.92$	100 / 100	100 / 100	98.9 / 98.7	99.0 / 99.1	99.3 / 99.5
$J/\Psi, e^+ e^-$ veto	100 / 100	100 / 100	99.4 / 99.2	99.5 / 98.9	99.1 / 99.3
hadron cuts	100 / 100	100 / 100	87.8 / 87.8	100 / 100	87.8 / 87.0
kaon veto for π_S	98.9 / 98.9	99.3 / 99.5	100 / 100	99.2 / 99.0	99.1 / 99.2
$ \cos \theta_{\text{miss}} < 0.9$	90.8 / 92.1	90.5 / 92.3	90.2 / 92.8	90.0 / 91.3	89.0 / 90.8
$ \cos \theta_{BY} < 1.1$	87.0 / 97.4	86.2 / 97.9	88.4 / 96.7	90.9 / 97.4	87.1 / 97.7
$\cos \Delta \theta_{\text{min}} > 0.8$	88.0 / 85.1	88.5 / 86.8	91.0 / 91.4	89.8 / 89.5	87.3 / 83.1
neural net	54.8 / 57.8	57.2 / 61.6	62.2 / 62.9	55.4 / 57.4	58.2 / 60.1
total	21.9 / 19.1	13.3 / 12.6	14.7 / 13.4	24.1 / 22.0	5.4 / 4.8

Table 4.12: Summary of selection efficiencies (in %) for the five electron channels (LOLEP/HILEP). The efficiencies are normalized to the number of events generated in the corresponding lepton-energy range. The efficiencies are calculated after all previous cuts are applied. The *reconstructed* efficiencies are mainly due to the geometric acceptance, and the track (cluster) reconstruction efficiencies. Details of the cuts are given in the text.

cut	$\rho^0 e^+ \nu$	$\rho^+ e^- \nu$	$\pi^0 e^+ \nu$	$\pi^+ e^- \nu$	$\omega e^+ \nu$
reconstructed	100 / 100	100 / 100	100 / 100	100 / 100	100 / 100
$N_{\text{tracks}}, N_{\text{cluster}}$	82.0 / 68.3	95.7 / 92.6	91.3 / 86.0	56.3 / 40.0	98.0 / 96.2
$\mathcal{R}_2 < 0.4$	45.8 / 44.4	48.0 / 46.6	46.5 / 45.5	41.4 / 39.9	54.8 / 52.8
$-0.72 < \cos \theta_e < 0.92$	97.0 / 95.0	97.7 / 96.1	97.2 / 95.4	96.6 / 94.6	97.9 / 95.8
$J/\Psi, e^+ e^-$ veto	78.2 / 77.7	79.1 / 76.8	80.9 / 78.6	79.3 / 78.6	79.5 / 77.7
hadron cuts	78.6 / 79.7	36.1 / 36.5	46.9 / 47.3	94.3 / 94.6	24.4 / 24.3
kaon veto for π_S	78.0 / 81.6	88.6 / 90.4	100 / 100	89.6 / 91.5	87.9 / 88.8
$ \cos \theta_{\text{miss}} < 0.9$	67.5 / 50.7	74.9 / 60.7	71.5 / 56.0	67.0 / 51.0	74.2 / 58.4
$ \cos \theta_{BY} < 1.1$	41.4 / 30.3	39.7 / 34.3	15.0 / 52.5	19.4 / 47.5	44.3 / 39.1
$\cos \Delta \theta_{\text{min}} > 0.8$	34.1 / 27.9	32.0 / 28.3	37.5 / 34.9	38.1 / 34.2	34.0 / 31.2
neural net	12.9 / 12.6	11.6 / 12.3	9.2 / 9.9	10.6 / 14.4	9.9 / 10.9
total	0.21 / 0.08	0.13 / 0.08	0.06 / 0.14	0.08 / 0.12	0.10 / 0.06

Table 4.13: Summary of selection efficiencies (in %) for combinations from continuum (off-resonance data) events (LOLEP/HILEP). Since real data are used, the generated numbers are not known. Details of the cuts are given in the text.

generated	reconstructed [%]				
	$B^\pm \rightarrow \rho^0 e\nu$	$B^0 \rightarrow \rho^\pm e\nu$	$B^\pm \rightarrow \omega e\nu$	$B^\pm \rightarrow \pi^0 e\nu$	$B^0 \rightarrow \pi^\pm e\nu$
$B^\pm \rightarrow \rho^0 e\nu$	5.72	1.83	0.53	0.42	0.93
$B^0 \rightarrow \rho^\pm e\nu$	2.16	4.67	0.62	0.62	0.80
$B^\pm \rightarrow \omega e\nu$	2.98	2.60	2.29	0.55	0.72
$B^\pm \rightarrow \pi^0 e\nu$	0.73	1.36	0.20	1.73	0.40
$B^0 \rightarrow \pi^\pm e\nu$	1.27	1.27	0.18	0.26	2.50

Table 4.14: Selection efficiencies for the modes $B^\pm \rightarrow \rho^0 e\nu$, $B^0 \rightarrow \rho^\pm e\nu$, $B^\pm \rightarrow \omega e\nu$, $B^\pm \rightarrow \pi^0 e\nu$, and $B^0 \rightarrow \pi^\pm e\nu$ in the LOLEP region. These efficiencies have been determined using simulated data (ISGW2 model). They are defined as the number of candidates passing all cuts (in each channel) divided by the number of all generated events (in the full lepton-energy range) for the specified channel.

of events reconstructed in the given lepton energy region divided by the number of all generated events in this lepton-energy range. The number in each row is relative to the number from the previous row. The last row shows the total efficiency. In each event the correct combination of signal tracks and clusters according to Monte Carlo truth information is selected. The numbers are based on the ISGW2 model.

Table 4.13 shows the efficiency for off-resonance data events after each cut. In this case the efficiency is defined as the number of candidates passing all cuts in each channel (possibly more than one per event) divided by the number of all reconstructed candidates in this channel and lepton-energy range.

Finally the total efficiencies for the five signal modes, which are used to determine the branching fraction (see Eq. 4.31), are shown in Tables 4.14 and 4.15. The efficiencies are determined using the ISGW2 model. They are defined here as the number of signal events that pass all cuts and are reconstructed in the specified channel divided by the number of all generated events for this channel. These efficiencies are normalized to the full lepton energy range. Note that a certain fraction of events in a given signal mode is reconstructed in one of the four other signal modes. These events are called crossfeed events.

4.4 Fit Method

To measure the branching fraction $\mathcal{B}(B \rightarrow \rho e\nu)$, an extended binned maximum-likelihood fit is performed simultaneously in two lepton-energy ranges and five decay modes. This section describes the fit method, the three fit variables, E_ℓ , M_{had} , and ΔE , and the various signal and background components.

generated	reconstructed [%]				
	$B^\pm \rightarrow \rho^0 e \nu$	$B^0 \rightarrow \rho^\pm e \nu$	$B^\pm \rightarrow \omega e \nu$	$B^\pm \rightarrow \pi^0 e \nu$	$B^0 \rightarrow \pi^\pm e \nu$
$B^\pm \rightarrow \rho^0 e \nu$	4.21	0.99	0.30	0.58	1.35
$B^0 \rightarrow \rho^\pm e \nu$	1.04	3.31	0.31	1.08	1.32
$B^\pm \rightarrow \omega e \nu$	1.97	1.55	1.57	0.94	0.88
$B^\pm \rightarrow \pi^0 e \nu$	0.23	0.41	0.07	1.28	0.40
$B^0 \rightarrow \pi^\pm e \nu$	0.42	0.47	0.05	0.33	1.63

Table 4.15: Selection efficiencies for the modes $B^\pm \rightarrow \rho^0 e \nu$, $B^0 \rightarrow \rho^\pm e \nu$, $B^\pm \rightarrow \omega e \nu$, $B^\pm \rightarrow \pi^0 e \nu$, and $B^0 \rightarrow \pi^\pm e \nu$ in the HILEP region. These efficiencies have been determined using simulated data (ISGW2 model). They are defined as the number of selected events passing all cuts divided by the number of all generated events (in the full lepton-energy range) for the specified channel.

4.4.1 Fit Variables

In the $B \rightarrow \rho e \nu$ and $B \rightarrow \omega e \nu$ channels, the fit variables are the invariant ρ (ω) mass $M_{\pi\pi(\pi)}$ and $\Delta E \equiv E_\rho + E_\ell + |\vec{p}_{\text{miss}}| - E_{\text{beam}}$. For the $B \rightarrow \pi e \nu$ modes, only ΔE is used. As discussed in the last section, these two fit variables and E_ℓ are constructed using the identified leptons, the final-state hadron, which is reconstructed using identified pions, and the neutrino inferred from the missing momentum and energy. The two lepton-energy ranges are HILEP and LOLEP as defined in section 4.3.

For the $\pi\pi$ modes, the data are divided into 10×10 bins over the (M_{had} , ΔE) region $0.25 \leq M_{\text{had}} \leq 2 \text{ GeV}/c^2$ and $|\Delta E| \leq 2 \text{ GeV}$. The $M_{\pi\pi}$ bin size for the fit is $175 \text{ MeV}/c^2$, for ΔE it is 400 MeV . The ω channel has 5 bins in the range $782 \pm 80 \text{ MeV}/c^2$ and 10 bins in $|\Delta E| \leq 2 \text{ GeV}$.

ΔE vs. $M(\pi\pi)$ distributions for the mode $B^+ \rightarrow \rho^0 e^+ \nu$ (HILEP region) are shown in Fig. 4.15 for Monte Carlo and in Fig. 4.16 for on- and off-resonance data. As can be seen, signal events are centered around $\Delta E = 0$ and the ρ mass in $M_{\pi\pi}$. Backgrounds from $b \rightarrow c e \nu$ and $b \rightarrow u e \nu$ tend to have $\Delta E < 0$. The resolution is largely dominated by the neutrino.

4.4.2 Contributions to the Fit

The fit includes contributions from $B \rightarrow \rho(\omega) e \nu$, $B \rightarrow \pi e \nu$, other $b \rightarrow u e \nu$ modes, $b \rightarrow c e \nu$, continuum, and also a contribution from fake electrons.

Signal Contribution

Monte Carlo simulation provides the shapes of the signal and crossfeed distributions. There is a significant fraction of crossfeed signal events. Isospin and quark model rela-

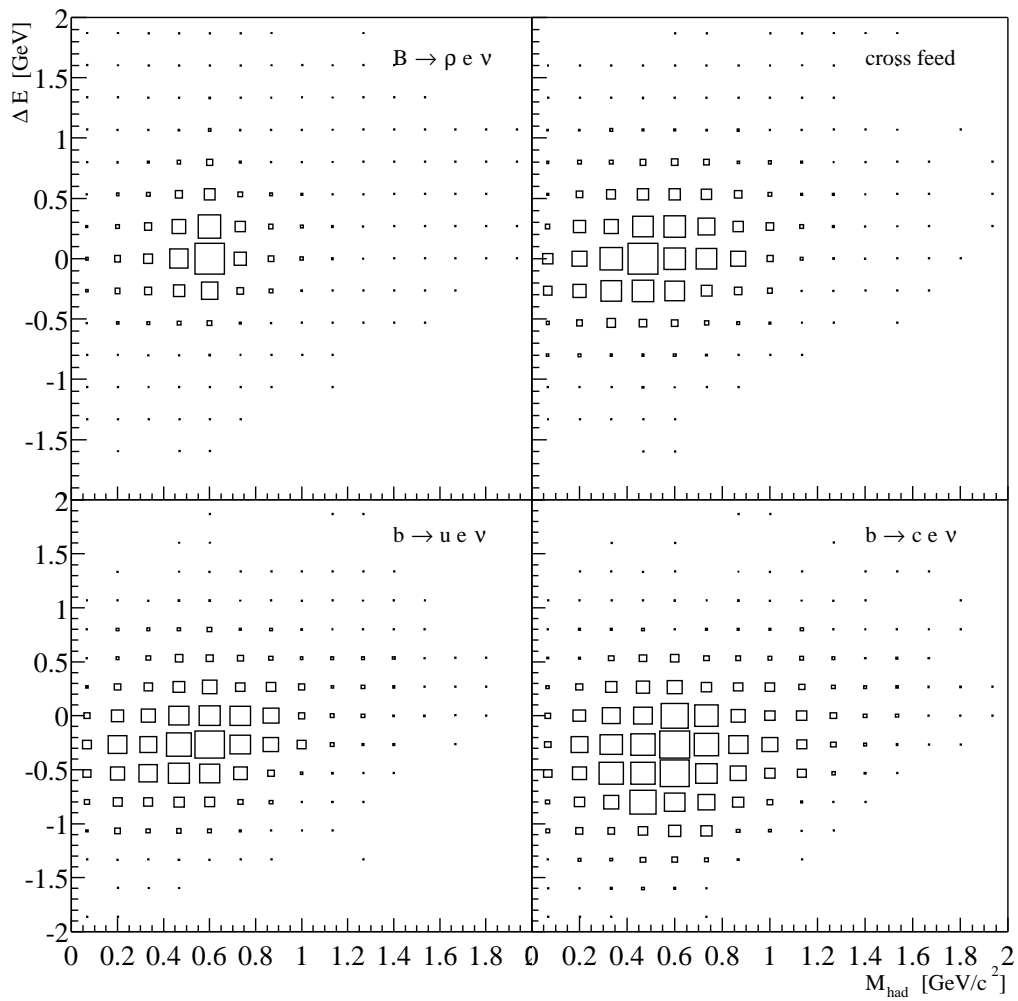


Figure 4.15: $M(\pi\pi)$ vs ΔE distribution in HILEP for various contributions to the fit. $B \rightarrow \rho e \nu$ signal events (top, left) peak at $\Delta E = 0$. $b \rightarrow u$ and $b \rightarrow c$ background events (bottom row) peak at $\Delta E < 0$.

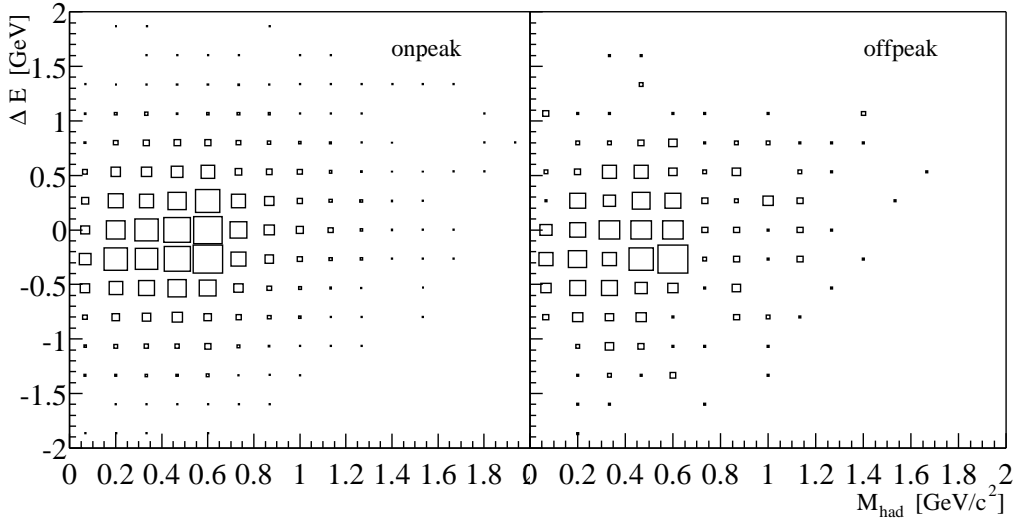


Figure 4.16: $M(\pi\pi)$ vs ΔE distributions in HILEP for the fitted on-resonance data (left) and off-resonance data (right).

tions are used to constrain the relative normalizations of $B^0 \rightarrow \rho^- \ell^+ \nu$, $B^+ \rightarrow \rho^0 \ell^+ \nu$, and $B^+ \rightarrow \omega \ell^+ \nu$:

$$\begin{aligned} \Gamma(B^0 \rightarrow \rho^- \ell^+ \nu) &= 2\Gamma(B^+ \rightarrow \rho^0 \ell^+ \nu), \\ \Gamma(B^+ \rightarrow \rho^0 \ell^+ \nu) &= \Gamma(B^+ \rightarrow \omega \ell^+ \nu). \end{aligned} \quad (4.21)$$

Thus there is only one fit parameter, $\mathcal{B}(B^0 \rightarrow \rho^- e^+ \nu)$, describing all three modes. A possible breaking of the isospin constraints is discussed in section 5.4.3. There is also an isospin relation between the charged and the neutral pion modes:

$$\Gamma(B^0 \rightarrow \pi^- \ell^+ \nu) = 2\Gamma(B^+ \rightarrow \pi^0 \ell^+ \nu). \quad (4.22)$$

With this relation the branching fraction $\mathcal{B}(B^0 \rightarrow \pi^- e^+ \nu)$ is the only fit parameter for this contribution.

$b \rightarrow ue\nu$ Background

The shape of the $b \rightarrow ue\nu$ modes other than the five signal modes is taken from Monte Carlo simulation. The normalization and to some extent also the shape of the $b \rightarrow u$ backgrounds is known poorly. Therefore there are two different fit parameters for the normalization of the $b \rightarrow u$ backgrounds, one for each lepton-energy bin. The fit will be able to determine the amount of $b \rightarrow u$ in each lepton bin freely. Monte Carlo simulation provides the relative normalization for each of the five modes. Uncertainties in the shape of this contribution are taken into account as a contribution to the systematic error (see section 5.4).

$b \rightarrow ce\nu$ Background

As for the other contributions, the shapes of the ΔE vs. M_{had} distribution is determined using Monte Carlo simulations. The LOLEP region is largely dominated by $b \rightarrow ce\nu$

decays. The fit uses five free parameters associated with the normalization of this background (one for each mode). The five free parameters are scale factors that give the overall normalization of the $b \rightarrow c\ell\nu$ background relative to that expected from the Monte Carlo simulation. With this freedom, uncertainties in the branching fractions of the $b \rightarrow c$ background modes are taken into account. Also effects of an imperfect detector simulation will be lessened by allowing for a free normalization.

A very small remaining background coming from events other than semileptonic decays (J/Ψ , τ , etc.) is included into the $b \rightarrow ce\nu$ background component.

Continuum Background

The off-resonance data give the shape and normalization of the continuum background. Monte Carlo simulation is not used for the continuum contribution since the continuum Monte Carlo shows discrepancies in shape and normalization when compared to off-resonance data. Note that since the amount of available off-resonance data is limited, it is important to treat the statistical fluctuations in this sample in a mathematically correct way. A simple binned likelihood fit will not give an unbiased answer. The details of the fit method are described below.

Fake Lepton Background

The normalization and shape for the fake electron contribution is determined using on-resonance and off-resonance data samples. The procedure is discussed in section 4.3.2.

4.4.3 The Extended Binned Maximum-Likelihood Fit

The fit method used in this analysis is a generalized binned maximum-likelihood method which takes into account the statistical fluctuations not only in the on- and off-resonance data samples but also in the Monte Carlo contributions. The full details of this method are described by R. Barlow and C. Beeston in [41]. The following paragraphs give an overview of the method.

The total likelihood function is derived by assuming that the number of events in bin i , from each fit contribution j , are generated from a Poisson distribution in the same way as the data:

$$\ln \mathcal{L} = \sum_{i=1}^n (d_i \ln f_i - f_i) + \sum_{i=1}^n \sum_{j=1}^m (a_{ji} \ln A_{ji} - A_{ji}), \quad (4.23)$$

where d_i is the number of on-resonance events and f_i is the sum of all fit contributions in bin i (see below). i are bins over the $(M_{\pi\pi(\pi)}, \Delta E)$ distribution, the two electron energy regions (HILEP and LOLEP) and the five decay modes ($B^+ \rightarrow \rho^0 e^+ \nu$, $B^0 \rightarrow \rho^- e^+ \nu$, $B^+ \rightarrow \pi^0 e^+ \nu$, $B^0 \rightarrow \pi^- e^+ \nu$, and $B^+ \rightarrow \omega e^+ \nu$). The numbers a_{ji} are the (integer) numbers of accepted Monte Carlo events or off-resonance events. There are $m = 9$ contributions a_{ji} to the fit:

- $j = 1 \dots 5$: One Monte Carlo contribution for each signal channel. For the $B^+ \rightarrow \rho^0 \ell^+ \nu$ channel for example this would be the direct signal contribution plus four crossfeed contributions from the other signal channels.
- $j = 6$: Monte Carlo backgrounds from $b \rightarrow c$ decays.
- $j = 7$: Monte Carlo backgrounds from other $b \rightarrow u$ decays than the signal channels.
- $j = 8$: Off-resonance data. This contribution is treated in the same way as the Monte Carlo contributions, even though real off-resonance data is used to describe this component rather than Monte Carlo simulation.
- $j = 9$: Fake leptons.

The A_{ji} are the estimated means of the Poisson distribution that the a_{ji} were generated from. The sum f_i of all fit contributions is then given by

$$f_i = \sum_{j=1}^m p_j w_{ji} A_{ji} , \quad (4.24)$$

where p_j is a parameter describing the relative normalization of the fit component j and w_{ji} is the weight for events from contribution j in bin i . There are different sources of event weights:

- The normalization to the number of $B\bar{B}$ events,
- the normalization to the on-resonance luminosity in case of the off-resonance and fake lepton fit contributions,
- the tracking efficiency correction.

In our case p_8 and p_9 are fixed to 1.0, i.e. to the ‘‘Monte Carlo’’ expectation. The other p_j are functions of the free fit parameters (see example below). The A_{ji} are a priori unknown and could be treated as free fit parameters. However, due to the large number of A_{ji} it is more realistic to follow a different approach. One can choose the A_{ji} in such a way that the total likelihood is maximal. Differentiating Eq. 4.23 with respect to A_{ji} gives a set of $m \times n$ equations:

$$\frac{d_i p_j w_{ji}}{f_i} - p_j w_{ji} + \frac{a_{ji}}{A_{ji}} - 1 = 0 \quad \forall i, j . \quad (4.25)$$

These nonlinear equations can be simplified [41]: Equations 4.25 can be rewritten as

$$1 - \frac{d_i}{f_i} = \frac{1}{p_j w_{ji}} \left(\frac{a_{ji}}{A_{ji}} - 1 \right) \quad \forall i, j . \quad (4.26)$$

The left hand side depends on i only. With

$$t_i = 1 - \frac{d_i}{f_i} , \quad (4.27)$$

Channel	HILEP		LOLEP	
	$\sum a_{i,off}$	$\sum A_{i,off}$	$\sum a_{i,off}$	$\sum A_{i,off}$
$B^+ \rightarrow \rho^0 \ell^+ \nu$	154 ± 12	156	354 ± 19	353
$B^0 \rightarrow \rho^- \ell^+ \nu$	154 ± 12	157	323 ± 18	330
$B^+ \rightarrow \omega \ell^+ \nu$	48 ± 7	55	91 ± 10	87

Table 4.16: Total number of off-resonance events given by the fit ($A_{i,off}$) compared with the total observed number of events ($a_{i,off}$) for the modes $B^+ \rightarrow \rho^0 \ell^+ \nu$, $B^0 \rightarrow \rho^- \ell^+ \nu$, $B^+ \rightarrow \omega \ell^+ \nu$ in the two lepton-energy bins.

the right hand side becomes

$$A_{ji} = \frac{a_{ji}}{1 + p_j t_i w_{ji}}. \quad (4.28)$$

Thus, for a given set of p_j , the $m \times n$ unknown quantities A_{ji} are given by the n unknown quantities t_i . These quantities can be calculated numerically using the system of n equations,

$$\frac{d_i}{1 - t_i} = f_i = \sum_{j=1}^m \frac{p_j a_{ji} w_{ji}}{1 + p_j t_i w_{ji}}. \quad (4.29)$$

The Newton method is used to solve for the t_i . Note that special considerations have been applied here if the number of events a_{ji} are zero. This is described in detail in [41]. Knowing the A_{ji} , one can then minimize $-2 \log \mathcal{L}$ using the MINUIT package. The calculation of the A_{ji} is done at every step of the MINUIT minimization procedure. For finite statistics, the numbers a_{ji} and A_{ji} have not to be equal. Table 4.16 shows, for the case of the continuum contribution, that the sums of a_{ji} and A_{ji} are compatible.

The method has the property of including errors owing to finite MC statistics into the statistical error of the fit result. Other analyses include this contribution into the systematic error of the final results.

As discussed in section 4.4.2, there are 9 free fit parameters (see Table 4.17):

- $\mathcal{B}(B^0 \rightarrow \rho^- e^+ \nu)$, $par(1)$;
- $\mathcal{B}(B^0 \rightarrow \pi^- e^+ \nu)$, $par(2)$;
- the scale factors of the $b \rightarrow ue\nu$ background in each lepton-energy bin, $par(3)$ and $par(4)$;
- the scale factors, one for each mode, that give the overall normalization of the $b \rightarrow ce\nu$ background relative to that expected from the Monte Carlo simulation, $par(5)$ through $par(9)$.

Number	Name	Definition	MC value
1	$\text{BR}(\rho^\pm)$	$\mathcal{B}(B^0 \rightarrow \rho^\pm e\nu)$	$2.6 \cdot 10^{-4}$
2	$\text{BR}(\pi^\pm)$	$\mathcal{B}(B^0 \rightarrow \pi^\pm e\nu)$	$1.8 \cdot 10^{-4}$
3	$bue\nu(HI)$	Scale factor $b \rightarrow ue\nu$ (HILEP)	1
4	$bue\nu(LO)$	Scale factor $b \rightarrow ue\nu$ (LOLEP)	1
5	$bce\nu(\rho^0)$	Scale factor $b \rightarrow ce\nu$ ($B^+ \rightarrow \rho^0 e^+ \nu$)	1
6	$bce\nu(\rho^\pm)$	Scale factor $b \rightarrow ce\nu$ ($B^0 \rightarrow \rho^\pm e^+ \nu$)	1
7	$bce\nu(\pi^0)$	Scale factor $b \rightarrow ce\nu$ ($B^+ \rightarrow \pi^0 e^+ \nu$)	1
8	$bce\nu(\pi^\pm)$	Scale factor $b \rightarrow ce\nu$ ($B^0 \rightarrow \pi^\pm e^+ \nu$)	1
9	$bce\nu(\omega)$	Scale factor $b \rightarrow ce\nu$ ($B^+ \rightarrow \omega e^+ \nu$)	1

Table 4.17: Free parameters used in the likelihood fit (see text).

In the case of the $B^+ \rightarrow \rho^0 e^+ \nu$ channel in HILEP, the function f_i is:

$$\begin{aligned}
f_i &= p_1 \cdot w_{\rho^\pm}^i \cdot a_{\rho^\pm}^i + p_2 \cdot w_{\rho^0}^i \cdot a_{\rho^0}^i + p_3 \cdot w_\omega^i \cdot a_\omega^i \\
&+ p_4 \cdot w_{\pi^\pm}^i \cdot a_{\pi^\pm}^i + p_5 \cdot w_{\pi^0}^i \cdot a_{\pi^0}^i \\
&+ p_6 \cdot w_{b \rightarrow ul\nu}^i \cdot a_{b \rightarrow ul\nu}^i \\
&+ p_7 \cdot w_{b \rightarrow cl\nu}^i \cdot a_{b \rightarrow cl\nu}^i \\
&+ p_8 \cdot k \cdot a_{off}^i \\
&+ p_9 \cdot w_{fake, B\bar{B}}^i \cdot a_{fake, B\bar{B}}^i,
\end{aligned} \tag{4.30}$$

where the coefficients p_j are related to the fit parameters $par(1-9)$ in the following way:

$$\begin{aligned}
p_1 &= par(1) \cdot N_{B\bar{B}} \cdot \epsilon_{\rho^\pm, \rho^0} \cdot \frac{1}{a_{\rho^\pm}} \\
p_2 &= par(1) \cdot \frac{1}{2} \cdot \frac{\tau_{B^+}}{\tau_{B^0}} \cdot N_{B\bar{B}} \cdot \epsilon_{\rho^0, \rho^0} \cdot \frac{1}{a_{\rho^0}} \\
p_3 &= par(1) \cdot \frac{1}{2} \cdot \frac{\tau_{B^+}}{\tau_{B^0}} \cdot N_{B\bar{B}} \cdot \epsilon_{\omega, \rho^0} \cdot \frac{1}{a_\omega} \\
p_4 &= par(2) \cdot N_{B\bar{B}} \cdot \epsilon_{\pi^\pm, \rho^0} \cdot \frac{1}{a_{\pi^\pm}} \\
p_5 &= par(2) \cdot \frac{1}{2} \cdot \frac{\tau_{B^+}}{\tau_{B^0}} \cdot N_{B\bar{B}} \cdot \epsilon_{\pi^0, \rho^0} \cdot \frac{1}{a_{\pi^0}} \\
p_6 &= par(3) \\
p_7 &= par(6) \\
p_8 &= 1 \\
p_9 &= 1.
\end{aligned} \tag{4.31}$$

The numbers a_k are $a_k = \sum w_{ki} a_{ki}$, with the sum running over all bins in HILEP and channel k . The efficiency ϵ_{kl} is the efficiency in HILEP for events generated in channel k to be reconstructed in channel l . These are given in Table 4.15. $\frac{\tau_{B^+}}{\tau_{B^0}} = 1.062 \pm 0.029$ is the lifetime ratio for charged and neutral B mesons taken from [22]. $N_{B\bar{B}} = 55.2 \times 10^6$ is the number of $B\bar{B}$ pairs in the on-resonance data sample (see section 3). The fake lepton contribution $a_{fake, B\bar{B}}^i$ is given by Eq. 4.8.

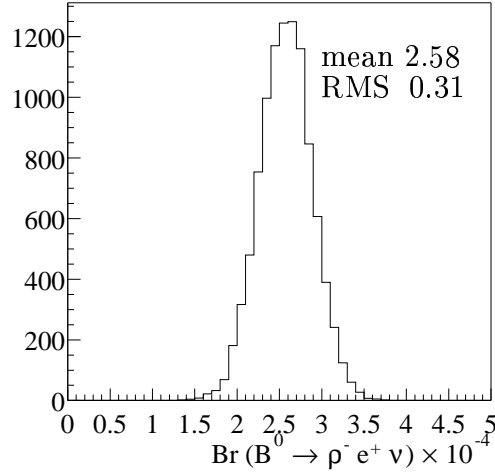


Figure 4.17: Fitted branching fraction for 10000 toy Monte Carlo samples. $\mathcal{B}(B^0 \rightarrow \rho^- \ell^+ \nu) = 2.6 \times 10^{-4}$ has been used to generate the samples. The fit finds the correct branching fraction on average with a very small bias. The spread of results is 12%.

4.4.4 Checks of the Fit Method

A toy Monte Carlo study was used to verify the stability of the fit method and to check its statistical error. One way of doing such a check would be to use many independent Monte Carlo samples as input to the fit method. Since the amount of available signal and background Monte Carlo is limited this approach does not seem feasible. The approach followed here is to use the same Monte Carlo samples which are used in the fit but to generate independent samples by applying a bin by bin fluctuation in the two dimensional histograms. This is described in the following paragraph.

In each two dimensional histogram (ΔE vs M_{had}) the expected number of events in each bin i from each contribution is:

$$N_{i,on} = N_{i,signal} + N_{i,backgrounds} + N_{i,continuum} \quad (4.32)$$

$$N_{i,off} = N_{i,continuum}/k \quad (4.33)$$

$$N_{i,signal} = N_{i,\rho^0} + N_{i,\rho^\pm} + N_{i,\pi^0} + N_{i,\pi^\pm} + N_{i,\omega} \quad (4.34)$$

$$N_{i,backgrounds} = N_{i,b \rightarrow c} + N_{i,b \rightarrow u} + N_{i,fake} \quad (4.35)$$

For the estimation of $N_{i,signal}$ signal Monte Carlo is used, $N_{i,backgrounds}$ is determined from the generic B meson decays sample. A continuum Monte Carlo sample is used for $N_{i,continuum}$. The ratio of on- to off-resonance luminosities is k . All events are weighted to obtain the amount of events which is expected in the data. The pseudo Monte Carlo sample is now generated by assuming that the number of events in each bin for contribution j can be generated from a Poisson distribution with the mean $\mu_{ij} = N_{ij}$. One has to be careful that μ_{ij} is a good estimator for the true mean in each bin. This is not true for bins with zero entries. In this case, the generated toy bin contents would always be zero for all generated samples since the mean is equal to zero. Hence for samples with low statistics the generated distributions will not be statistically independent. For this reason the actual off-resonance data is not used to determine $N_{i,off}$ but rather con-

tinuum Monte Carlo which is available with much higher statistics, thus avoiding bins with a small number of entries.

The result of 10000 toy Monte Carlo fits is shown in Fig. 4.17. The central value of the branching fraction used for generating the toy samples was $2.6 \cdot 10^{-4}$. The toy Monte Carlo shows that the fit gives the right answer on average with a negligible bias. The expected statistical error is given by the spread of the fit results. The root mean square is $0.31 \cdot 10^{-4}$ (12%).

4.5 Reweighting Technique

Instead of generating dedicated Monte Carlo samples for each of the form-factor models, a reweighting technique is used. Monte Carlo events for the five signal channels have been generated with a flat distribution in the phase space (the *phase space* Monte Carlo). For each event the differential decay rate, given by Eq. 2.25 for the generated q^2 , $\cos \theta_l$, $\cos \theta_V$, and χ is calculated and applied as an event weight to determine the kinematic distributions predicted by each model.

This technique has been verified by comparing a Monte Carlo simulation for the ISGW2 model with the corresponding reweighted phase space Monte Carlo. Fig. 4.18 shows the lepton energy, q^2 , $\cos \theta_l$, and $\cos \theta_V$ distributions for the Monte Carlo generated with ISGW2 model (solid line), phase-space Monte Carlo (dotted line), and reweighted phase-space Monte Carlo (dashed line). Good agreement between the generated and reweighted (ISGW2) distributions is observed. The efficiencies calculated from the reweighted Monte Carlo,

$$\epsilon = \frac{N_{select}}{N_{tot}} \quad \Longrightarrow \quad \epsilon = \frac{\sum_{i=1}^{N_{select}} w}{\sum_{i=1}^{N_{tot}} w}, \quad (4.36)$$

where w is the weight and N the total or selected number of events, agree well with the efficiencies given in Table 4.14. It has been verified that the fit result using the reweighted phase space Monte Carlo simulation agrees with the result using the ISGW2 Monte Carlo simulation to better than 1%.

4.6 Reconstruction of q^2

In the decay $B \rightarrow \rho \ell \nu$ the kinematic variable q^2 is given by

$$q^2 = M_B^2 + M_\rho^2 - 2E_B E_\rho + 2\vec{p}_B \cdot \vec{p}_\rho. \quad (4.37)$$

Since the direction of the B meson in each event is not known there is an ambiguity in the reconstruction of this variable. However with the constraint $E_B = E_{T(4S)}/2$, the minimum and maximum possible values of q^2 can be determined. These correspond to the kinematic configurations where the B momentum direction is closest to, or furthest

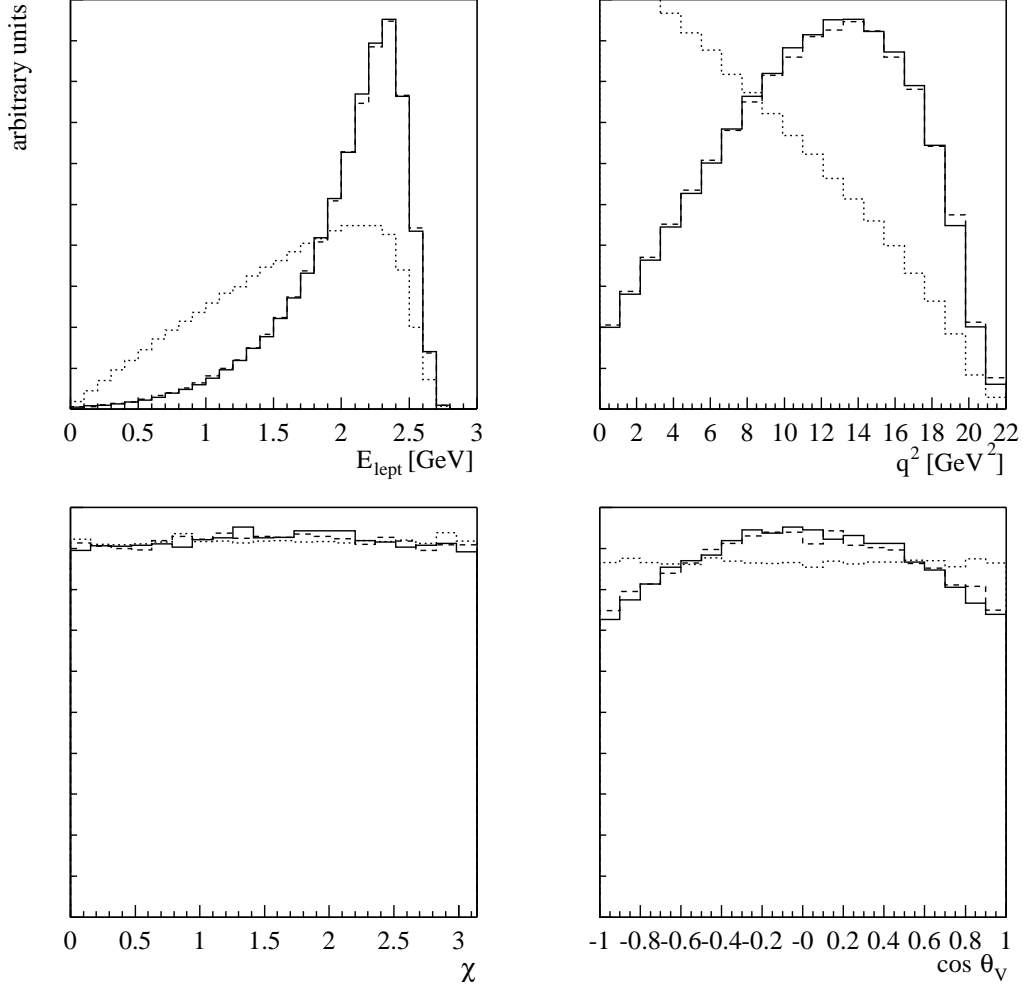


Figure 4.18: E_{lept} , q^2 , $\cos \theta_\ell$, and $\cos \theta_V$ distributions for the ISGW2 generated Monte Carlo (solid line), the reweighted phase space Monte Carlo simulating the ISGW2 model (dashed line) and the phase space Monte Carlo before reweighting (dotted line).

from, the ρ momentum direction. The midpoint $q_{\text{avg}}^2 = (q_{\text{min}}^2 + q_{\text{max}}^2)/2$ of the allowed q^2 range is a good estimate of q^2 . With $\vec{p}_B \cdot \vec{p}_\rho = |\vec{p}_B| |\vec{p}_\rho| \cos \theta_{B,\rho}$ one finds

$$q_{\text{min,max}}^2 = M_B^2 + M_\rho^2 - 2E_B E_\rho + 2|\vec{p}_B| |\vec{p}_\rho| \cos \theta_{B,\rho}^{\text{min,max}}, \quad (4.38)$$

where

$$\cos \theta_{B,\rho}^{\text{min}} = \cos(\theta_{BY} - \theta_{Y,\rho}) \quad (4.39)$$

$$= \cos \theta_{BY} \cos \theta_{Y,\rho} + \sin \theta_{BY} \sin \theta_{Y,\rho}, \text{ and}$$

$$\cos \theta_{B,\rho}^{\text{max}} = \cos(\theta_{BY} + \theta_{Y,\rho}) \quad (4.40)$$

$$= \cos \theta_{BY} \cos \theta_{Y,\rho} - \sin \theta_{BY} \sin \theta_{Y,\rho}.$$

$\cos \theta_{BY}$ is given by Eq. 4.12. The reconstructed q^2 distribution is shown in Fig. 4.19. A narrow peak can be seen for events with all particles reconstructed correctly and a broad peak for events where at least one particle has been reconstructed incorrectly.

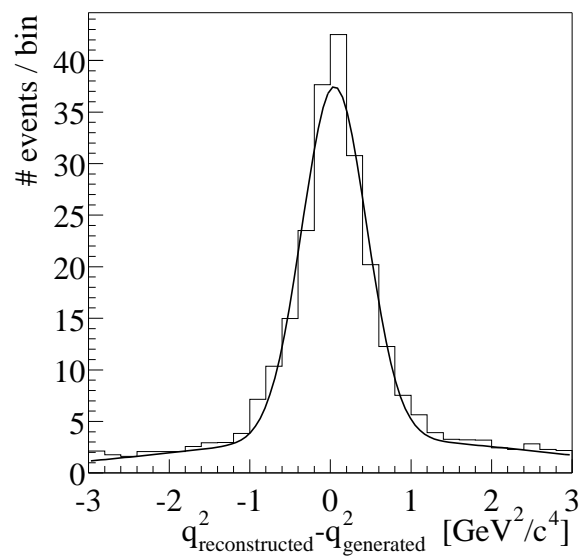


Figure 4.19: Resolution of the reconstructed variable q^2 for signal Monte Carlo events. The curve is a fit of two Gaussian distributions. The narrow Gaussian with $\sigma = 0.4 \text{ GeV}^2/c^4$ corresponds to events with all particles reconstructed correctly. The wider distribution with $\sigma = 2.3 \text{ GeV}^2/c^4$ is due to events where at least one particle has been reconstructed incorrectly.

Chapter 5

Results

In this chapter the fit results for the branching fraction $B \rightarrow \rho \ell \nu$ and the determination of the CKM matrix element $|V_{ub}|$ are presented. Results for five different form-factor models are listed separately. The final result will be a combination of these five results.

5.1 Branching-Fraction Fit Result

The fit result for each form-factor model and a combined result are summarized in Fig. 5.1. The $B^0 \rightarrow \rho^- \ell^+ \nu$ branching fraction varies from $(2.79 \pm 0.35) \times 10^{-4}$ for the ISGW2 model to $(3.99 \pm 0.52) \times 10^{-4}$ for the LCSR model. The combined result for the $B^0 \rightarrow \rho^- e^+ \nu$ branching fraction is determined by taking the unweighted mean of all form-factor results. The statistical and systematic errors of the combined result are determined by taking the mean of the relative errors of each individual result. The fit stability for each model has been studied in the same way as for the ISGW2 result. One finds that all models behave in a similar way. A common systematic error is assigned for all models. A theoretical error is assigned to take into account the substantial spread in results among the form-factor models. The theoretical error is taken to be one half of the full spread of the results. The combined result is

$$\mathcal{B}(B^0 \rightarrow \rho^- e^+ \nu) = (3.39 \pm 0.44 \pm 0.52 \pm 0.60) \times 10^{-4}, \quad (5.1)$$

where the errors are statistical (including Monte Carlo statistics), systematic, and theoretical respectively.

Table 5.1 shows the $B^+ \rightarrow \rho^0 \ell^+ \nu$, $B^0 \rightarrow \rho^- \ell^+ \nu$, and $B^+ \rightarrow \omega \ell^+ \nu$ selection efficiencies using different models. A summary of the fitted yields of each fit contribution and for each form-factor model is shown in Tables 5.2 through 5.4.

Table 5.5 shows the values of the 9 fit parameters, defined in Table 4.17, for each form-factor model. The fit parameters describing the $b \rightarrow c$ backgrounds are in reasonable agreement with Monte Carlo expectations. The average of the five parameters agrees within 9%. Also, the π crossfeed agrees with Monte Carlo expectations within errors. The fit parameters which describe the $b \rightarrow u$ downfeed background in the HILEP and LOLEP region are almost within one sigma of the expectation. Note that the LOLEP

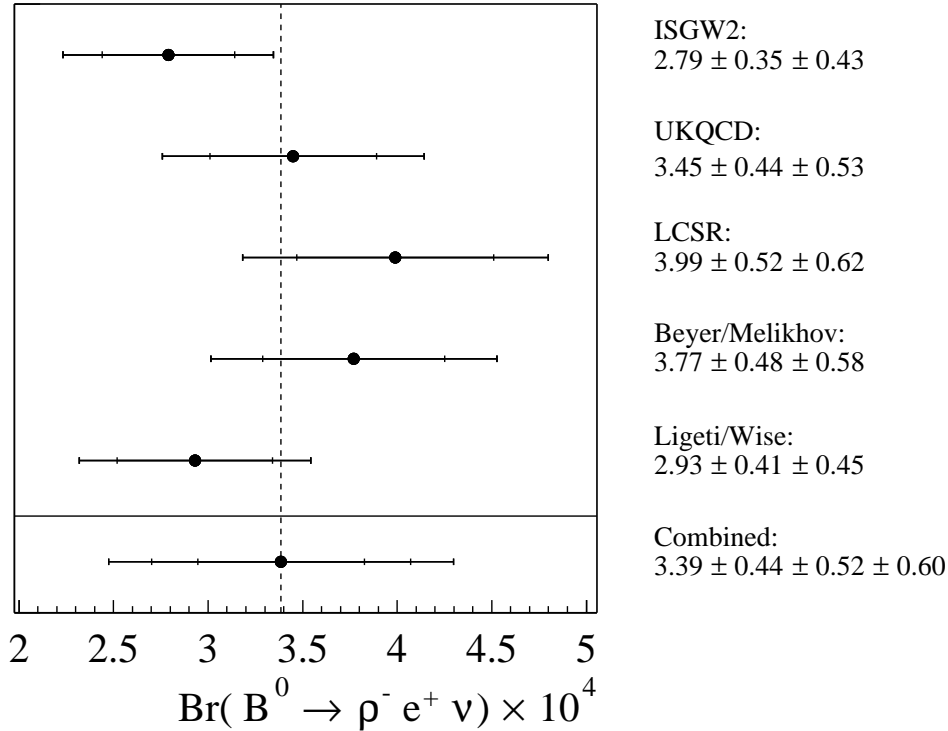


Figure 5.1: The $B^0 \rightarrow \rho^- e^+ \nu$ branching fraction results using the ISGW2, UKQCD, LCSR, Beyer/Melikhov, and Ligeti/Wise form-factors. The errors shown are statistical, systematic, and (only in case of the combined result) theoretical, successively combined in quadrature. The combined central value is determined by taking the unweighted mean of all form-factor results. The statistical and systematic errors of the combined result are determined by taking the means of the relative errors of each individual result, and its theoretical error is taken to be one half of the full spread of the results.

	ISGW2	UKQCD	LCSR	B/M	L/W
$B^\pm \rightarrow \rho^0 e \nu$:					
HILEP	4.2%	3.4%	2.8%	3.0%	4.0%
LOLEP	5.7%	5.0%	4.3%	4.6%	6.0%
$B^0 \rightarrow \rho^\pm e \nu$:					
HILEP	3.3%	2.7%	2.2%	2.4%	3.1%
LOLEP	4.7%	4.1%	3.6%	3.8%	4.9%
$B^\pm \rightarrow \omega e \nu$					
HILEP	1.6%	1.2%	1.0%	1.1%	1.4%
LOLEP	2.3%	2.0%	1.8%	2.0%	2.3%

Table 5.1: Signal efficiencies for the ISGW2, UKQCD, LCSR, Beyer/Melikhov (B/M), and Ligeti/Wise (L/W) models, defined as accepted number of events in the HILEP or LOLEP region divided by the generated number of events of all momenta.

region is dominated by $b \rightarrow c$ backgrounds. Even a small variation in the shape of this background can cause a systematic deviation of the fitted $b \rightarrow u$ downfeed normalization. The influence on the fitted branching fraction is however very small. Downfeeds

	ISGW2	UKQCD	LCSR	B/M	L/W
HILEP:					
signal	324 ± 40	322 ± 41	310 ± 40	315 ± 40	320 ± 45
crossfeed	363 ± 42	347 ± 41	341 ± 41	353 ± 42	349 ± 45
downfeed	151 ± 62	180 ± 60	192 ± 59	181 ± 59	174 ± 62
$b \rightarrow c$	351 ± 5	352 ± 5	352 ± 5	353 ± 5	352 ± 5
off-res.	912 ± 73	912 ± 73	912 ± 73	912 ± 73	912 ± 73
LOLEP:					
signal	440 ± 55	474 ± 61	478 ± 62	474 ± 60	488 ± 68
crossfeed	725 ± 86	750 ± 92	761 ± 94	774 ± 95	769 ± 100
downfeed	1623 ± 287	1578 ± 291	1547 ± 294	1529 ± 293	1549 ± 299
$b \rightarrow c$	32940 ± 439	32989 ± 441	33020 ± 442	33038 ± 442	32996 ± 443
off-res.	2063 ± 110	2063 ± 110	2063 ± 110	2063 ± 110	2063 ± 110

Table 5.2: Fitted yields of the $B^+ \rightarrow \rho^0 e^+ \nu$ mode in the HILEP and LOLEP regions using the ISGW2, UKQCD, LCSR, Beyer/Melikhov (B/M), and Ligeti/Wise (L/W) models. The errors are statistical only. Errors on the signal and crossfeed yields are completely correlated.

	ISGW2	UKQCD	LCSR	B/M	L/W
HILEP:					
signal	510 ± 63	505 ± 65	487 ± 63	494 ± 62	505 ± 70
crossfeed	262 ± 32	249 ± 32	245 ± 32	253 ± 32	250 ± 34
downfeed	136 ± 55	162 ± 54	173 ± 53	163 ± 53	157 ± 56
$b \rightarrow c$	396 ± 5	397 ± 5	397 ± 5	397 ± 5	397 ± 5
off-res.	917 ± 73	917 ± 73	917 ± 73	917 ± 73	917 ± 73
LOLEP:					
signal	718 ± 89	778 ± 99	789 ± 102	782 ± 99	799 ± 111
crossfeed	538 ± 73	551 ± 78	559 ± 79	567 ± 80	564 ± 82
downfeed	1518 ± 268	1476 ± 273	1447 ± 275	1430 ± 274	1449 ± 280
$b \rightarrow c$	32454 ± 420	32472 ± 421	32498 ± 422	32521 ± 421	32477 ± 422
off-res.	1928 ± 106	1928 ± 106	1928 ± 106	1928 ± 106	1928 ± 106

Table 5.3: Fitted yields of the $B^0 \rightarrow \rho^- e^+ \nu$ mode in the HILEP and LOLEP regions using the ISGW2, UKQCD, LCSR, Beyer/Melikhov (B/M), and Ligeti/Wise (L/W) models. The errors are statistical only. Errors on the signal and crossfeed yield are completely correlated.

from states with very large invariant hadronic masses will contribute preferably at lower lepton energies. These states are likely not to be modeled adequately in the Monte Carlo simulation. A systematic error will be included to cover uncertainties in the shape of the $b \rightarrow u$ downfeed component.

The correlations between the fit parameters are shown in Table 5.6. One observes that the branching fraction $B^0 \rightarrow \rho^- e^+ \nu$ (parameter 1) is anticorrelated with the $\mathcal{B}(B^0 \rightarrow \pi^- e^+ \nu)$ and with the $b \rightarrow ue\nu$ parameters in the HILEP and LOLEP regions (parameters 3 and 4).

	ISGW2	UKQCD	LCSR	B/M	L/W
HILEP:					
signal	132 ± 16	120 ± 15	121 ± 16	128 ± 16	121 ± 17
crossfeed	79 ± 9	80 ± 10	79 ± 10	81 ± 10	77 ± 10
downfeed	54 ± 22	65 ± 21	69 ± 21	65 ± 21	62 ± 22
$b \rightarrow c$	139 ± 2	139 ± 2	139 ± 2	139 ± 2	139 ± 2
off-res.	321 ± 43	321 ± 43	321 ± 43	321 ± 43	321 ± 43
LOLEP:					
signal	192 ± 24	202 ± 26	215 ± 28	222 ± 28	199 ± 28
crossfeed	165 ± 19	177 ± 21	179 ± 22	183 ± 22	182 ± 23
downfeed	572 ± 101	556 ± 103	545 ± 104	539 ± 103	546 ± 105
$b \rightarrow c$	11294 ± 196	11311 ± 197	11313 ± 197	11312 ± 196	11323 ± 198
off-res.	508 ± 55	508 ± 55	508 ± 55	508 ± 55	508 ± 55

Table 5.4: Fitted yields of the $B^+ \rightarrow \omega e^+ \nu$ mode in the HILEP and LOLEP regions using the ISGW2, UKQCD, LCSR, Beyer/Melikhov (B/M), and Ligeti/Wise (L/W) models. The errors are statistical only. Errors on the signal and crossfeed yield are completely correlated.

Parameters	ISGW2	UKQCD	LCSR	B/M	L/W
1. $\text{BR}(\rho)/10^{-4}$	2.79 ± 0.35	3.45 ± 0.44	3.99 ± 0.52	3.77 ± 0.48	2.93 ± 0.41
2. $\text{BR}(\pi)/10^{-4}$	1.87 ± 0.56	1.79 ± 0.58	1.75 ± 0.59	1.69 ± 0.58	1.83 ± 0.59
3. $b\ell\nu(HI)$	0.67 ± 0.27	0.78 ± 0.26	0.85 ± 0.26	0.80 ± 0.26	0.77 ± 0.28
4. $b\ell\nu(LO)$	1.36 ± 0.24	1.32 ± 0.24	1.29 ± 0.25	1.28 ± 0.24	1.29 ± 0.25
5. $b\ell\nu(\rho^0)$	1.08 ± 0.01	1.09 ± 0.01	1.09 ± 0.01	1.08 ± 0.01	1.08 ± 0.01
6. $b\ell\nu(\rho^\pm)$	1.07 ± 0.01	1.07 ± 0.01	1.07 ± 0.01	1.07 ± 0.01	1.07 ± 0.01
7. $b\ell\nu(\pi^0)$	1.13 ± 0.03	1.13 ± 0.03	1.13 ± 0.03	1.13 ± 0.03	1.13 ± 0.03
8. $b\ell\nu(\pi^\pm)$	1.12 ± 0.03	1.12 ± 0.03	1.12 ± 0.03	1.12 ± 0.03	1.11 ± 0.03
9. $b\ell\nu(\omega)$	1.04 ± 0.02	1.04 ± 0.02	1.04 ± 0.02	1.04 ± 0.02	1.04 ± 0.02

Table 5.5: Result of the binned likelihood fit of the distribution ($M_{\pi\pi(\pi)}, \Delta E$) simultaneously for the 5 decay modes and the 2 lepton-energy bins (LOLEP, HILEP). The parameters have been defined in Table 4.17, parameters 3-9 are given relative to the MC expectation. The ISGW2, UKQCD, LCSR, Beyer/Melikhov (B/M), and Ligeti/Wise (L/W) models has been used to simulate the $B^+ \rightarrow \rho^0 \ell^+ \nu$, $B^0 \rightarrow \rho^- \ell^+ \nu$ and $B^+ \rightarrow \omega \ell^+ \nu$ events.

5.2 Fit Projections

The projections of the ISGW2 fit for the two lepton-energy bins and for each channel are shown in Figs. 5.2 through 5.5. Good agreement between the data and fit result can be observed in each of these figures. The fits for the other four form-factor models show similar agreement. A significant $B \rightarrow \rho e \nu$ signal can be seen in the $M_{\pi\pi}$ and ΔE distributions in HILEP.

The ISGW2 projections of lepton-energy distributions for the $B^+ \rightarrow \rho^0 e^+ \nu$ and $B^0 \rightarrow \rho^- e^+ \nu$ modes are shown in Figs. 5.6 and 5.7. Good agreement between data and fit result is observed in the full lepton-energy range used in the fit. A large excess of

PAR	CORRELATION COEFFICIENTS								
NO.	1	2	3	4	5	6	7	8	9
1	1.000	-0.507	-0.793	-0.416	0.173	0.154	0.140	0.234	0.135
2	-0.507	1.000	0.218	-0.025	0.051	0.038	-0.206	-0.424	0.074
3	-0.793	0.218	1.000	0.426	-0.213	-0.192	-0.097	-0.129	-0.175
4	-0.416	-0.025	0.426	1.000	-0.781	-0.762	-0.347	-0.332	-0.638
5	0.173	0.051	-0.213	-0.781	1.000	0.632	0.292	0.277	0.525
6	0.154	0.038	-0.192	-0.762	0.632	1.000	0.292	0.280	0.515
7	0.140	-0.206	-0.097	-0.347	0.292	0.292	1.000	0.235	0.230
8	0.234	-0.424	-0.129	-0.332	0.277	0.280	0.235	1.000	0.210
9	0.135	0.074	-0.175	-0.638	0.525	0.515	0.230	0.210	1.000
global	0.892	0.753	0.822	0.926	0.802	0.789	0.436	0.572	0.655

Table 5.6: Correlations between the 9 parameters given by Minuit. The parameters have been defined in Table 4.17. The last line gives the maximum correlation with any linear combination of the other parameters.

$B^+ \rightarrow \rho^0 e^+ \nu$ and $B^0 \rightarrow \rho^- e^+ \nu$ signal is observed above the $b \rightarrow c$ lepton-energy endpoint.

The reconstructed q^2 distribution is shown in Fig. 5.8 for the mode $B^+ \rightarrow \rho^0 e^+ \nu$ and Fig. 5.9 for $B^0 \rightarrow \rho^- e^+ \nu$. The reconstruction of the variable q^2 is discussed in section 4.6. In each figure, the distributions are shown with only the continuum and fake lepton subtracted (distribution (a)) and with all other background and crossfeed signals subtracted (distribution (b)). One can see a good agreement between the data and the fit results using the ISGW2 model.

5.3 Fit Quality

Figs. 5.10 through 5.12 show the residuals for the $B^+ \rightarrow \rho^0 e^+ \nu$, $B^0 \rightarrow \rho^- e^+ \nu$ and $B^+ \rightarrow \omega e^+ \nu$ modes in the HILEP and LOLEP regions. Good agreement between on-resonance data and fit result can be seen in each of these figures.

One can compute the total χ^2 and probability \mathcal{P} for this fit. The number of degrees of freedom N_{dof} is the number of bins with non-zero bin content, minus the number of free fit parameters. The χ^2 test is only reliable if the number of events in each bin is sufficiently large. In a paper of Cochran [43] it is argued that the number of entries per bin must be greater than six in at least 80% of all bins. To fulfill this criterion a somewhat coarser binning (larger bins in the regions of low statistics) before calculating a χ^2 is used. The χ^2 is defined by

$$\chi^2 = \sum_i \frac{(N_{on,i} - N_{fit,i})^2}{\sigma_i^2}, \quad (5.2)$$

where i runs over all bins, N_{on} is the number of on-resonance events in bin i and N_{fit} is the expected number of events in bin i , i.e. the sum of all contributions ($\sum_{j=1}^m p_j w_{ji} a_{ji}$,

see section 4.4.3). The error $\sigma_i = \sqrt{N_{on,i} + k^2 \cdot N_{off,i}}$ takes into account fluctuations in the on-resonance and off-resonance data sample. One finds

$$\begin{aligned}\chi^2 &= 91 , \\ N_{dof} &= 93 , \\ \mathcal{P} &= 0.52 ,\end{aligned}\tag{5.3}$$

and similar quality of the fits for the other four form-factor models.

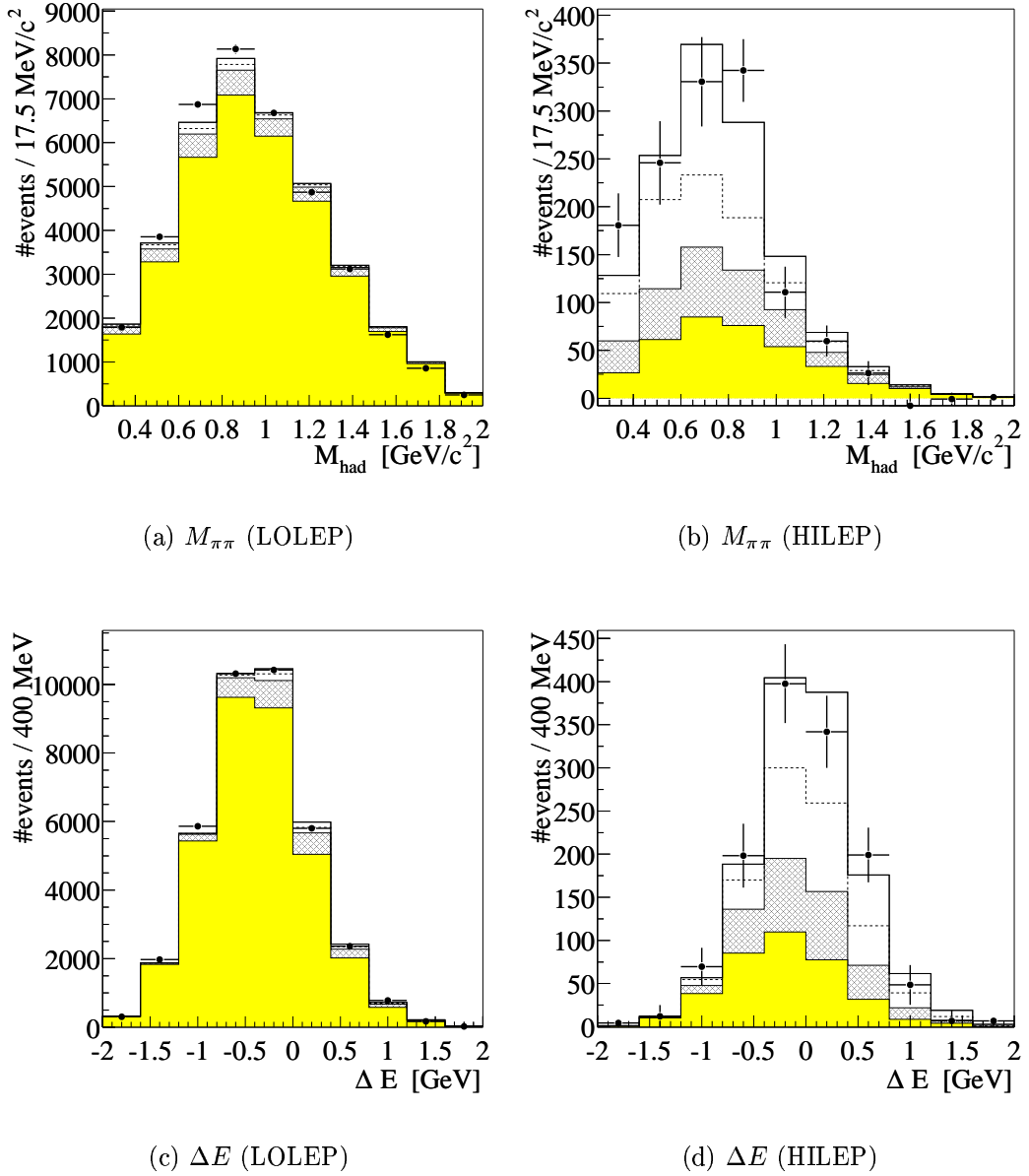


Figure 5.2: Projections of the ISGW2 fit result for the $B^+ \rightarrow \rho^0 e^+ \nu$ channel in the LOLEP and HILEP lepton-energy region; the contributions are the direct and crossfeed components of the signal (unshaded regions, above and below the dashed line, respectively); the background from $b \rightarrow ue\nu$ non-signal modes and $B \rightarrow \pi e\nu$ (double hatched region); the background from $b \rightarrow ce\nu$ and other backgrounds (lightly shaded region).

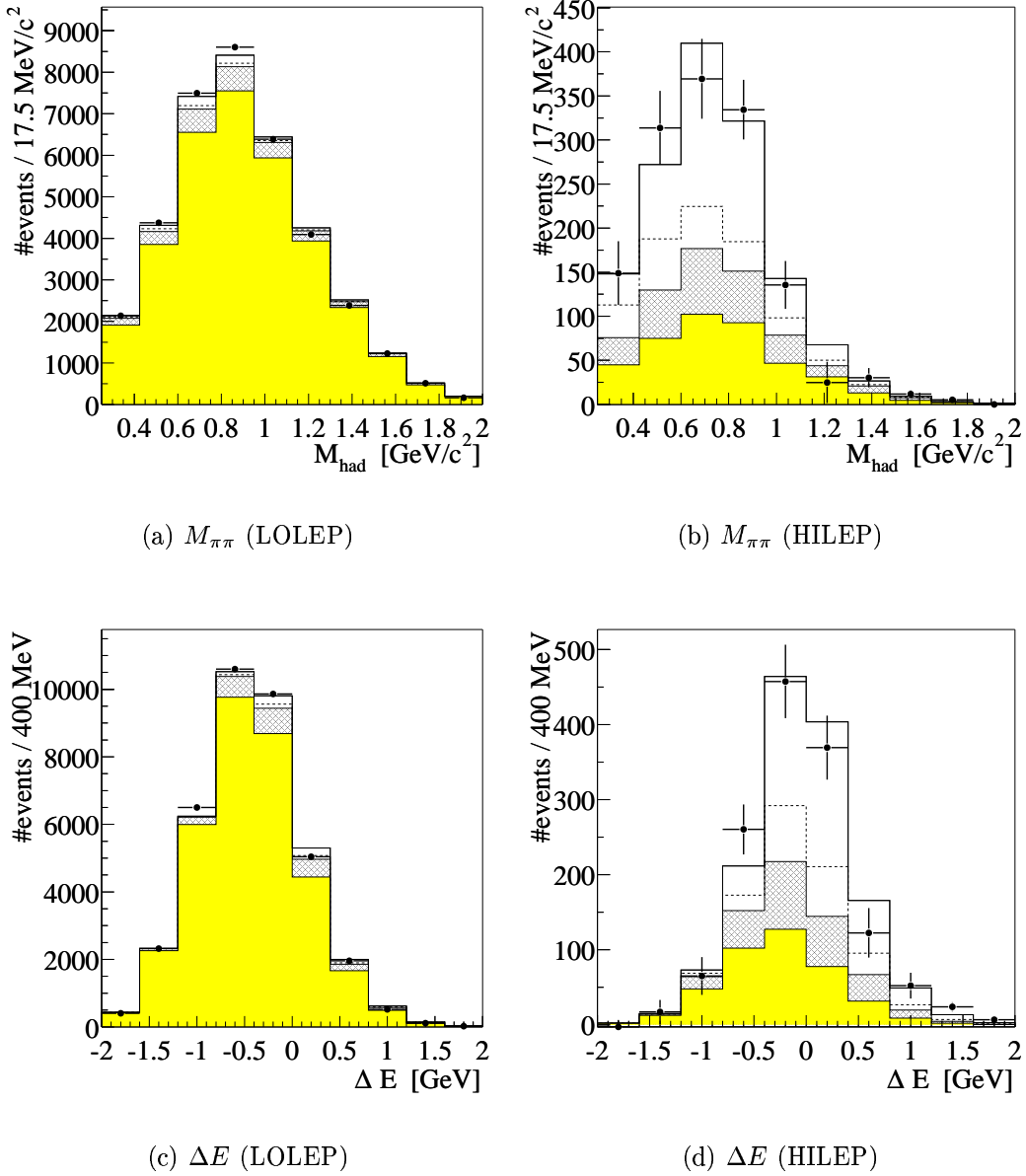


Figure 5.3: Projections of the ISGW2 fit result for the $B^0 \rightarrow \rho^- e^+ \nu$ channel in the LOLEP and HILEP lepton-energy region; the contributions are the direct and crossfeed components of the signal (unshaded regions, above and below the dashed line, respectively); the background from $b \rightarrow ue\nu$ non-signal modes and $B \rightarrow \pi e \nu$ (double hatched region); the background from $b \rightarrow ce\nu$ and other backgrounds (lightly shaded region).

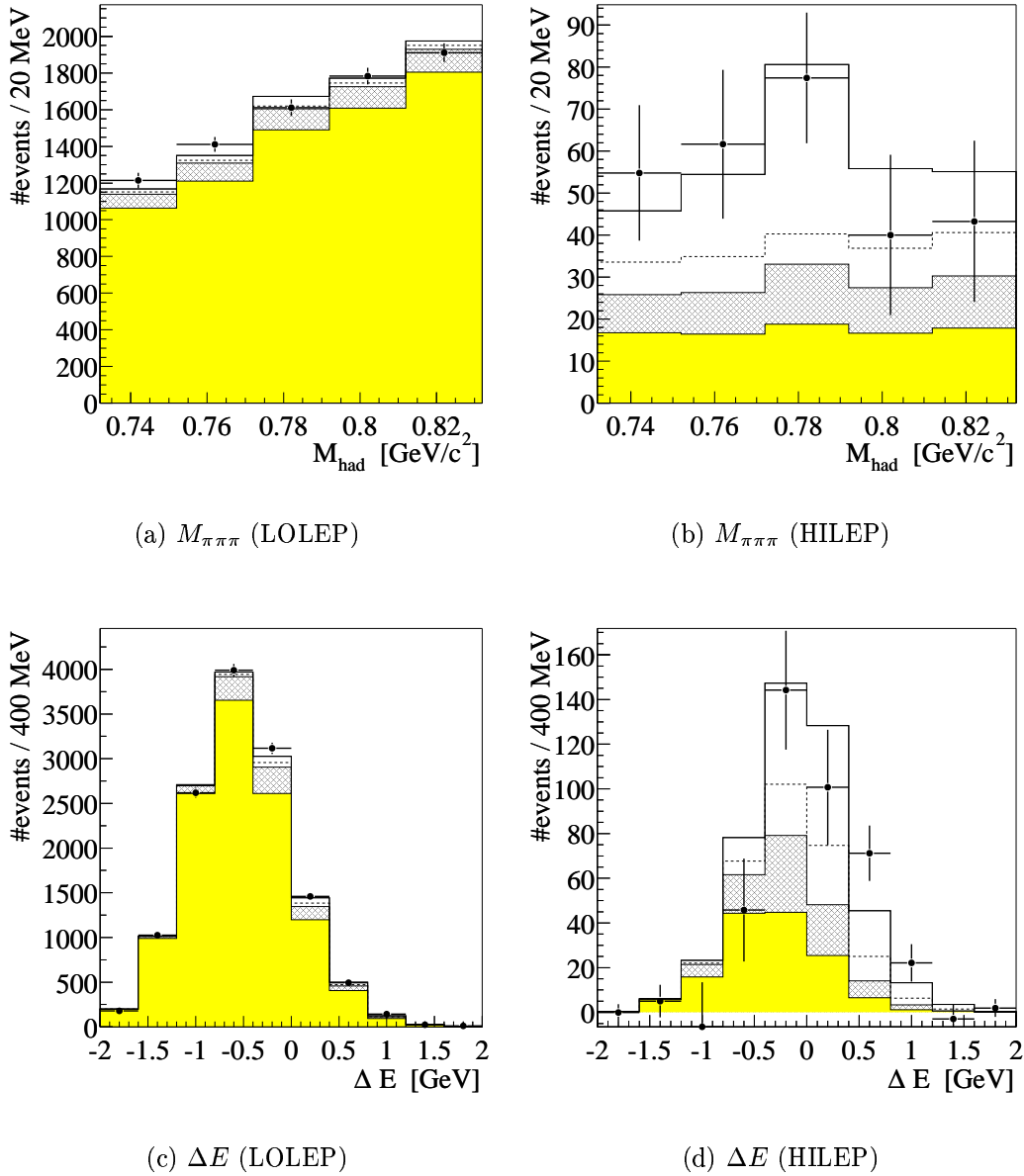


Figure 5.4: Projections of the ISGW2 fit result for the $B^+ \rightarrow \omega e^+ \nu$ channel in the LOLEP and HILEP lepton-energy region; the contributions are the direct and crossfeed components of the signal (unshaded regions, above and below the dashed line, respectively); the background from $b \rightarrow ue\nu$ non-signal modes and $B \rightarrow \pi e\nu$ (double hatched region); the background from $b \rightarrow ce\nu$ and other backgrounds (lightly shaded region).

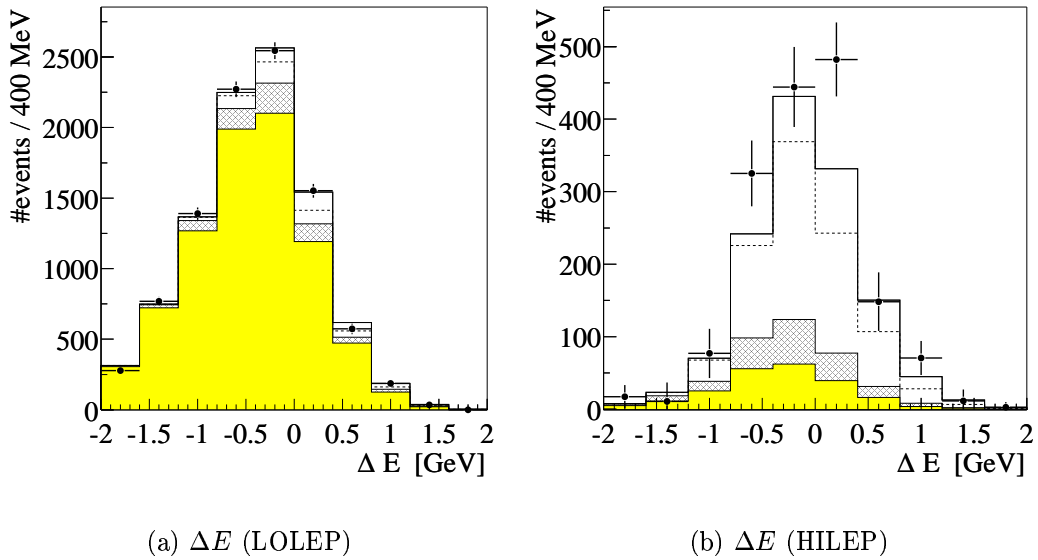


Figure 5.5: Projections of the ISGW2 fit result for the sum of the $B^+ \rightarrow \pi^0 e^+ \nu$ and $B^0 \rightarrow \pi^- e^+ \nu$ channels in the LOLEP and HILEP lepton-energy region; the contributions are the direct and crossfeed components of the signal (unshaded regions, above and below the dashed line, respectively); the background from $b \rightarrow ue\nu$ non-signal modes (double hatched region); the background from $b \rightarrow ce\nu$ and other backgrounds (lightly shaded region).

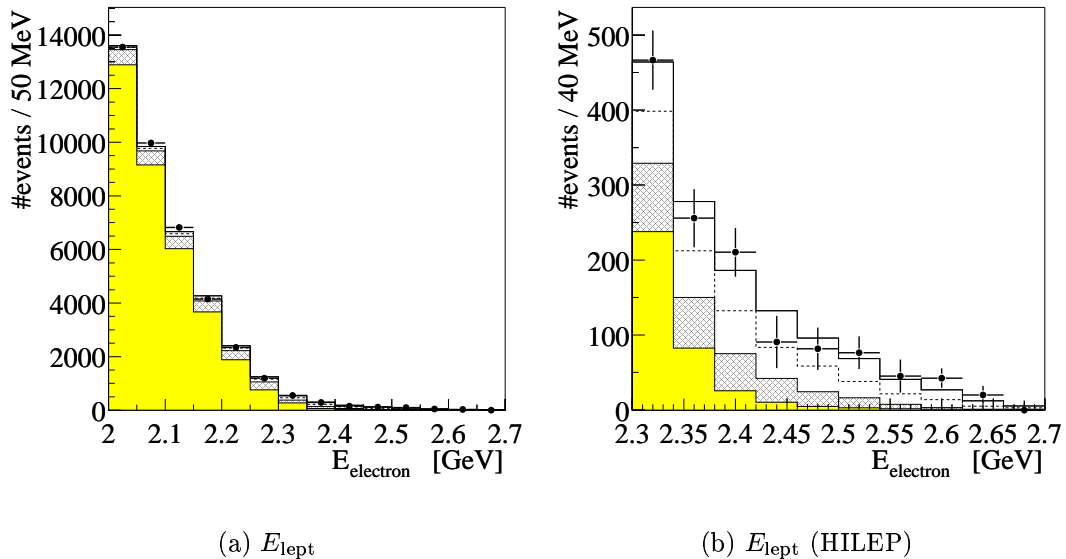


Figure 5.6: Projection of the kinematic variable E_{lept} for the mode $B^+ \rightarrow \rho^0 e^+ \nu$. The points with the error bars show the on-resonance data after continuum and fake subtractions. The histogram shows the projection of the ISGW2 fit. The contributions are the direct and crossfeed components of the signal (unshaded regions, above and below the dashed line, respectively); the background from $b \rightarrow ue\nu$ non-signal modes and $B \rightarrow \pi e\nu$ (double hatched region); the background from $b \rightarrow ce\nu$ and other backgrounds (lightly shaded region).

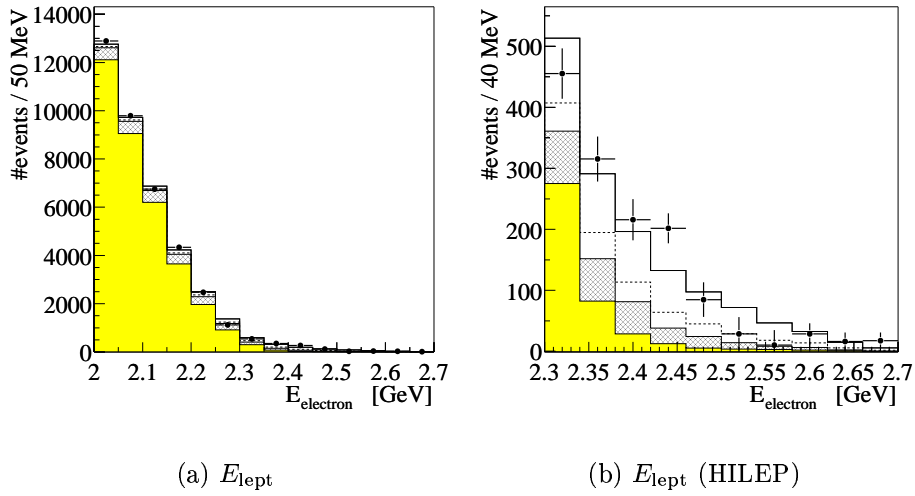


Figure 5.7: Projection of the kinematic variable E_{lept} for the mode $B^0 \rightarrow \rho^- e^+ \nu$. The points with the error bars show the on-resonance data after continuum and fake subtractions. The histogram shows the projection of the ISGW2 fit. The contributions are the direct and crossfeed components of the signal (unshaded regions, above and below the dashed line, respectively); the background from $b \rightarrow ue\nu$ non-signal modes and $B \rightarrow \pi e\nu$ (double hatched region); the background from $b \rightarrow ce\nu$ and other backgrounds (lightly shaded region).

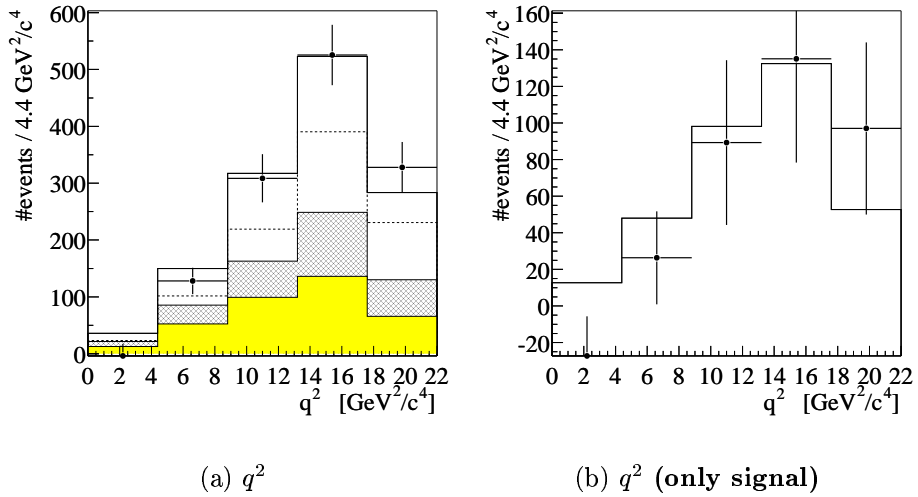


Figure 5.8: Projection of the kinematic variable q^2 for the modes $B^+ \rightarrow \rho^0 e^+ \nu$ (HILEP): (a) The points with the error bars show the on-resonance data after continuum and fake subtraction. The histogram shows the projection of the ISGW2 fit. The contributions are the direct and crossfeed components of the signal (unshaded regions, above and below the dashed line, respectively); the background from $b \rightarrow ue\nu$ non-signal modes and $B \rightarrow \pi e\nu$ (double hatched region); the background from $b \rightarrow ce\nu$ and other backgrounds (lightly shaded region). (b) The points with the error bars show the on-resonance data after subtraction of all backgrounds; the histogram shows the fitted $B^+ \rightarrow \rho^0 e^+ \nu$ signal.

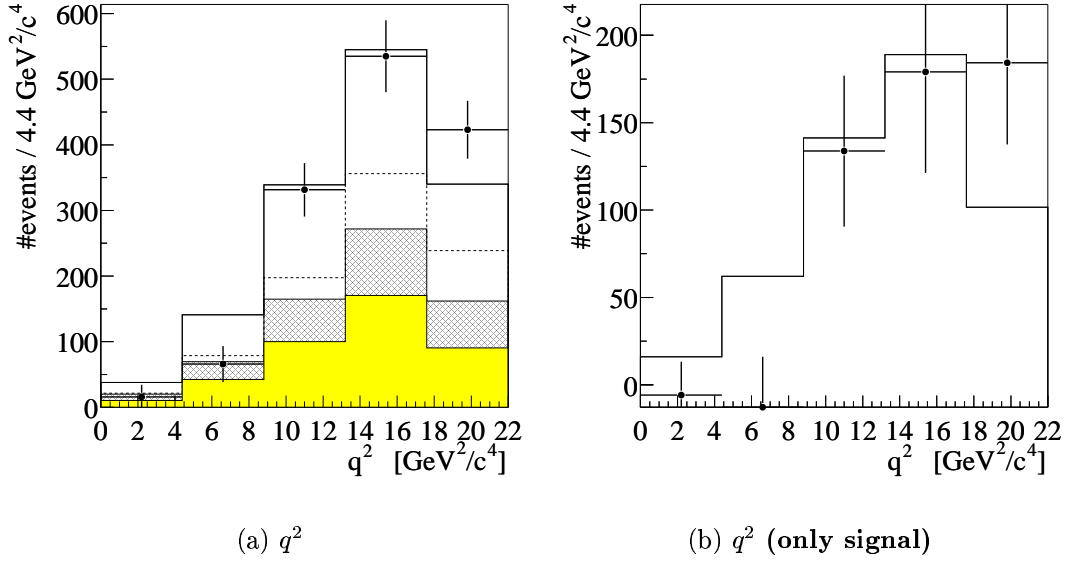


Figure 5.9: Projection of the kinematic variable q^2 for the modes $B^0 \rightarrow \rho^- e^+ \nu$ (HILEP): (a) The points with the error bars show the on-resonance data after continuum and fake subtraction. The histogram shows the projection of the ISGW2 fit. The contributions are the direct and crossfeed components of the signal (unshaded regions, above and below the dashed line, respectively); the background from $b \rightarrow ue\nu$ non-signal modes and $B \rightarrow \pi e\nu$ (double hatched region); from $b \rightarrow ce\nu$ and other backgrounds (lightly shaded region). (b) The points with the error bars show the on-resonance data after subtraction of all backgrounds; the histogram shows the fitted $B^0 \rightarrow \rho^- e^+ \nu$ signal.

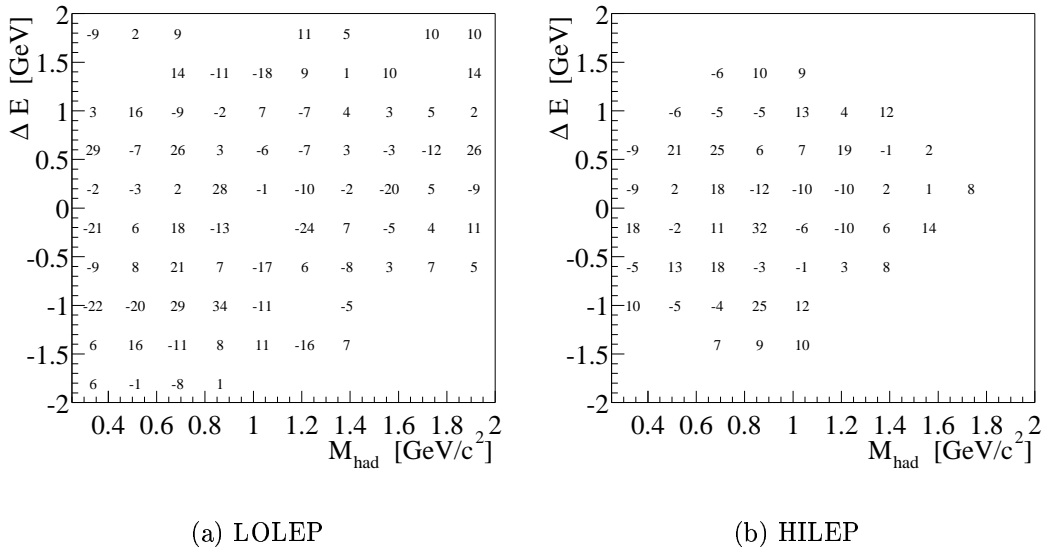


Figure 5.10: Residuals for the $B^+ \rightarrow \rho^0 e^+ \nu$ mode in the LOLEP and HILEP region. The residuals are defined, for each bin, as $10 \cdot (\text{data} - \text{fit}) / \sigma$, where σ is the $\sqrt{N_{on} + k^2 \cdot N_{off}}$ error due to the statistics of the on- and off-resonance data.

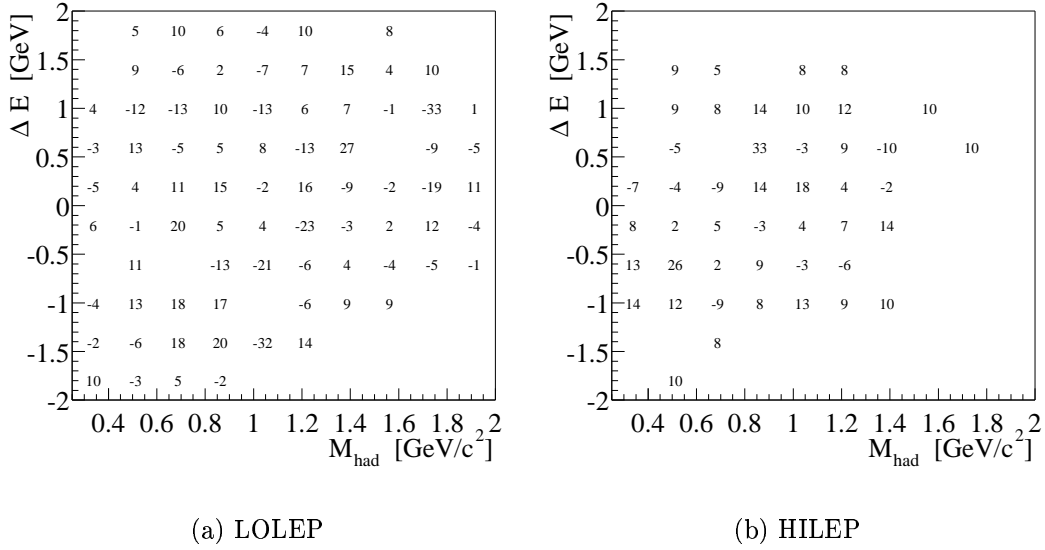


Figure 5.11: Residuals for the $B^0 \rightarrow \rho^- e^+ \nu$ mode in the LOLEP and HILEP region. The residuals are defined, for each bin, as $10 \cdot (\text{data} - \text{fit})/\sigma$, where σ is the $\sqrt{N_{on} + k^2 \cdot N_{off}}$ error due to the statistics of the on- and off-resonance data.

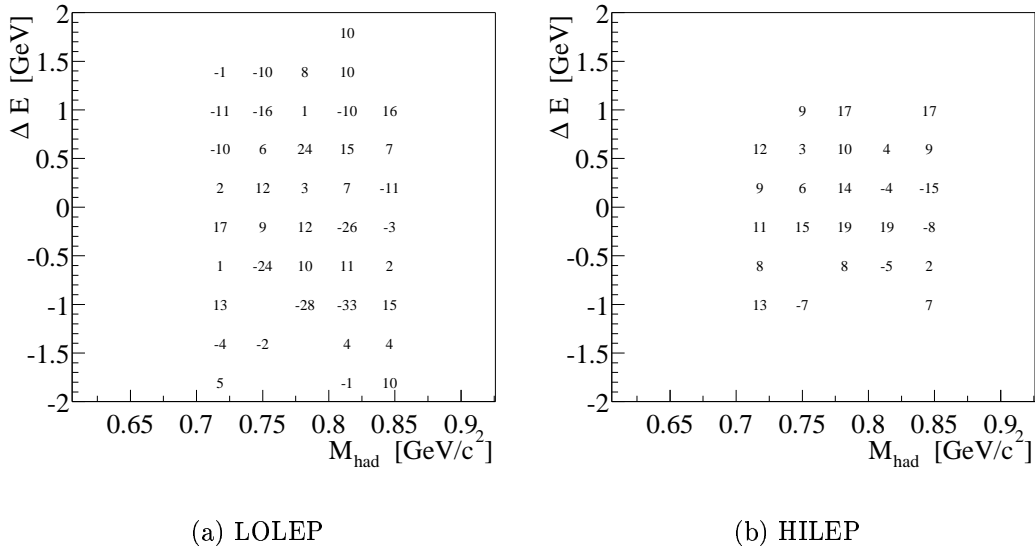


Figure 5.12: Residuals for the $B^+ \rightarrow \omega e^+ \nu$ mode in the LOLEP and HILEP region. The residuals are defined, for each bin, as $10 \cdot (\text{data} - \text{fit})/\sigma$, where σ is the $\sqrt{N_{on} + k^2 \cdot N_{off}}$ error due to the statistics of the on- and off-resonance data.

5.4 Systematic Errors

This chapter discusses all identified sources of systematic errors in this analysis. Errors arise from the detector simulation, from uncertainties in the background modeling, and other sources. Table 5.7 gives a summary of all systematic errors on the measured $B \rightarrow \rho l \nu$ branching fraction.

error contribution	$\delta\mathcal{B}_\rho/\mathcal{B}_\rho$ (%)
Tracking Efficiency	± 5
Tracking Resolution	± 1
Photon/ π^0 Efficiency	± 5
Photon/ π^0 Energy Scale	± 3
$b \rightarrow c$ Background Composition	$+1.4$ -1.7
$b \rightarrow u$ Background Composition	$+6$ -4
Non-Resonant $b \rightarrow u$	$\pm 9\%$
B Lifetime	± 1
B Counting	± 1.6
Fake Electrons	$< \pm 1$
Electron Id	± 2
f_\pm/f_{00}	$< \pm 1$
Data Selection	± 6
Fit Method	$+4$ -6
Total Systematic Error	± 15.5

Table 5.7: Summary of all contributions to the systematic error on the branching fraction.

5.4.1 Detector Simulation

This section discusses the effects of uncertainties in the tracking and photon efficiencies and resolutions. It is important to understand that the normalizations and shapes of the ΔE and other distributions depends not only on the reconstruction details of the signal tracks (the lepton and the pions) but also on the remaining particles in the event because these are used to reconstruct the missing momentum. It is crucial to understand the effect of tracking and photon efficiencies and other detector systematics.

Tracking Efficiency

A separate tracking efficiency study (for details see [34, 35, 36]) provides a relative MC/Data correction factor κ for each track as a function of the track's $|p|$, θ , ϕ and the event's track multiplicity. The effect of the tracking efficiency on the signal efficiency and the ΔE resolution is studied by killing all tracks randomly according to the correction factor κ . In the rare case that $\kappa > 1$ (i.e. data is more efficient than Monte Carlo simulation) tracks will be *reinserted* from the generator level applying a realistic smearing of the track parameters. When killing a track which is associated with a calorimeter cluster the cluster is kept but the track is eliminated. When inserting a track it is associated with a realistic energy deposition in the calorimeter and any clusters which

may have been associated with the corresponding truth particle are removed. Finally the systematic error is estimated by varying the tracking efficiencies globally by $\pm 1\%$. A variation of $\pm 5\%$ for the fitted branching fraction is observed. This is assigned as a systematic error for uncertainties in the tracking efficiency.

Tracking Resolution

To estimate the systematic uncertainty due to the tracking resolution an additional 15% smearing is applied to the ω helix fit parameter (which is proportional to the transverse momentum of a track) of all tracks in the Monte Carlo simulation. One finds a variation of -1% for the fitted branching fraction. A systematic error of $\pm 1\%$ is assigned for uncertainties in the tracking resolution.

Photon and π^0 Efficiencies

The π^0 efficiency has been determined from data using τ 1-on-1 decays [39]. This study shows that one must apply a 1.5% smearing of the Monte Carlo photon energies to better match the data. Several effects can contribute to a discrepancy between data and Monte Carlo simulation:

- lost or partly reconstructed clusters because of hardware inefficiencies,
- less dead material in the simulated than in the real detector leads to photons reconstructed at too low energies and π^0 masses which fall outside the π^0 mass window. Also more photons make a conversion pair and are not reconstructed as photon at all,
- a less than perfect calorimeter calibration also leading to invariant masses outside the mass window.

In case of single photons one would expect less efficiency discrepancies since there is no mass window cut and it is unlikely that a cluster is not reconstructed at all. Even if the photon converts it will contribute to the reconstruction of the missing momentum.

A systematic error is estimated by randomly removing a small fraction of π^0 mesons according to a momentum dependent function obtained in a separate study [38]. A 5% variation seen in the fit result is assigned as a systematic error for the photon and π^0 efficiency.

Photon and π^0 Energy Scale

When shifting all photon energies by 0.75% up and down, one finds a variation of $\pm 3\%$ for the fitted branching fraction. This is assigned as a systematic error for the calorimeter energy scale.

5.4.2 Background Modeling

The influence of the exact composition of the backgrounds is studied by varying the branching fraction for selected modes as described in the following paragraphs. Table 5.8 summarizes the results.

channel	variation	$\delta\mathcal{B}_\rho/\mathcal{B}_\rho$
$B \rightarrow D\ell\nu$	+10%	+0.5%
	-10%	-0.5%
$B \rightarrow D^*\ell\nu$	+10%	-1.6%
	-10%	+1.2%
other D channels	+40%	-0.5%
	-40%	+0.5%
$B \rightarrow \eta\ell\nu$	+50%	-2.4%
	-50%	+2.5%
$B \rightarrow a\ell\nu$	+50%	-2.0%
	-50%	+3.9%
$B \rightarrow b\ell\nu$	+50%	-2.1%
	-50%	+2.9%
$B \rightarrow h(f)\ell\nu$	+50%	-1.6%
	-50%	+2.3%

Table 5.8: Influence of the background composition on the fit result. $B \rightarrow D\ell\nu$ ($B \rightarrow D^*\ell\nu$) channels include B meson decays to charged and neutral D (D^*); $B \rightarrow \eta\ell\nu$ channels include B meson decays to η and η' ; $B \rightarrow a\ell\nu$ channels include B meson decays to a_0^0 , a_1^0 , a_0^\pm , a_1^\pm and a_2^\pm ; $B \rightarrow b\ell\nu$ channels include B meson decays to b_1^0 and b_1^\pm ; $B \rightarrow h(f)\ell\nu$ channels include decays to $f_0^{0(\prime)}$, $f_1^{0(\prime)}$, $f_2^{0(\prime)}$ and $h_1^{0(\prime)}$.

$b \rightarrow c$ Background Composition

The most important backgrounds arise from the well measured channels $B \rightarrow D\ell\nu$ and $B \rightarrow D^*\ell\nu$. The branching fraction is varied by $\pm 10\%$ for these two channels separately by assigning a weight to each event in such a manner that the total rate stays constant. Also the branching fraction of the other D channels was varied by $\pm 40\%$ in the same manner. The largest variation of the fit result is found when varying the D^* channel and is of the order -1.6% . The quadratic sum of all variations, ${}_{-1.7}^{+1.4}\%$, is taken as a contribution to the systematic error for the uncertainty in the $b \rightarrow c$ background composition.

$b \rightarrow u$ Background Composition

Similar to the $b \rightarrow c$ background, the branching fraction for selected channels is varied: $B \rightarrow X_u\ell\nu$, where $X_u = \eta, a, b, f(h)$. Again the weights are assigned in such a way that the total rate stays constant. Since the $b \rightarrow u$ background modes are less well measured than the $b \rightarrow c$ modes, these channels are varied by $\pm 50\%$. The largest variation of the fit result is found for the $B \rightarrow a\ell\nu$ channels and is of the order 3.9% . A systematic error

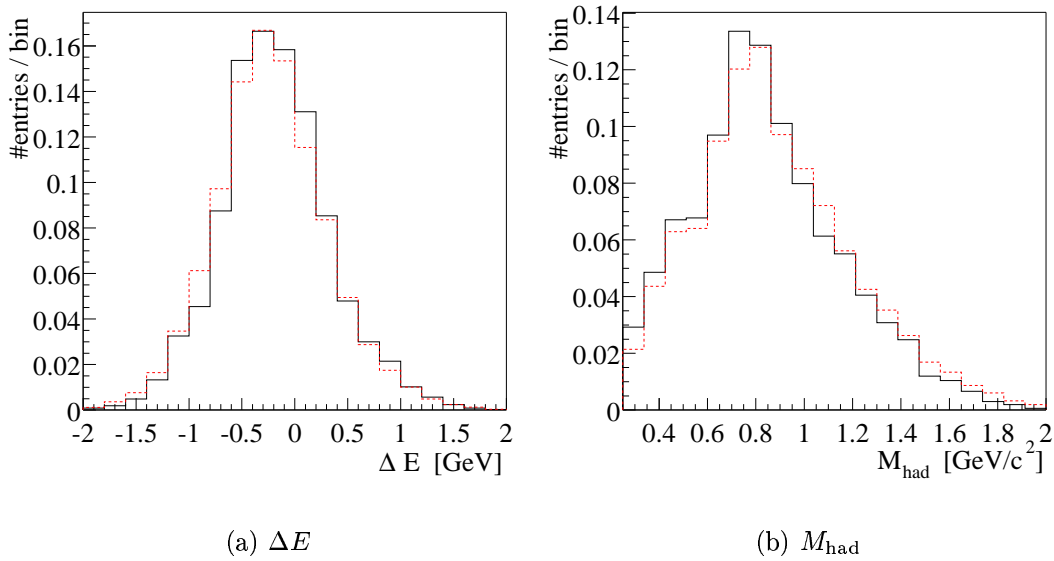


Figure 5.13: (a) ΔE and (b) M_{had} distribution of a purely resonant downfeed component (solid line) and a mix of resonant and non-resonant downfeed (dashed line). Non-resonant events are reconstructed with smaller values of ΔE , and greater values of M_{had} than resonant events, on average.

of ${}^{+6}_{-4}\%$, the quadratic sum of all variations, will be assigned for the uncertainty in the $b \rightarrow u$ background composition.

Non-Resonant $b \rightarrow u$ Backgrounds

Non-resonant $B \rightarrow \pi\pi\ell\nu$ contributions will peak at $\Delta E = 0$ in the same way as resonant contributions. However the hadron mass spectrum M_{had} and the q^2 distribution will be different. The spectra of $M_{\pi\pi}$ in Figs. 5.2 and 5.3 are completely compatible with the Breit-Wigner shape of the ρ . There is no strong indication of a non-resonant $B \rightarrow \pi\pi\ell\nu$ contribution. Another non-resonant background can arise from processes with more than two pions, for example $B \rightarrow \pi\pi\pi\ell\nu$. The Monte Carlo used to describe the $b \rightarrow u$ backgrounds includes a substantial fraction of these events (see Tables 4.3 and 4.4). The ΔE and M_{had} distributions for a purely resonant downfeed component and a mix of resonant and non-resonant decays is shown in Fig. 5.13. When doubling the non-resonant component and redoing the fit one finds a variation of +9%. However the fit parameters which describe the normalization of the $b \rightarrow u$ component in LOLEP are a few sigma away from the expectation, indicating that the downfeed component is not well described. Using a purely resonant mix to describe the $b \rightarrow u$ component one finds a variation of the fit result of -9%. Again the agreement of the downfeed component is worse. To cover any systematic uncertainties due to the shape of the downfeed component a systematic error of $\pm 9\%$ is assigned.

5.4.3 Other Systematic Errors

B Lifetime

The result of this analysis depends on the B meson lifetimes in two ways. On the one hand it is used to determine the relative number of $B^+ \rightarrow \rho^0 \ell^+ \nu$ and $B^+ \rightarrow \omega \ell^+ \nu$ to $B^0 \rightarrow \rho^- \ell^+ \nu$ events (the isospin constraint is used) and on the other hand the lifetime is needed to extract a value for $|V_{ub}|$. The PDG [22] value for B^0 and B^+ lifetimes is used, leading to an error of $\pm 1\%$.

B Counting

The method used to determine the number of B mesons has been described in section 4.1. The method yields a systematic error of $\pm 1.6\%$.

Fake Electrons

The fake lepton subtraction has been described in section 4.3.2. The misidentification rates are determined from data control samples. These are limited by the size and purity of these samples. The fake contribution is very small in the electron channels. A systematic error of 1% on the branching fraction from the normalization of the fake contribution is assigned. The analysis has been repeated with assuming that all electrons that do not pass the loose electron selection are pions. The pion control samples at high energies have larger statistics and less contamination than the kaon and proton control samples. One finds that the normalization of the fake contribution matches up to 20% compared to the case where different particle types are considered. The influence on the final result is $< 1\%$.

Electron Identification

The efficiencies of the electron selectors are determined from data and reproduced in Monte Carlo by using a killing technique (see section 4.2.1). There is however a systematic error due to the fact that the electron efficiencies are determined from (radiative) Bhabha events and not in a multihadron environment. Monte Carlo studies show that the absolute efficiency is known within $\pm 2\%$ [42].

f_{\pm}/f_{00}

The ratio of the number of $B^+ B^-$ to $B^0 \bar{B}^0$ events is known to better than 10% [22]. The effect on the fitted branching fraction will be much smaller since the fit conserves the number of $B^+ \rightarrow \rho^0 \ell^+ \nu$ plus $B^0 \rightarrow \rho^- \ell^+ \nu$ events rather than each number individually. Varying the ratio within the experimental errors one finds a variation of less than 1% for the fitted branching fraction.

cut variation	$\delta\mathcal{B}_\rho/\mathcal{B}_\rho$
$ \cos(\theta_{\text{miss}}) < 0.85$	+11%
$ \cos(\theta_{\text{miss}}) < 0.95$	-6%
$\mathcal{O}_{\text{net}} < 0.55$	-11%
$\mathcal{O}_{\text{net}} < 0.65$	+6%
$\cos \Delta\theta_{\text{min}} > 0.75$	+1%
$\cos \Delta\theta_{\text{min}} > 0.85$	+9%
$ \cos(\theta_{BY}) < 1.05$	-0.3%
$ \cos(\theta_{BY}) < 1.15$	-3.0%

Table 5.9: Relative change of the fitted branching fraction for different cut variations.

Data Selection

The most important cuts have been varied to study the behaviour of the fit result. Variations of the fit result are expected for several reasons. On the one hand the amount of data used in the fit changes. Note that the statistics of the off-resonance component is very low, and even small changes can introduce noticeable variations in the shape of the off-resonance distributions. This kind of error is already accounted for by the statistical error of the fit result. On the other hand the Monte Carlo simulation may not exactly match the data. These systematic uncertainties are partly caused by theoretical form-factor model uncertainties, which are in turn already covered by the theoretical error quoted on the fit result.

Fit results for various cut variations are shown in Table 5.9. The largest variation of $\pm 11\%$ is seen when changing the $|\cos(\theta_{\text{miss}})|$ and \mathcal{O}_{net} requirements. Here the amount of continuum used in the fit changes rather drastically by 20% and 37% respectively. A toy Monte Carlo study shows that the variation of the fit result expected due to purely statistical fluctuations is of order $\pm 6\%$ for the variation of the neural net cut and $\pm 5\%$ for the $|\cos(\theta_{\text{miss}})|$ cut. Since the actual variation seen is somewhat larger, an additional systematic error of $\pm 6\%$, corresponding to half the full spread seen, is assigned for uncertainties in the data selection.

Fit Method

The fit has been repeated with various modifications, without the ω or π modes, without the lepton-energy region LOLEP, and with different binnings. Table 5.10 shows the branching fractions $\mathcal{B}(B^0 \rightarrow \rho^- e^+ \nu)$ that have been determined using these settings. Note that in the case of fitting without the LOLEP region, the $b \rightarrow c$ fit parameters need to be fixed, otherwise the fit cannot determine the normalization of the $b \rightarrow c$ backgrounds. For this reason the quoted statistical error in this case is smaller than for the other fit results. The largest variations seen are +8% and -12%. Note that a large part of the variation originates in statistical fluctuations and is covered by the statistical error of the fit result. In case of the fit without the ω mode, a toy Monte Carlo shows that the expected variation due to statistical fluctuations is 5%, which is compatible with the variation seen. In case of the fit without the LOLEP region one will be very sensitive to the exact shape of the lepton-energy spectrum. The variation of -12% for

fit method:	$\mathcal{B}(B^0 \rightarrow \rho^- \ell^+ \nu)$	$\delta \mathcal{B}_\rho / \mathcal{B}_\rho$
(a) default fit	$(2.79 \pm 0.35) \cdot 10^{-4}$	
(b) without ω mode	$(2.62 \pm 0.38) \cdot 10^{-4}$	-6%
(c) without π modes	$(2.60 \pm 0.33) \cdot 10^{-4}$	-7%
(d) without LOLEP	$(2.48 \pm 0.40) \cdot 10^{-4}$	-12%
(e) 5×5 bins in $(M(\pi\pi), \Delta E)$	$(3.01 \pm 0.39) \cdot 10^{-4}$	+8%
(f) 15×15 bins in $(M(\pi\pi), \Delta E)$	$(2.71 \pm 0.34) \cdot 10^{-4}$	-3%

Table 5.10: Result of the fit using the method describe in section 5 with different settings: (a) default; (b) without fitting the ω channel; (c) without fitting the π channels; (d) without fitting the LOLEP region; (e) data are divided in 5 bins over the $0.25 \leq M_{\text{had}} \leq 2 \text{ GeV}/c^2$ region and 5 bins over the $|\Delta E| \leq 2 \text{ GeV}$ region (f) data are divided in 15 bins over the $0.25 \leq M_{\text{had}} \leq 2 \text{ GeV}/c^2$ region and 15 bins over the $|\Delta E| \leq 2 \text{ GeV}$ region.

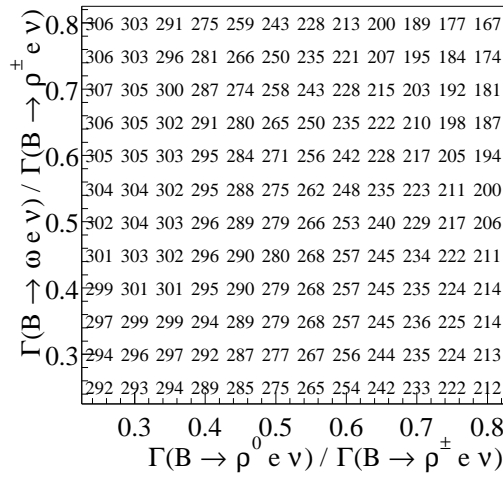


Figure 5.14: $B^0 \rightarrow \rho^- \ell^+ \nu$ branching fraction as function of $\Gamma(B^+ \rightarrow \rho^0 \ell^+ \nu) / \Gamma(B^0 \rightarrow \rho^- \ell^+ \nu)$ and $\Gamma(B^+ \rightarrow \omega \ell^+ \nu) / \Gamma(B^0 \rightarrow \rho^- \ell^+ \nu)$. The nominal fit is performed using the constraints $\Gamma(B^+ \rightarrow \rho^0 \ell^+ \nu) / \Gamma(B^0 \rightarrow \rho^- \ell^+ \nu) = \Gamma(B^+ \rightarrow \omega \ell^+ \nu) / \Gamma(B^0 \rightarrow \rho^- \ell^+ \nu) = 0.5$.

the ISGW2 model can partly be understood if the actual lepton energy spectrum is softer than for the ISGW2 model. The ISGW2 model has the hardest lepton-energy spectrum of all models studied here. The corresponding variation seen for the other models is smaller and ranges from 8 to 11%. All other fit variations are similar for all models.

Since some of the variations seen are somewhat larger than the expected statistical fluctuations, half of the maximum spread, ${}_{-6}^{+4}\%$, is taken as an estimate for an additional systematic error of the fit method.

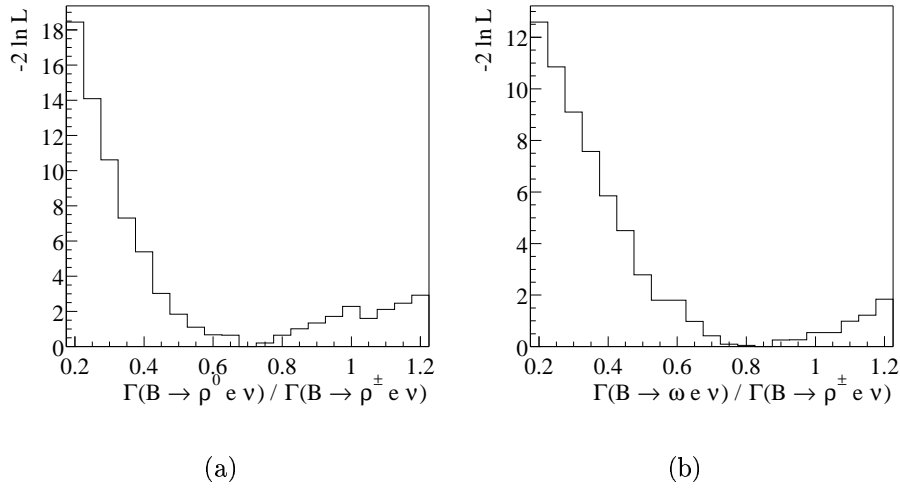


Figure 5.15: $-2 \ln \mathcal{L}$ as function of **(a)** $\Gamma(B^+ \rightarrow \rho^0 \ell^+ \nu) / \Gamma(B^0 \rightarrow \rho^- \ell^+ \nu)$ and **(b)** $\Gamma(B^+ \rightarrow \omega \ell^+ \nu) / \Gamma(B^0 \rightarrow \rho^- \ell^+ \nu)$. The nominal fit uses the constraints $\Gamma(B^+ \rightarrow \rho^0 \ell^+ \nu) / \Gamma(B^0 \rightarrow \rho^- \ell^+ \nu) = \Gamma(B^+ \rightarrow \omega \ell^+ \nu) / \Gamma(B^0 \rightarrow \rho^- \ell^+ \nu) = 0.5$.

Isospin Constraints

The following isospin relations have been used in the fit to constrain the relative normalizations of $B^0 \rightarrow \rho^- e^+ \nu$, $B^+ \rightarrow \rho^0 e^+ \nu$, and $B^+ \rightarrow \omega e^+ \nu$ (Eq. 4.21):

$$\begin{aligned} \Gamma(B^0 \rightarrow \rho^- \ell^+ \nu) &= 2 \Gamma(B^+ \rightarrow \rho^0 \ell^+ \nu) , \\ \Gamma(B^+ \rightarrow \rho^0 \ell^+ \nu) &= \Gamma(B^+ \rightarrow \omega \ell^+ \nu) . \end{aligned} \quad (5.4)$$

G. López Castro *et al.* have predicted large isospin breaking effects of about 30% in $B \rightarrow \rho \ell \nu$ due to $\rho - \omega$ mixing [44]. These predictions would imply

$$\Gamma(B^+ \rightarrow \rho^0 \ell^+ \nu) / \Gamma(B^0 \rightarrow \rho^- \ell^+ \nu) = 0.67 , \text{ and} \quad (5.5)$$

$$\Gamma(B^+ \rightarrow \omega \ell^+ \nu) / \Gamma(B^0 \rightarrow \rho^- \ell^+ \nu) = 0.51 . \quad (5.6)$$

Fig. 5.14 shows the fitted branching fraction of $B^0 \rightarrow \rho^- e^+ \nu$ as a function of $\Gamma(B^+ \rightarrow \rho^0 \ell^+ \nu) / \Gamma(B^0 \rightarrow \rho^- \ell^+ \nu)$ and $\Gamma(B^+ \rightarrow \omega \ell^+ \nu) / \Gamma(B^0 \rightarrow \rho^- \ell^+ \nu)$. If the predictions hold the fitted branching fraction would change by 16%. However it was shown in [11], that when taking into account the finite ρ and ω width (using the proper Breit-Wigner function) the isospin breaking effect is only of the order 3%.

To experimentally test the isospin constraints, one can evaluate the fit quality as a function of $\Gamma(B^+ \rightarrow \rho^0 \ell^+ \nu) / \Gamma(B^0 \rightarrow \rho^- \ell^+ \nu)$ and $\Gamma(B^+ \rightarrow \omega \ell^+ \nu) / \Gamma(B^0 \rightarrow \rho^- \ell^+ \nu)$, see Fig. 5.15. The minimum of $-2 \log \mathcal{L}$ occurs at $\Gamma(B^+ \rightarrow \rho^0 \ell^+ \nu) / \Gamma(B^0 \rightarrow \rho^- \ell^+ \nu) \simeq 0.7$ and $\Gamma(B^+ \rightarrow \omega \ell^+ \nu) / \Gamma(B^0 \rightarrow \rho^- \ell^+ \nu) \simeq 0.75$. These results are in agreement with equations 5.4 within 1.3σ and 1.7σ .

Considering that experimentally there is no significant evidence of isospin breaking, and that a realistic violation of order 3% would have a negligible influence on the fit result, no systematic error will be included for a possible isospin breaking.

5.5 Extraction of $|V_{ub}|$

The CKM matrix element $|V_{ub}|$ can be obtained from the branching fraction $\mathcal{B}(B^0 \rightarrow \rho^- \ell^+ \nu)$ using the relation

$$|V_{ub}| = \sqrt{\frac{\mathcal{B}(B^0 \rightarrow \rho^- \ell^+ \nu)}{\tilde{\Gamma}_{thy} \tau_{B^0}}}, \quad (5.7)$$

where $\tau_{B^0} = 1.548 \pm 0.032$ ps is used [22]. A combined central value is determined by taking the mean of all form-factor results, weighted by the individual theoretical error of each model. The branching fractions are taken separately for each form-factor as listed in Fig. 5.1. $\tilde{\Gamma}_{thy}$ and its theoretical error for each form-factor model is given in Table 2.3. The calculations quote errors on $\tilde{\Gamma}_{thy}$ between 15% and 50%. The statistical and systematic errors of the final combined result are determined by taking the mean of the relative errors of each individual result. The theoretical error is taken to be one half of the full spread of all fit results (including theoretical errors). The results for each form-factor and the combined result are shown in Fig. 5.16. The combined result is

$$|V_{ub}| = (3.69 \pm 0.23 \pm 0.27_{-0.59}^{+0.40}) \times 10^{-3}, \quad (5.8)$$

where the errors are statistical (including Monte Carlo statistics), systematic, and theoretical respectively. The largest uncertainty on $|V_{ub}|$ arises from the normalization $\tilde{\Gamma}_{thy}$ of the models.

5.6 Comparison with Other Measurements

A comparison of the result with inclusive [32] and exclusive measurements from CLEO and the inclusive measurement from LEP [30] is shown in Fig. 5.17. Two exclusive results from CLEO are quoted. The first result is obtained from an analysis very similar to the analysis presented here [11], the second result is an average of the first result and another separate analysis [10, 11]. The result presented here shows competitive errors, is compatible with all other measurements within errors, and lies inbetween the CLEO and LEP results.

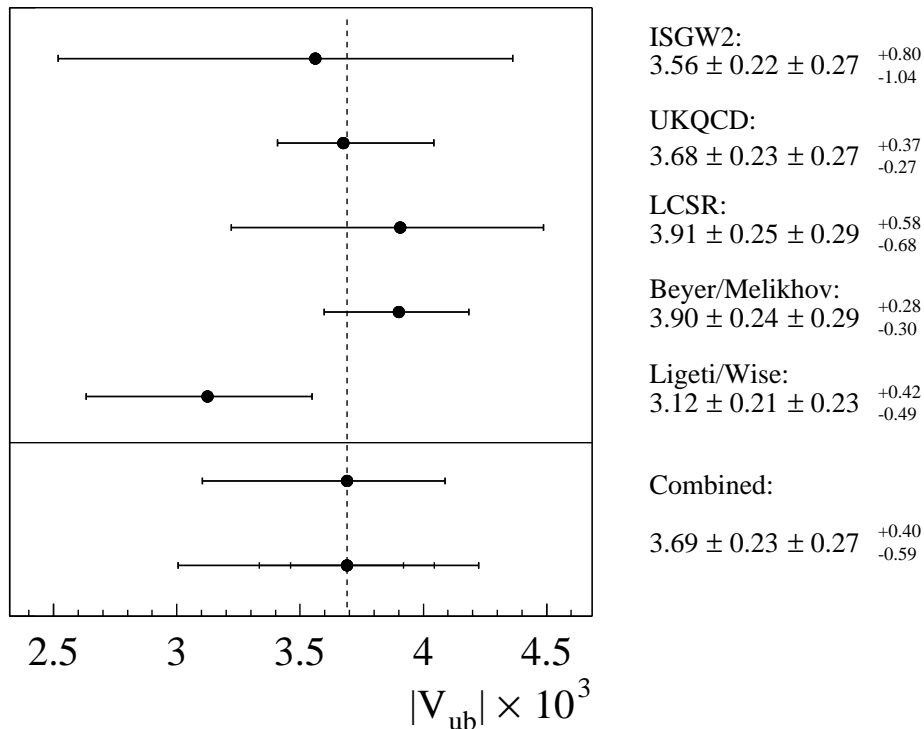


Figure 5.16: $|V_{ub}|$ determined using the ISGW2, UKQCD, LCSR, Beyer/Melikhov, and Ligeti/Wise form-factors. The results for each form-factor are drawn with theoretical error bars only. The combined central value is determined by taking the mean of all form-factor results, weighted by their individual theoretical error. The theoretical error of the combined result is taken to be one half of the full spread of results, including the errors. The combined result is also drawn with statistical, systematic, and theoretical errors successively added in quadrature. The statistical and systematic errors of the combined result are determined by taking the mean of the relative errors of each individual result. All five results are shown on the right side of the figure separately with their statistical, systematic, and theoretical errors.

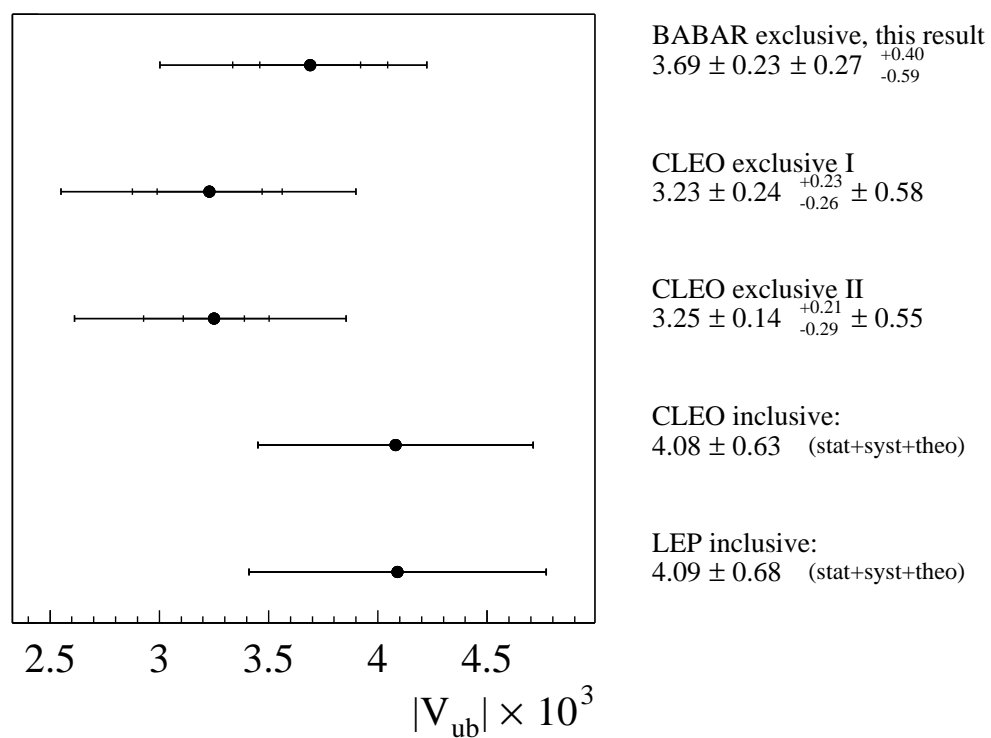


Figure 5.17: Comparison with results from other experiments. The exclusive CLEO result I [11] is obtained from an analysis very similar to the analysis presented here, the result II is an average of the result I and a separate CLEO result [10].

Chapter 6

Conclusions and Outlook

A measurement of the branching fraction $B \rightarrow \rho \ell \nu$ and the CKM matrix element $|V_{ub}|$ was presented. The results obtained show competitive errors compared to other analyses. The dominating systematic error comes from uncertainties in the downfeed background from resonant and non-resonant semileptonic decays other than the signal modes. The statistical error is smaller than for any other single exclusive previous measurement. The results are well compatible with constraints from the Standard Model and with other measurements.

A more stringent test of the Standard Model will be possible in the future assuming theoretical advances in the field of form-factor models and improvements in the experimental techniques. There have not been many new theoretical results during the last few years. Nevertheless one can expect future improvements in the calculation of form-factors especially from enhanced lattice QCD calculations.

Although this measurement was limited by the systematic and theoretical errors, there are several options for experimental improvements when a larger dataset becomes available. The most important one being the improvement of the neutrino reconstruction. With a better neutrino resolution the signal to background ratio can be enhanced, suppressing more continuum, downfeed and most importantly downfeed from non-resonant modes. This will allow to reduce the systematic uncertainties substantially. Also it should be possible to include a larger fraction of the lepton-energy spectrum, thus reducing model dependencies. The inclusion of lepton energies between 1 and 2 GeV may even allow to distinguish between form-factor models in the long term future. There is no clear signal yet in the semileptonic omega channel, but with somewhat increased data statistics and enhancements to the omega signal to background ratio, maybe by designing a dedicated neural net or fisher discriminant, the omega channel seems to be a promising mode for further studies.

The initial goal of the *BABAR* experiment was the measurement of the CP violation parameter $\sin 2\beta$. The latest result presented by the *BABAR* collaboration quotes a value of $\sin 2\beta = 0.75 \pm 0.09 \pm 0.04$ [45] and is therefore compatible with Standard Model expectations. Together with a similar result published by the Belle collaboration at about the same time [46] one can already conclude that no large violation of the Standard

Model expectation for CP violation in the interference of mixing and decay is observed. The focus of the *BABAR* experiment will naturally shift towards other measurements, including non CP-violating processes. One of them is the measurement of the exclusive branching fraction $B \rightarrow \rho \ell \nu$ presented in this thesis. A precise measurement of the CKM matrix element $|V_{ub}|$ derived from this and other analyses provides an excellent consistency check of the CKM picture in the Standard Model.

List of Tables

2.1	Quantum numbers of quarks and leptons	6
2.2	Lepton-energy distribution for different form-factor models	11
2.3	Predicted values of $\tilde{\Gamma}_{thy}$ for different form-factor models.	11
2.4	Values for the parameters $F(0)$, a , and b in the LCSR model	17
2.5	Values for the parameters $f(0)$, a , and b in the Beyer/Melikhov model	18
4.1	Summary of all data runs used in this analysis	28
4.2	Summary of all Monte Carlo samples used in this analysis	29
4.3	$B^0 \rightarrow H_u \ell \nu$ decay modes	30
4.4	$B^\pm \rightarrow H_u \ell \nu$ decay modes	30
4.5	Decay modes of the a mesons	31
4.6	Decay modes of the f mesons	31
4.7	Decay modes of the b , h and η mesons	32
4.8	Measured $b \rightarrow ul\nu$ branching fraction in different experiments	32
4.9	Branching fraction for the semileptonic $b \rightarrow c$ background modes.	33
4.10	Fractions of particles with respect to the total number of tracks that are not electrons.	37
4.11	Number of fake electrons	38
4.12	Selection efficiencies for the electron channels	51
4.13	Selection efficiencies for continuum events	51
4.14	LOLEP selection efficiencies for the vector modes	52
4.15	HILEP selection efficiencies for the vector modes	53
4.16	Total number of off-resonance events $A_{i,off}$ given by the fit.	58
4.17	Fit parameters	59
5.1	Signal efficiencies	66
5.2	Fitted yields of the $B^+ \rightarrow \rho^0 e^+ \nu$ mode	67
5.3	Fitted yields of $B^+ \rightarrow \rho^0 e^+ \nu$ mode	67
5.4	Fitted yields of the $B^+ \rightarrow \omega e^+ \nu$ mode	68

5.5	Result of the binned likelihood fit	68
5.6	Correlations between the 9 fit parameters.	69
5.7	Summary of all systematic errors	78
5.8	Influence of the background composition on the fit result	80
5.9	Cut Variations	83
5.10	Fit methods	84

List of Figures

2.1	The unitarity triangle	9
2.2	Spectator diagram of $B^0 \rightarrow \rho^- \ell^+ \nu$	10
2.3	$d\Gamma/dq^2$ distribution for different form-factor models	12
2.4	Dalitz plots for $B \rightarrow \rho(\pi)\ell\nu$	12
2.5	Angles $\theta_\ell, \theta_V, \chi$	14
2.6	Kinematic distributions of the form-factor models.	15
3.1	Schematic view of the <i>BABAR</i> detector.	20
3.2	Schematic view of the acceleration and storage system of PEP-II.	21
3.3	Schematic view of the silicon vertex tracker, SVT	21
3.4	Schematic xz-view of the drift chamber DCH	22
3.5	Schematic view of the Cherenkov detector, DIRC.	23
3.6	Working principle of the DIRC	24
3.7	Schematic view of the electromagnetic calorimeter, EMC.	24
3.8	Electron efficiency and pion misidentification rate.	25
3.9	Schematic view of the instrumented flux return, IFR.	26
4.1	\mathcal{R}_2 distribution	35
4.2	Fake electrons for the vector meson modes	37
4.3	$\gamma\gamma$ invariant mass	39
4.4	Missing momentum resolution	40
4.5	$\cos\theta_{\text{miss}}$ distribution	41
4.6	Angles θ_{BY} and $\Delta\theta$ defined in the $\Upsilon(4S)$ frame.	42
4.7	$\cos\theta_{BY}$ distribution	43
4.8	$\cos\Delta\theta_{\text{min}}$ distribution	43
4.9	$ \vec{p}_{\text{had}} + \vec{p}_\ell + \vec{p}_{\text{miss}} $ distribution	45
4.10	Comparison of the neural net variables for data and Monte Carlo simulation	46
4.11	Comparison of the energy flow distributions for data and Monte Carlo simulation	47

4.12	Neural net output for signal and background contributions	48
4.13	Comparison of the neural net output for data and Monte Carlo simulation	48
4.14	Cut Optimization	50
4.15	$M(\pi\pi)$ vs ΔE of various contributions to the fit.	54
4.16	$M(\pi\pi)$ vs ΔE for on- and off-resonance data	55
4.17	Fitted branching fraction for 10000 toy Monte Carlo samples	60
4.18	Reweighted kinematic distributions	62
4.19	q^2 resolution	63
5.1	$B^0 \rightarrow \rho^- e^+ \nu$ branching fraction for different form-factors	66
5.2	Projections of the fit result for the mode $B^+ \rightarrow \rho^0 e^+ \nu$	71
5.3	Projections of the fit result for the mode $B^0 \rightarrow \rho^- e^+ \nu$	72
5.4	Projections of the fit result for the mode $B^+ \rightarrow \omega e^+ \nu$	73
5.5	Projections of the fit result for the modes $B \rightarrow \pi e \nu$	74
5.6	Projection of the kinematic variable E_{lept} for the mode $B^+ \rightarrow \rho^0 e^+ \nu$. .	74
5.7	Projection of the kinematic variable E_{lept} for the mode $B^0 \rightarrow \rho^- e^+ \nu$. .	75
5.8	Projection of the kinematic variable q^2 for the mode $B^+ \rightarrow \rho^0 \ell^+ \nu$	75
5.9	Projection of the kinematic variable q^2 for the mode $B^0 \rightarrow \rho^- \ell^+ \nu$	76
5.10	Fit residuals for the mode $B^+ \rightarrow \rho^0 \ell^+ \nu$	76
5.11	Fit residuals for the mode $B^0 \rightarrow \rho^- e^+ \nu$	77
5.12	Fit residuals for the mode $B^+ \rightarrow \omega \ell^+ \nu$	77
5.13	ΔE and M_{had} distribution of the resonant and non-resonant downfeed . .	81
5.14	Fit results assuming isospin breaking	84
5.15	$-2 \ln \mathcal{L}$ assuming isospin breaking	85
5.16	$ V_{ub} $ for different form-factors	87
5.17	Comparison with results from other experiments.	88

Bibliography

- [1] Super-Kamiokande Collaboration, *Phys. Rev. Lett.* 81 (1998).
- [2] SNO Collaboration, *Phys. Rev. Lett.* 87, 071301 (2001).
- [3] H. Georgi, Helen R. Quinn, S. Weinberg, *Phys. Rev. Lett.* 33:451-454,1974.
- [4] P. Higgs, *Phys. Lett.* 12:132-133 (1964)
- [5] M.Kobayashi and T. Maskawa, *Prog. Theor. Phys.* 49, 652 (1973).
- [6] L. Wolfenstein, *Phys. Rev. Lett.* **51**, 1945 (1983)
- [7] R.M. Barnett *et al.*, *Phys. Rev.* **D54**,1 (1996)
- [8] The *BABAR* Physics Book, Physics at an Asymmetric *B* Factory, P.F. Harrison and H.R. Quinn, SLAC-R-504 (1998)
- [9] J.D. Richman and P.R. Burchat, *Rev. Mod. Phys.* **67**, 893 (1995).
- [10] J.P. Alexander *et al.*, *Phys. Rev. Lett.* **77**, 5000 (1996)
- [11] CLEO Collaboration (B.H. Behrens *et al.*), *Phys. Rev.* **D61**, 052001 (2000)
- [12] N. Isgur, D. Scora, B. Grinstein, and M. B. Wise, *Phys. Rev.* **D39**, 799 (1989).
- [13] N. Isgur and D. Scora, *Phys. Rev.* **D52** 2783 (1995).
- [14] L. Del Debbio *et al.*, *Phys. Lett.* **B416**, 392 (1998).
- [15] B. Stech, *Phys. Lett.* **B354** 447 (1995), hep-ph/9502378
- [16] P. Ball and V. M. Braun, *Phys. Rev.* **D58**, 094016 (1998).
- [17] M. A. Shifman, A. I. Vainshtein and V. I. Zakharov, *Nucl. Phys.* **B147** 385; 448; 519 (1979)
- [18] S. J. Brodsky and G. P. Lepage, *Perturbative Quantum Chromodynamics*, p. 93, World Scientific, Singapore (1989)
- [19] M. Beyer and D. Melikhov, *Phys. Lett.* **B436** 344-350 (1998), Form factors of exclusive $b \rightarrow u$ transitions
- [20] Z. Ligeti and M. B. Wise, *Phys. Rev.* **D53**, 4937 (1996)
- [21] Private communication with Mark Wise

-
- [22] Particle Data Group: Review of Particle Physics, *Eur. Phys. J.* **C15** (2000).
- [23] B. Aubert *et al.*, The *BABAR* Detector, submitted to *Nucl. Instrum. and Methods* (2001).
- [24] Measurement of the Number of Upsilon(4S) Mesons, BAD note 134, Chris Hearty
- [25] Luminosity Measurement, BAD note 229, Christos Touramanis
- [26] GEANT4 homepage: <http://wwwinfo.cern.ch/asd/geant4/geant4.html>
- [27] F. Fazio and M. Neubert, $B \rightarrow X_u \ell \nu$ decay distributions to order α_s , hep-ph/9905351v2
- [28] J.L. Goity and W. Roberts, Soft pion emission in semileptonic B meson decays, *Phys. Rev.* **D51** 3459-3477 (1995)
- [29] T. Brandt, Electron Identification and Measurement of the Inclusive Semileptonic Branching Fraction of B Mesons at the *BABAR* Experiment, PhD Thesis at the Tech. University Dresden (2002).
- [30] ALEPH, CDF, DELPHI, L3, OPAL, SLD, Combined results on b-hadron production rates and decay properties, CERN-EP/2001-050 (2001).
- [31] OPAL Collaboration, *Eur. Phys. J.* **C21**, 399-410 (2001).
- [32] CLEO Collaboration, Improved Measurement of $|V_{ub}|$ with Inclusive Semileptonic B Decays, hep-ex/0202019v1 (2002)
- [33] *BABAR* Collaboration, DPF 2002 Williamsburg, Conference Contribution
- [34] Determination of the Tracking Efficiency for High Momentum Tracks, BAD note 61, Gerhard Raven.
- [35] Measurement of the Tracking Efficiency Using 3+1 τ Events, BAD note 87, Erich Varnes.
- [36] Measurement of the GoodTrackLoose efficiency using SVT tracks, BAD note 157, Erich Varnes.
- [37] <http://www.slac.stanford.edu/BFROOT/www/Physics/Tools/BetaTools/MicroKilling.html>.
- [38] Efficiencies for neutral particles in the calorimeter in RUN1 and RUN2 data using tau 1-on-1 decays, BAD note 378, Francesca Lodovico
- [39] Study of π^0 Efficiencies in RUN1 Data Using τ 1-on-1 Decays, BAD note 196, Tilman Colberg.
- [40] G.C. Fox, S. Wolfram, *Nucl. Phys.* **B149**, 413 (1979).
- [41] Fitting using finite Monte Carlo Samples, Roger Barlow, Christine Beeston, *Comp. Phys. Comm.* **77**, 219-228 (1993).
- [42] Private communication with Thorsten Brandt.

-
- [43] The chi-squared test of goodness-of-fit, *Ann. Math. Statist.* **23**, 315 Section 11.2. (1952).
- [44] J.L.Diaz-Cruz, G.Lopez Castro et J.H.Munoz, *Phys. Rev.* **D54**, 2388 (1996).
- [45] BABAR Collaboration, B. Aubert *et al.*, Improved Measurement of the CP Violating Asymmetry Amplitude $\sin 2\beta$, SLAC-PUB-9153, BABAR-CONF-02-01, (2002).
- [46] BELLE Collaboration, K. Abe *et al.*, Improved Measurement of the CP Asymmetry in the Neutral B Meson System, KEK-PREPRINT-2002-18, BELLE-PREPRINT-2002-12, (2002).

Acknowledgments

I would like to say many thanks to Prof. Dr. K. R. Schubert, who was an excellent doctoral adviser during all the time of my work and who gave me the opportunity to work on a very interesting topic, in an interesting environment. I would also like to say thanks to Prof. Dr. B. Spaan, for many interesting discussions about physics, but not only about physics. I appreciate that Mr. Spaan and Franz Muheim agreed to be referees for my thesis. Many thanks to Thorsten Brandt, Tilmann Colberg, and Rolf Dubitzky for reading through my thesis. Last but not least all of this would not have been possible without the support I received from my parents. Another ingredient, which made life much easier, was the stimulating atmosphere and the sympathy I felt for so many people at our laboratory in Dresden and at Stanford. Thanks, Rainer, for always providing a stable computing platform, and for coping with me and letting me know whenever an idle CPU was available for my work. Finally I appreciate the financial support provided for this work by the Bundesministerium für Bildung und Forschung (BMBF).

Versicherung

Hiermit versichere ich, dass ich die vorliegende Arbeit ohne unzulässige Hilfe Dritter und ohne Benutzung anderer als der angegebenen Hilfsmittel angefertigt habe; die aus fremden Quellen direkt oder indirekt übernommenen Gedanken sind als solche kenntlich gemacht. Die Arbeit wurde bisher weder im Inland noch im Ausland in gleicher oder ähnlicher Form einer anderen Prüfungsbehörde vorgelegt.

Leif Wilden

